ABSTRACT

Title of Dissertation: AN APPROACH TO ESTIMATE GLOBAL BIOMASS BURNING EMISSIONS OF ORGANIC AND BLACK CARBON FROM MODIS FIRE RADIATIVE POWER

Evan A. Ellicott, Doctor of Philosophy, 2009

Directed By: Professor Chris O. Justice
Department of Geography

Biomass burning is an important global phenomenon affecting atmospheric composition with significant implications for climatic forcing. Wildland fire is the main global source of fine primary carbonaceous aerosols in the form of organic carbon (OC) and black carbon (BC), but uncertainty in aerosol emission estimates from biomass burning is still rather large. Application of satellite based measures of fire radiative power (FRP) has been demonstrated to offer an alternative approach to estimate biomass consumed with the potential to estimate the associated emissions from fires. To date, though, no study has derived integrated FRP (referred to as fire radiative energy or FRE) at a global scale, in part due to limitations in temporal or spatial resolution of satellite sensors. The main objective of this research was to quantify global biomass burning emissions of organic and black carbon aerosols and the corresponding effect on planetary radiative forcing. The approach is based on the geophysical relationship between the flux of FRE emitted, biomass consumed, and aerosol emissions.

Aqua and Terra MODIS observations were used to estimate FRE using a simple model to parameterize the fire diurnal cycle based on the long term ratio between Terra and Aqua MODIS FRP and cases of diurnal satellite measurements of FRP made by the geostationary sensor SEVIRI, precessing sensor VIRS, and high latitude (and thus high overpass frequency) observations by MODIS. Investigation of the atmospheric attenuation of MODIS channels using a parametric model based on the MODTRAN radiative transfer model indicates a small bias in FRE estimates which was accounted for. Accuracy assessment shows that the FRE estimates are precise ($R^2 = 0.85$), but may be underestimated. Global estimates of FRE show that Africa and South America dominate biomass burning, accounting for nearly 70% of the annual FRE generated.

The relationship between FRE and OCBC estimates made with a new MODIS-derived inversion product of daily integrated biomass burning aerosol emissions was explored. The slope of the relationship within each of several biomes yielded a FRE-based emission factor. The biome specific emission factors and FRE monthly data were used to estimate OCBC emissions from fires on a global basis for 2001 to 2007. The annual average was 17.23 Tg which was comparable to previously published values, but slightly lower. The result in terms of global radiative forcing suggests a cooling effect at both the top-of-atmosphere (TOA) and surface approaching almost -0.5 K which implies that biomass burning aerosols could dampen the warming effect of green house gas emissions.

An error budget was developed to explore the sources and total uncertainty in the OCBC estimation. The results yielded an uncertainty value of 58% with specific

components of the process warranting future consideration and improvement. The uncertainty estimate does not demonstrate a significant improvement over current methods to estimate biomass burning aerosols, but given the simplicity of the approach should allow for refinements to be made with relative ease.

AN APPROACH TO ESTIMATE GLOBAL BIOMASS BURNING EMISSIONS OF ORGANIC AND BLACK CARBON FROM MODIS FIRE RADIATIVE POWER

By

Evan Ellicott

Dissertation submitted to the Faculty of the Graduate School of the
University of Maryland, College Park, in partial fulfillment
of the requirements for the degree of
Doctor of Philosophy
2009

Advisory Committee:

Professor Chris O. Justice
Dr. Eric Vermote
Professor John R.G. Townshend
Professor Rachel T. Pinker
Professor Ralph Dubayah

Preface

The material presented in Chapters 2, 3, and 4 of this document has previously been published as peer-reviewed journal articles. The papers are multi-author articles and therefore a brief explanation of my role and contribution to each is provided below. In general, I conducted the majority of the analysis and writing and thus the articles and research can, for the most part, be considered solely mine.

Chapter 2: I was responsible for all of the analysis, parametric code manipulation, developing new code to perform analysis, and obtaining and comparing validation data from various sources and authors. Francois Petitcolin developed the parametric model, but I was responsible for all validation processes and modification of the code for various applications, which is the emphasis of this chapter and published paper. Although the overview of radiative transfer modeling, and specifically the explanation of the parametric model processes could be moved to an appendix in this dissertation document, it was concluded by my co-advisors that leaving this material in the main body of text offered the same continuity of the published paper.

Chapter 3: I developed the parameterization process for estimating MODIS FRP and conducted all analysis to evaluate the performance of this methodology. All analysis and writing were conducted in their entirety by me. Data, as well as guidance and mentoring, were provided by the co-authors.

Chapter 4: Several co-authors were critical in the development of the aerosol inversion product. Specifically, Dr. Eric Vermote aided in post-processing of the AOT product and provided guidance in development of the error budget. Otherwise, all analysis and product generation, including deriving FRE-based emission coefficients, estimating OCBC from FRE, and evaluation of the results were performed by me.

Acknowledgements

I thank co-advisors Dr. Eric Vermote and Dr. Chris Justice for their support and guidance. Dr. Vermote has played a critical role in mentoring me with my research while Dr. Justice has been instrumental in reviewing my writing and providing opportunity towards my development in academia.

I thank Dr. Louis Giglio for his technical assistance in developing the FRE methodology, generously offering data, and providing critical assessment of my ideas and approaches. I thank Dr. Gareth Roberts for helping with SEVIRI data and giving feedback on my research and writing. I thank Dr. Wilfrid Schroeder for his helpful technical insight. Finally, I thank Dr. Guido van der Werf for his support through manuscript reviews, offering insight on the GFEDv2 processes and data, providing advice on my research, and feedback on my analysis.

I thank NASA's Earth and Space Science Fellowship Program for recognizing the potential benefits of my research and providing financial support.

Finally, I thank my wife for her commitment and support of this endeavor. It has truly been team effort and she has been a patient participant.

Table of Contents

List of Tables

List of Figures

Chapter 1: Introduction

1.1 Research Goal

The goal of the research presented in this dissertation is to quantify global biomass burning emissions of organic and black carbon aerosols and the corresponding effect on planetary radiative forcing. The approach is based on the geophysical relationship between the flux of fire radiative energy (FRE) emitted, biomass consumed, and aerosol emissions. The following section offers insight to the state of the science and the motivation for this research project.

1.2 Background

Biomass burning is recognized as a significant source of atmospheric trace gas and particulate matter emissions [*Crutzen and Andreae*, 1990] and has received attention from the scientific community over the past several decades as an important contributor to total climatic radiative forcing [*Kaufman et al.*, 1990; *Innes*, 2000]. *Crutzen* [1979] first highlighted the variety of trace gas emissions from tropical forest fires and the potential these constituents could have in altering atmospheric chemistry and biogeochemical cycles. Subsequent research has demonstrated additional impacts on the biosphere, atmosphere, and directly upon humans. For example, ozone (O_3) is produced photochemically in the troposphere from hydrocarbon and nitrogen oxides released during vegetation burning and results in regional health hazards such as damage to human respiratory systems [*Levine*, 2003; *Andreae*, 2004].

Cicerone (1994) emphasized that some byproducts of biomass burning, such as methyl chloride (CH_3Cl) and methyl bromide (MeBr), can escape to the stratosphere where they are responsible for ozone destruction; resulting in health risks at a much larger scale.

Fire is an integral part of many ecosystems [*Kuhry*, 1994; *Cary and Banks*, 2000], but the nature of this relationship may change according to some climate models which show fire frequency and intensity increasing with global warming trends [*Intergovernmental Panel on Climate Change* (*IPCC*), 2007]. In addition, the influence of anthropogenic ignited fires, which accounts for 90% of all biomass burning [*Levine*, 2001], may increase with population growth and the added pressure for land and resources. A result of these driving forces will be greater biomass burning emissions, decreased sequestration of carbon, and the potential creation of feedback loops [*Kasischke et al.,* 1995a; *Chapman and Thurlow*, 1998; *Moore*, 2002].

Gas and particulate matter injected into the atmosphere from vegetation fires results in complex outcomes for radiative budgets. Although surface and lower-atmospheric warming due to the greenhouse gas effect is generally well understood, there is significant uncertainty in terms of aerosol emissions in large part due to the temporal and spatial heterogeneity of fire and the short atmospheric lifespan of aerosols (minutes to days). *Twomey* [1984] suggested that cloud condensation nuclei produced as a result of aerosols released from biomass burning could increase cloud cover and reflectance. The net effect would be a cooler atmosphere and reduced surface insolation. *Kaufman and Fraser* [1997] found a similar effect of smoke particles increasing reflectance, as well as potential alteration to hydrologic regimes

due to decreased precipitation. However, *Kaufman and Fraser* stated that the climatic cooling force of smoke was significantly less than previously suggested by models. In addition, aerosols can influence Earth's climate in more complex and indirect pathways such as changing cloud albedo and lifetime. Thus, the impact of aerosol forcing is still rather uncertain and generally due to incomplete estimates of emission sources and loading.

Soja et al. [2004] and *French et al.* [2004] suggested that limited information about soil organic layer burning is potentially a significant source of error in biomass burning emission estimates. *Ito and Penner* [2005], using the Global Burned Area (GBA) product from the SPOT satellite, estimated 1428 Tg carbon (C) emitted from fires in 2000. For comparison, *Hoelzemann et al.* [2004], using the Global Burnt Scar (GLOBSCAR) burned area product generated from the ASTR satellite, estimated 1741 Tg C for the same year. This is surprising given *Ito and Penner's* [2005] GBA burned area estimate was nearly twice as large as GLOBSCAR used by *Hoelzemann et al.* [2004] (314×10^6 ha and 172×10^6, respectively). *Kasischke and Penner* [2004] suggested that differences in fuel load estimates and combustion factors, in addition to burned area, were responsible for the disagreement in emission estimates. A comparison of carbon emission estimates from biomass burning for 2000 made by *van der Werf et al.* [2006] (2038 Tg C) and *Schultz et al.* [2008] (2254 Tg C) highlights additional variability in recent estimates.

Organic and black carbon (OC and BC, respectively) are predominately generated from biomass burning [*Bond et al.,* 2004] and are associated with light scattering and absorbing properties, respectively. Relatively greater emissions of OC and BC come

from forest fires than savanna fires owing to the larger proportions of smoldering combustion. (Note that OC + BC aerosol emissions are referred to as OCBC for the remainder of the paper). Global estimates of these fine mode aerosols emitted from biomass burning have greater uncertainties than trace gas emissions [*Andreae and Merlet*, 2001]. As an example, *van der Werf et al.* [2006] reported 22 Tg of OCBC in 2001, while *Chin et al.* [2007] reported 56.3 Tg for the same year. In their earlier work, *Chin et al.* [2002] estimated an annual average of 88 Tg OCBC for the 1990s. This higher estimate is in part due to the use of a larger emission factor (14 g/kg [2002] vs. 8g/kg [2007]) and larger estimate of biomass combusted (5510 Tg dry matter [2002] vs. 4942 Tg dry matter [2007]). Other estimates of OCBC are reasonably consistent. *Hoelzemann et al.* [2004] reported 17.6 Tg of OCBC for 2000 with a range of 13.6 – 20.2 Tg. *Schultz et al.* [2008] developed a 40 year inventory of vegetation fire emissions using a combination of burned area estimates from satellite products, data reported in the literature, and modeling which yielded an OCBC annual mean for the 1990s of 25 Tg. *Andreae and Merlet* [2001] reported 26.1 Tg of OCBC emitted from fires for the late 1990s while *Bond et al.* [2004] had 26.3 Tg OC for a "typical" year in the 1990s. However, it should be noted that most of these estimates relied in some part, if not directly, on emission factors reported by *Andreae and Merlet* [2001], suggesting that agreement between estimates is often a result of use of common data, and thus similar in biases [*Robinson,* 1989]. Differences may therefore be attributed to variations in other modeling components such as fuel loads or burned area [*Kasischke and Penner*, 2004; *Schultz et al*. 2008]. It is not surprising then that current uncertainty surrounding the impact of aerosol forcing is, according to the

International Global Observation Strategy (IGOS), "one of the largest unknown factors in climate research" and is in large part due to poor estimates of the contribution from biomass burning [*Barrie et al.*, 2004].

In part, the variation in emission estimates can be attributed to the methodologies employed. A common approach, referred to in this paper as "bottom up", is based on estimates of surface variables (total fuel consumed during combustion, the area burned, and the type of fuel affected) that are used to compute emissions to the atmosphere. On the other hand, "top down" (inversion) approaches seek to measure atmospheric constituent concentration associated with fire (e.g. CO, aerosols) to estimate emission sources at the surface.

Earth observing satellites have made a significant contribution to wildfire detection, monitoring, and characterization for nearly two decades [*Dozier*, 1981; *Kaufman et al.*, 1990; *García*, 1991; *Robinson*, 1991; *Kasischke et al.*, 1995a; *Kasischke et al.*, 1995b; *van der Werf et al.*, 2003; *Wooster et al.*, 2003; *Korontzi et al.*, 2004; *Wooster et al.*, 2005; *van der Werf et al.*, 2006]. Current satellite based, bottom-up approaches to estimate emissions involve multiplying the fuel consumed by an *a priori* emission factor for the atmospheric species (gas or aerosol) of interest (equation (1.1)):

$$E_x = EF_x \times M \tag{1.1}$$

Where E_x is the emission load of species x (g); EF_x is the emission factor for species x for the specific vegetation type or biome (g kg^{-1}); and M is the biomass burned (kg). The biomass burned is calculated using equation (1.2).

$$M = A \times B \times \beta \tag{1.2}$$

Where A is the burned area (km^2); B is the biomass or fuel load (g km^{-2}); and β is combustion factor (fraction of available fuel burned). The combustion factor cannot be measured from space and the uncertainty in space-based measurements of burned area and fuel loads is high [*van der Werf et al.,* 2006]. *Boschetti et al.* [2004] showed that differences in spatial and temporal estimates of burned area were apparent between the GLOBSCAR and GBA2000 products with the latter producing a global burned area nearly twice as large as GLOBSCAR. They concluded that such discrepancies have serious implications for accurately quantifying emissions from fires [*Boschetti et al.,* 2004]. *Korontzi et al.* [2004] showed that estimates of burned area can vary significantly between burned area algorithms, which when coupled with the landcover types that are burning, can result in differences in the amount of biomass consumed exceeding a factor of two. The difficulty in accurately measuring these variables leads to an uncertainty in emission estimates of at least 50%, and possibly much greater [*Robinson*, 1989; *Andreae and Merlet*, 2001; *van der Werf et al.,* 2003; *French et al.*, 2004; *Korontzi et al.*, 2004]. Although datasets used for this application are continuously improved [*Roy et al.*, 2005; *van der Werf et al.*, 2006],

due to the uncertainty in current estimates it is worthwhile to explore other approaches.

1.3 Research Hypothesis and Objectives

Biomass burning is a global phenomenon with significant implications for climatic forcing, human health, biodiversity, and land cover. However, as described above, uncertainty in emission estimates from vegetation fires is still rather large. Recently, emerging advances in satellite remote sensing of fire radiative energy offer opportunities for direct measurement of biomass consumed. Therefore, the main the hypothesis for this research is:

> *Quantifying global biomass burning aerosol emissions based on the fire radiative energy can offer improved estimates with less uncertainty than current methods used in emission modeling?*

In order to investigate the relationship between fire energy and emissions the following research objectives are addressed in this dissertation:

1. Atmospheric attenuation must be accounted for in order to accurately estimate radiances observed by satellite sensors. Therefore,
    - Validation of a new parametric model for atmospheric correction of thermal infrared data, including the evaluation of atmospheric attenuation of MODIS MIR "fire" channels, is performed.

2. Currently, MODIS provides global coverage of instantaneous FRE, or the fire radiative power (FRP), but is limited in the temporal domain to an average of 4 observations a day. In order to estimate the total aerosol emissions from fire based on the fire intensity, the temporal trajectory of FRP must be known. Consequently,
    - A methodology is developed to parameterize the diurnal cycle of hourly FRP from MODIS observations (at 0.5° spatial and monthly temporal resolutions). The integral is calculated to produce FRE which is then assessed with estimates made from higher temporal resolution sensors.
    - An additional analysis of the performance of the FRP parameterization is conducted based on the estimates of biomass consumed, fuel loads, and carbon emissions for African wildland fires.
3. Given the uncertainty in current estimates of biomass burning emissions described in the previous section, improved or alternative approaches should be explored. Thus,
    - The relationship between the estimated FRE and a new MODIS-derived inversion product of daily integrated, biomass burning aerosol emissions of organic carbon (OC) and black carbon (BC) is explored. FRE-based emission factors (referred to as emission coefficients hereafter) are generated and global, monthly estimates

of OCBC emissions from biomass burning for multiple years presented.

- An additional component necessary to objectively assessing the approach described in this research is to provide a review of the potential sources and magnitude of error in the data and estimates.

4. Finally, to understand the implications of the biomass burning emissions estimated in this research,
    - The global radiative forcing is calculated and compared with current estimates offered by the 2nd version of the Global Fire Emissions Database (GFEDv2).

1.4 Dissertation Outline

This dissertation consists of five chapters, three of which are self-contained, with the focus of the research on making global estimates of biomass burning organic and black carbon aerosols based on the fire radiative energy (FRE) liberated during combustion.

Chapter 1 introduces the importance of biomass burning emissions and the current uncertainty in emission estimates and the corresponding radiative forcing. Chapter 2 presents the validation of a new parametric model for atmospheric correction of thermal infrared data. The investigation provides an accuracy assessment of the parametric model and demonstrates the application of the model for operational use. In addition, Chapter 2 offers an evaluation of the atmospheric impact on FRP measurements and a simple, yet effective, correction approach.

In Chapter 3 an approach to estimate fire radiative power (FRP) from MODIS beyond the nominal observations is presented. Employing high temporal frequency observations from the SEVIRI and VIRS satellite sensors, as well as high latitude retrievals made by MODIS, the diurnal cycle of FRP is characterized at monthly intervals for multiple years. The relationship between the diurnal cycle and the ratio of Terra-MODIS and Aqua-MODIS FRP measurements is explored as a method to parameterize the fire energy temporal trajectory. The FRE is then calculated, using only MODIS data, as the integral of the discrete FRP estimates. Comparison of FRE estimates, as well as biomass combusted (using an FRE-based combustion factor), is made with other data sources.

Chapter 4 examines the relationship between the estimated FRE and a new MODIS-derived inversion product of daily integrated, biomass burning aerosol emissions. The inversion product is generated from the MODIS fine mode aerosol optical thickness and inverse modeling transport processes adopted from the Goddard Chemistry Aerosol Radiation and Transport (GOCART) model. A global analysis follows, using a similar approach to *van der Werf et al.* [2006], to determine emission coefficients. The relationship between estimated FRE and the inversion-based OCBC product is analyzed within 3 globally dispersed vegetation zones (biomes) and employed as an FRE-based emission factor (referred to here as an *emission coefficient*). Applying the FRE estimates from Chapter 3 with the emission coefficient developed in Chapter 4, a multi-year (2001-2007) global dataset of biomass burning OCBC emissions is produced. Chapter 4 also includes an error budget to address the uncertainty in the OCBC estimates.

Finally, Chapter 5 concludes with a summary of the research with interest paid to the radiative forcing impact from biomass burning aerosols. The topic of potential ways to improve the emission estimates, and the methodologies that will need to be employed to make them, is also addressed.

The framework of this dissertation is shown in Figure 1.1.

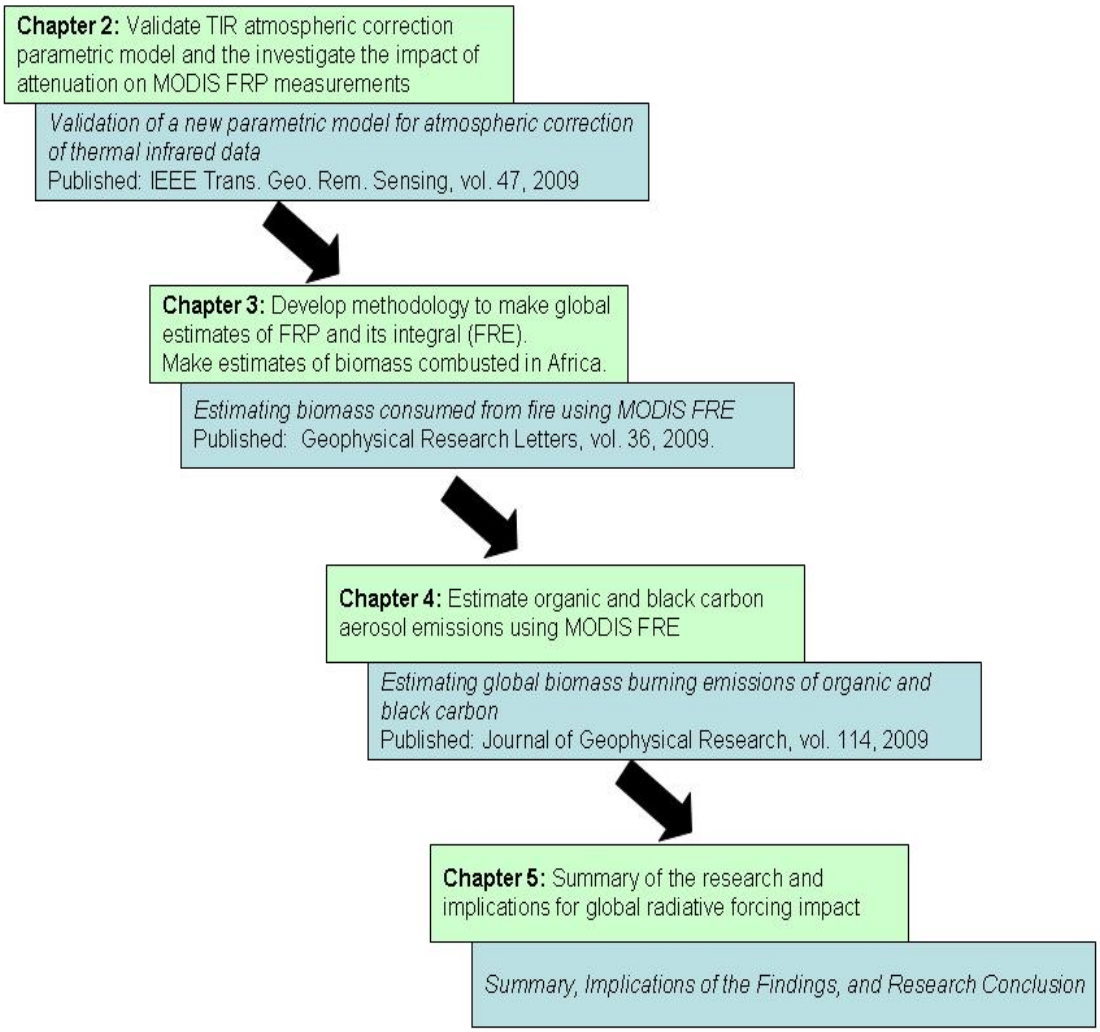

Figure 1.1: Research framework. Chapter titles in italics.

Chapter 2: Validation of a New Parametric Model for Atmospheric Correction of Thermal Infrared Data[1]

2.1 Introduction

Knowledge of the surface temperature is critical to understanding the flux of energy between the Earth's surface and atmosphere, and therefore an important part of climate modeling, analyzing vegetative stress, and hydrologic modeling [*Jacob et al.,* 2002; *French et al.,* 2003]. Land surface temperature (LST) may reveal latent information about soil moisture, drought conditions, and land cover change [*Lambin and Ehrlich,* 1996]. Sea surface temperature (SST) has historically been used for meteorological and weather prediction applications, but also provides the basis for a long term data record of climatic change [*Merchant and LeBorgne,* 2004].

Retrieval of surface temperature from space-borne sensors has been successfully employed since the early 1980s using a variety of instruments such as the Advanced Very High Resolution Radiometer (AVHRR) [*Deschamps and Phulpin,* 1980; *Barton,* 1995]. Surface temperatures are typically retrieved from thermal infrared (TIR) (8-12μm) satellite observations; however accurate retrievals require correction for atmospheric effects. For example, attenuation of thermal infrared satellite observations is largely due to the columnar water vapor present in the atmosphere, specifically in the lower troposphere [*Matthew et al.,* 2001]. This paper verifies the performance of a parametric model, which is tuned to the Moderate Resolution

[1] The bulk of this chapter was published in *Ellicott et al.* [2009a]

Imaging Spectrometer (MODIS), for atmospheric correction in the TIR. Ultimately, the goal is to devise a global operational atmospheric correction scheme for the MODIS sensor that would provide greater accuracy and less computational time than current atmospheric correction methods.

One particular method commonly employed for atmospheric correction of thermal infrared data involves using the differential absorption between two spectrally discrete bands (typically at 11μm and 12μm) to account for water vapor absorption in the atmosphere [*Prabhakara et al.,* 1974]. This empirical method, referred to as split-window, offers a relatively accurate (± 1.0 K) method for retrieving the surface temperature, provided the surface emissivity is known explicitly or implicitly [*Barton,* 1995; *Eugenio et al.,* 2005]; implicit knowledge is obtained through the regression of satellite data to ground temperature measurements. However, this approach has several shortcomings and is subject to bias [*McClain et al.,* 1985; *Merchant and LeBorgne,* 2004]. The split-window approach can reliably account for atmospheric attenuation over sea surfaces where emissivity is generally well known and stable and, relying upon the empirical calibration between buoy temperature retrievals and satellite observations, achieve an accuracy of <0.5 K [*McClain et al.,* 1985; *Barton,* 1995; *Merchant and LeBorgne,* 2004]. However, there is a latitudinal, as well as hemispherical, asymmetry in the concentration of buoy temperature retrievals which is a limitation to synoptic SST retrieval [*Minnett,* 2003]. In addition, bias is likely a result of the regression process for fitting satellite derived temperatures to buoy temperatures because buoy temperatures are retrieved below the surface (bulk), while satellite radiometer derived temperatures are based on the

surface (skin) temperature [*Hook et al.,* 2003; *Minnett,* 2003]. LST retrievals, corrected using the split-window approach, must deal with greater uncertainty in the emissivity of terrestrial features observed by satellites as a result of the heterogeneous nature of land surfaces, as well as a lack of a systematic *in situ* data available for developing the regression coefficients used in the SST algorithm. Though regionally accurate, especially for water body targets, the split window scheme is not ideal for global, operational atmospheric correction of land surface temperature retrieval.

An alternative method to atmospherically correct surface temperature retrievals uses a single infrared band, typically centered at 11μm because of limited atmospheric perturbation around this wavelength. This requires an accurate radiative transfer model (RTM) and prior information about the surface emissivity and atmospheric conditions, specifically temperature and water vapor profiles [*Chou et al.,* 1991; *French et al.,* 2003]. Atmospheric profiles have traditionally been retrieved from radiosonde data [*Durre et al.,* 2006] and are often assimilated into circulation models to generate coarse, global resolution datasets, such as the National Centers for Environmental Prediction (NCEP) Global Data Analysis System (1˚ x 1˚, 6 hour) product. A combination of atmospheric profiles with a RTM, such as MODTRAN [*Berk et al.,* 1998; *Anderson et al.,* 2000], provides an effective methodology to generate the corrected variables necessary for surface temperature calculation [*Petitcolin and Vermote,* 2002]. A limitation to the single channel – RTM method is the large size of data sets and therefore the computation time required, thus making the single channel approach generally impractical for operational correction of satellite retrievals, especially at synoptic scales [*Chou et al.,* 1991; *French et al.,*

2003]. Various approaches have been proposed to simplify RTM, including, but not limited to: reducing RTM to very simple equations [*French et al.,* 2003], using pre-computed corrections that are interpolated according to the difference between the local atmospheric profile and reference profiles [*Chou et al.,* 1991], correlated-*k* model [*Kratz,* 1995], or neural networks [*Gottsche and Olesen,* 2002]. However, these approaches have their limitations. For example, [*French et al.,* 2003] simplified atmospheric correction by implementing an adjusted water vapor continuum correction technique, achieving a processing time 15x faster than MODTRAN. The bias (0.8K – 1.6 K) in temperature retrievals using this approach, on the other hand, does not provide enough margin for accurately retrieving surface temperatures. The neural networks technique described by [*Gottsche and Olesen,* 2002] achieved accurate results (RMSE = 0.16 – 0.3K) and was 104 times faster than MODTRAN 3.1, but inherent limitations to neural networks were not addressed. The underlying processes are not clear and the user may not readily have access to the underlying architecture. In addition, time is required to "train" the network (6 days in the case of *Gottsche and Olesen* [2002] which is fast by most NN standards) and there is an over simplification of atmospheric variables as they are integrated over the full optical path. Correlated-k models are limited when considering vertically inhomogeneous atmospheres in part because of the assumption that absorption coefficients are correlated between vertical layers.

The purpose of this study was to assess the accuracy of a single channel atmospheric correction scheme which is tuned to the MODIS sensor (currently flying aboard the Earth Observing System (EOS) satellites Terra and Aqua at an altitude of

705km, viewing the entire Earth's surface every 1 to 2 days). The goal was to achieve the same accuracy as MODTRAN, but with less computational demand (i.e. speed) by parameterizing processes used in radiative transfer modeling. Thus, the correction scheme is a trade-off between complexity and accuracy. The parametric model was developed upon lessons learned by *Petitcolin and Vermote* [2002] and is based a on least squares fitting methodology to derive model coefficients. In *Petitcolin and Vermote* [2002], MODTRAN was run using NCEP profile data to retrieve the necessary atmospheric correction variables. The variables returned were then interpolated from 1° to 1km to correct MODIS TIR observations. This was done to minimize the computation time of actually running MODTRAN using 1km data. Since the parametric model is less computationally demanding than MODTRAN, the atmospheric profile data can be interpolated rather than the atmospheric correction variables. This reduces the uncertainty in the correction variables which arises from the shifting view and solar angles across a 1° pixel that cannot be accounted for during the interpolation. The parametric model demonstrated a comparable accuracy to MODTRAN when testing against "reference" datasets, as well as *in situ* data. Initially the parametric model was evaluated against MODTRAN using a synthetic dataset (sections 2.4 and 2.5). Sea-surface temperatures derived by the parametric model were then assessed against the MODIS SST product in section 2.6. In section 2.7 *in situ* lake surface and land surface temperatures were used to investigate the models accuracy. The parametric model is then used to investigate the impact of atmospheric attenuation on the MODIS fire radiative power (FRP) product in section 2.8. Finally, in section 2.9 the consistency of temperature results is examined using

different combinations of available atmospheric profile data (i.e. radiosonde, satellite sounding) with the parametric model. Concluding remarks are made in section 2.10.

2.2 Overview of the Parametric Model for Atmospheric Correction

Surface radiance, a variable used to calculate surface brightness temperature in the thermal infrared, requires correction of satellite observations for atmospheric effects. Based upon top-of-atmosphere (TOA) radiance measured by spaceborne infrared sensors, upward atmospheric radiation (path radiance), downward atmospheric radiation (diffuse radiance), atmospheric transmittance, and *a priori* knowledge of surface emissivity, the following equation is used to retrieve surface radiance:

$$L_{surf\,\lambda} = [(L_{toa\,\lambda} - L_{atm\,\lambda\uparrow}) / t_{\lambda}] - (1 - \varepsilon_{\lambda})\, L_{atm\,\lambda\downarrow} \qquad (2.1)$$

where $L_{surf\,\lambda}$ is the surface radiance (W m^{-2} sr^{-1} μm^{-1}), $L_{toa\,\lambda}$ is the TOA radiance observed at the sensor (W m^{-2} sr^{-1} μm^{-1}), $L_{atm\,\lambda\uparrow}$ is the upwelling atmospheric radiance (W m^{-2} sr^{-1} μm^{-1}), $L_{atm\,\lambda\downarrow}$ is the average directional downwelling atmospheric radiance (W m^{-2} sr^{-1} μm^{-1}), t is the atmospheric transmittance (unitless), and ε is the surface emissivity; a dimensionless value representing the ratio of a surface's spectral radiance to a perfect black body spectral radiance, for a given temperature. An additional consideration when using satellite data is that the above equation is based on monochromatic observations while remote sensing is based on

broadband observations comprised of a continuous range of wavelengths per channel (or band). Therefore, equation (2.1) will include a spectral response function (f), which is the integrated contribution of the individual wavelengths (λ) within a given band (i). The spectral integration is applied to all terms of equation (2.1) so that the surface radiance is derived from the TOA radiance, observed by the sensor in broadband.

The parametric model for atmospheric correction in TIR aims at computing the upwelling atmospheric radiance, the downwelling atmospheric radiance and the atmospheric transmittance, all being band integrated. Such computation requires atmospheric data along the line-of-sight, also known as atmospheric profile, which includes atmospheric temperature, water vapor density, pressure and altitude. Data provided by numerical weather prediction models such as NCEP, with 28 layers at known pressure levels between 1030hPa to 10hPa, offer profiles for atmospheric correction in TIR. The proposed parametric model is based on the computation of the optical thickness τ_i ($t_i = e^{-\tau_i}$), upwelling atmospheric radiance, and the downwelling atmospheric radiance, on a layer basis, integrated along the optical path.

2.2.1 Layer Optical Thickness

In the thermal infrared, layer transmission is mainly due to gaseous absorption. Molecular scattering is weak and no aerosol effects need to be considered for most cases according to Mie theory since particles are much smaller than the wavelength. The main absorbent in TIR is water vapor, for which a continuum is observed.

Therefore, the optical thickness for layer *l* in channel *i* is the sum of three components for water vapor, water vapor continuum and other gases:

$$\tau_{l,i}=\tau_{l,i}^{H20}+\tau_{l,i}^{H20c}+\tau_{l,i}^{other} \tag{2.2}$$

The layer optical thickness of water vapor is computed using:

$$\tau_{l,i}^{H20} = \exp\left(a_{0,H2O,i} + a_{1,H2O,i}\rho_{H2O} + a_{2,H2O,i}\rho_{H2O}^2\right) \tag{2.3}$$

Where

$$\rho_{H2O} = \log\left(\frac{\rho_{0,H20}}{\cos(\theta_v)}\right) \tag{2.4}$$

where $\rho_{0,H2O}$ is the water vapor abundance of the layer in g m^{-2} (i.e. the water vapor density integrated along the vertical path within the layer) and θ_v is the view angle. The quadratic exponential form of equation (2.3) was found to be the optimal trade off between accuracy and simplicity. Adding terms such as ρ_{H2O}^3 or ρ_{H2O}^4 in the equation does not help capture the spectral non-linearities of the optical thickness of water vapor within the infrared band considered. $a_{0,H2O,i}$, $a_{1,H2O,i}$, and $a_{2,H2O,i}$ are band coefficients that depend on equivalent layer temperature (T_l) and equivalent layer pressure (P_l). The "a" coefficients are tabulated for each couple (T_l, P_l) of the atmospheric layers defined in Table 2.1 and stored in a look-up-table. T_l [resp. P_l] is computed using top layer and bottom layer temperatures [resp. pressures], using a weighting coefficient of 0.5. Parameters $a_{0,H2O}$, $a_{1,H2O}$ and $a_{2,H2O}$ are computed

using a least square fitting method for atmospheric layer configurations reported in Table 2.1. The reference optical thickness is computed by MODTRAN for the same atmospheric layer conditions (see equation (2.9)).

For optical thickness due to the water vapor continuum, the parametric model uses the model integrated in MODTRAN [*Clough et al.,* 1982; *Clough,* 1995]. The water vapor continuum is observed absorption due to water vapor that is not attributable to the Lorentz line contribution within $25cm^{-1}$ of each line. It is the difference between measured absorption and that which is predicted by theory. In other words, the continuum is absorption that cannot be accounted for by theory alone but is nonetheless real [*Grant,* 1990]. Absorption coefficients for the so-called self-broadened and foreign-broadened water vapor continuum models have been spectrally integrated with the sensor spectral response functions. Since the spectral variations of the absorption coefficients of the water vapor continuum are very smooth, values of τ^{H2Oc} computed by MODTRAN are reproduced by the parametric model.

The layer optical thickness due to atmospheric constituents other than water vapor is computed using:

$$\tau_{l,i}^{other} = \exp\left(a_{0,other,i}\rho_{other}^{a_{1,other}}\right) \tag{2.5}$$

where

$$\rho_{other} = \frac{D}{\cos(\theta_v)} \tag{2.6}$$

where D is the layer depth in kilometer. $a_{0,other,i}$ and $a_{1,other,i}$ are band coefficients that depend on T_l and P_l. Both parameters are derived by least square fitting for the layer configurations in Table 2.1.

Table 2.1: Atmospheric layer configurations used for computing atmospheric water vapor layer density, as well as other coefficients, from a least square fitting method.

(**P**) Pressure (hPa)		(**T**) Air temperature range (K)			Altitude of bottom of layer (km)	Relative humidity range (%)
Bottom of layer	Top of layer	From	To	Step		
1030	1000	260	320	5	0	10, 30, 50, 70, 90
1000	975					
975	950	250	300	5	0.5	
925	900				1	
850	800	240	290	5	1.5	
750	700				2	
650	600	230	280	5	3	
550	500				4.5	
450	400	220	260	5	6	
350	300				8	
250	200	210	240	5	10	1, 10, 30, 50, 70
150	100	200	230	5	13	1, 10, 30, 50
70	50				18	1, 10, 30
30	20				24	

Finally, in order to correct for non-linearities in optical thickness, spectral integration is applied. Radiative transfer models, such as MODTRAN, can apply the convolution with the sensor spectral response function (f) to wavelength radiances (L_λ) at layer level, as well as for the full optical path. The layer transmission is then:

$$t_{l,i}=\frac{\int_{\lambda_1}^{\lambda_2} t_{l,\lambda} L_\lambda f_i(\lambda) d\lambda}{\int_{\lambda_1}^{\lambda_2} L_\lambda f_i(\lambda) d\lambda} \tag{2.7}$$

where the layer transmittance in wavelength λ can be decomposed as:

$$t_{l,\lambda} = \exp\left(-\tau_{l,\lambda}^{H2O} - \tau_{l,\lambda}^{H2Oc}\ \tau_{l,\lambda}^{other}\right) \tag{2.8}$$

However, with the parametric model, computations at numerous wavelengths are avoided in order to reduce the computation time needed for atmospheric correction. Therefore, the spectral convolution is moved to the coefficients of the parametric models that are needed to compute the layer optical thickness of water vapor, water vapor continuum, and other gases. The spectrally integrated layer optical thickness is:

$$\tau_{l,i}^{e} = \frac{\int_{\lambda_1}^{\lambda_2} \tau_{l,\lambda}^{e}\ f_i(\lambda) d\lambda}{\int_{\lambda_1}^{\lambda_2} f_i(\lambda) d\lambda} \tag{2.9}$$

with superscript *e* being either *H2O*, *H2Oc* or *other* for the optical thickness of water vapor, of water vapor continuum, and other gases, respectively. Because the exponential function is not linear and the spectral variations of the absorption coefficients of water vapor and other gases are not smooth, moving the spectral

integration from radiances to optical thickness biases the layer transmissions computed with the parametric model. Such bias is corrected using a quadratic function applied to the layer optical thickness equation below, replacing the traditional $t=\exp(-\tau)$ formulation in the parametric model. The quadratic function offered the best fit while providing a trade-off between simplicity and accuracy.

$$t_{l,i}=\exp\left(-m_{1,l,i}\tau_{l,i}-m_{2,l,i}\left(\tau_{l,i}\right)^2\right) \tag{2.10}$$

where m parameter is derived from least square fitting. The correction is applied to layer transmissions before they are used later in the parametric model for the computation of atmospheric upwelling radiance, atmospheric downwelling radiance and total transmittance along the line of sight.

2.2.2 Layer Upwelling and Downwelling Radiances

Assuming the layer is a semi-transparent medium in local thermodynamical equilibrium, Kirchhoff's Law links the layer emission to the layer transmission so that the layer atmospheric upwelling radiance is computed using:

$$L_{l,atm\uparrow i}=\left(1-t_{l,i}\right)L_i\left(T_{l,atm\_eq}\right) \tag{2.11}$$

L_i is the Planck function, as introduced later in equation (2.21), convoluted with the spectral response function of band i. The equivalent layer temperature T_{l,atm_eq} is

derived from top layer temperature and bottom layer temperature, weighted by w (0.5):

$$T_{l,atm\_eq} = wT_{l,bot} + (1-w)T_{l,top} \tag{2.12}$$

where *top* and *bot* subscripts indicate top or bottom layer, respectively. The layer downwelling atmospheric emission integrated over the hemisphere is derived using

$$L_{l,atm\downarrow i} = (1-t_{l,i}(\theta_{emis\downarrow}))L_i(T_{l,atm\_eq}) \tag{2.13}$$

where $\theta_{emis\downarrow}$ is the equivalent view angle for which the layer transmittance is computed to be used in the above equation. Assuming the downwelling atmospheric radiance is isotropic; [*Kondratiev,* 1969] has shown that $\theta_{emis\downarrow} = 53^\circ$ is optimal.

2.2.3 From Layer to Total Transmittance and Total Radiances

To be used in equation (2.1), total transmittance, total upwelling radiance and total downwelling radiance along the line-of-sight shall be derived from layer quantities, the atmosphere being sliced in L layer with layer 1 at low altitude and layer L at top of the atmosphere. The band atmospheric transmittance t_i along the optical path is derived from the product of the transmission of the layers ($t_{i,l}$), yielded in equation (2.10).

$$t_i = \prod_{l=l}^{L} t_{l,i} \tag{2.14}$$

For the upwelling radiance, layer contributions are summed, accounting for the atmospheric transmittance of the layers between the layer and the sensor.

$$L_{atm\uparrow i} = \sum_{l=1}^{L} t_{l+1\to L,i} L_{l,atm\uparrow i} \tag{2.15}$$

where $t_{l+1\to L,i}$ is the transmittance along the path from top of layer *l* to top of the atmosphere

$$t_{l+1\to L,i} = \prod_{l=l}^{l_2} t_{l,i} \tag{2.16}$$

In parallel, downwelling emission reaching the surface is the sum of the layer contributions, accounting for the transmittance of the atmosphere between the layer and the surface.

$$L_{atm\downarrow i} = \sum_{l=1}^{L} t_{1\to l-1,i}\left(\theta_{emis\downarrow}\right) L_{l,atm\downarrow i} \tag{2.17}$$

with $t_{1\to 0,i}\left(\theta_{emis\downarrow}\right) = 1$.

2.3 Analysis Metrics

The following statistics were used to evaluate the performance of the parametric model and appear, for consistency, throughout this paper. The RMSE refers to the root mean square error and represents the degree of error between estimator and observed values of the quantity being investigated:

$$RMSE = \sqrt{\frac{\sum_{i=1}^{n}(e_i - o_i)^2}{n}} \tag{2.18}$$

where e_i is the estimated value from the parametric model, o_i is the observed (or "truth"), and n is the number of observations. In this analysis, "observed" data may be a metric to evaluate the model, as in the case of comparison with MODTRAN, or actual (*in situ*) observations:

The mean bias provides a statistical measure of the accuracy as computed by averaged sum of differences between all estimates, e_i and observed (o_i) data.

$$B = \frac{\sum_{i=1}^{n}(e_i - o_i)}{n} \tag{2.19}$$

Precision represents the repeatability of the estimates and is computed as the standard deviation of the estimates around the observed values, corrected for the mean bias (B):

$$P = \sqrt{\frac{\sum_{i=1}^{n}(e_i - o_i - B)^2}{n-1}} \tag{2.20}$$

Finally, the Nash-Sutcliffe model efficiency coefficient (E) was used as a goodness of fit metric to assessing the parametric model. In this case, the modified E, which replaces squaring the differences with the absolute value, was used. This is intended to limit the bias towards extreme values.

$$E = 1.0 - \frac{\sum_{i=1}^{n}|e_i - o_i|}{\sum_{i=1}^{n}|o_i - \overline{o}_i|} \tag{2.21}$$

where $\overline{o_i}$ is the mean of the observed values.

E ranges from -∞ to 1, such that a value of E = 1.0 indicates a perfect match between estimated and observed values. E = 0.0 occurs when the model estimated values are as accurate as the mean of the observed data. While a value of E < 0.0 indicates that the mean of the observed values is a better predictor than the model. The motivation for using E is to provide a relative measure other than the often-used coefficient of determination (R^2). According to *Legates and McCabe* [1999], the latter is sensitive to outliers while insensitive to additive and proportional differences between the observed and predicted values. Thus, high values of R^2 may be achieved even when the model and observed results are quite different in magnitude.

2.4 Evaluation of the Parametric Model Performance

The MODIS instrument includes 7 emissive bands that are useful for surface temperature remote sensing. The additional MODIS thermal bands are designated, as an example, for atmospheric sounding and not intended for surface retrievals. Thus, initial assessment of the parameterization was based on the agreement between the retrieved parameters from MODTRAN and the parametric model in these 7 bands (Table 2.2).

Table 2.2: MODIS-Terra band equivalent wavelengths for TIR bands.

BAND	20	21	22	23	29	31	32
λ_i (μm)	3.7882	3.9921	3.9921	4.0567	8.5288	11.0186	12.0325

Evaluation of the parametric model was focused on the three atmospheric parameters derived during radiative transfer modeling ($L_{atm}\uparrow$, $L_{atm}\downarrow$, and t). Each dataset was comprised of a MODIS granule (2004.047.0800, centered at 12°N 42°E; see Figure 2.1) and NCEP data, extracted from the work of *Petitcolin and Vermote* [2002], which provided geometric information related to satellite position (observation angle) and atmospheric profile data, respectively, to be used in MODTRAN and the parametric model in order to generate the above parameters. The observations had a water vapor content range of 0.64 to 3.93 g cm^{-2}; view angles between nadir and 75°; and lowest layer temperature range from 286 K to 305 K.

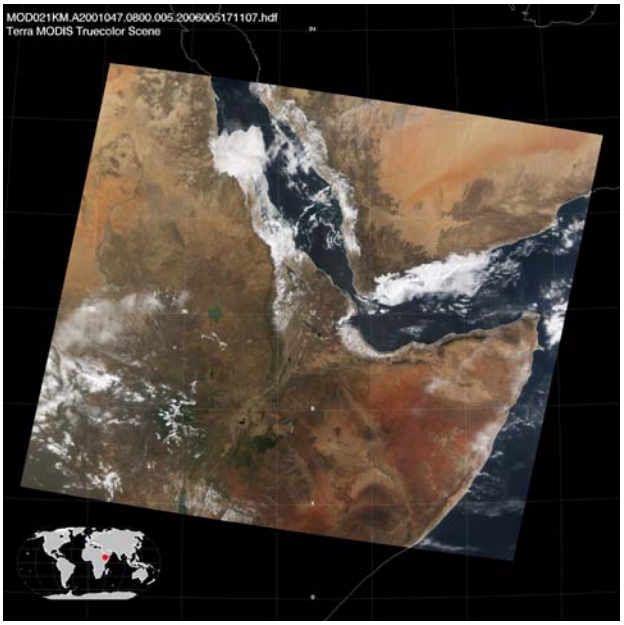

Figure 2.1: Quicklook image of the Terra MODIS granule centered at 12°N 42°E; used in the parametric model evaluation (Section 2.3) and the subsequent results plotted below (Fig. 2.2-2.7).

In a nominal MODIS granule, approximately 600 atmospheric profiles are available because NCEP provides profiles on a regular basis: 1 degree in latitude by 1 degree in longitude. For each of these profiles, with local observation conditions of MODIS, results of the parametric model were compared to results of MODTRAN (Figures 2.2, 2.3, and 2.4). Without interpolation of the atmospheric profile, both MODTRAN and the parametric model use the same atmospheric data. Therefore, the performances of the parametric model can be assessed without perturbations from atmospheric data.

A good agreement (E = 0.9) was shown between MODTRAN and the parametric model for upward radiance, downward radiance, and transmittance derived from MODIS MIR and TIR bands (Table 2.3). Examination of the bias and precision showed the model retrievals match closely with MODTRAN. Band 31 had the best

agreement. This was ideal since MODIS band 31 is selectively placed, in terms of wavelength, to minimize atmospheric perturbation. On the other hand, band 29 showed the least favorable agreement between the parametric model and MODTRAN and highlights an area to improve upon the model. While Figures 2.2, 2.3, and 2.4 show the comparison of radiative transfer variables retrieved from the model and MODTRAN for MODIS bands 31 (11μm) and 32 (12μm), all of the MODIS emissive thermal bands were assessed in this section. However, particular attention was given to the two MODIS bands commonly used in surface temperature retrieval schemes; band 31 (single-channel temperature retrieval and split-window) and band 32 (split-window). In addition, attention was focused on MODIS band 31 because its spectral placement was intended to minimize atmospheric perturbation and is unaffected by solar reflection during daytime observations. Thus, if the model is to prove effective it must be accurate for MODIS band 31.

Computation speed was assessed between MODTRAN and the parametric model for retrieval of correction parameters upward radiance, downward radiance, and transmittance. Multiple trials, all conducted on the same computer (Intel Pentium 4, 2800 Hz, 512 KB cache, 1.1GB RAM, Linux 2.4.22), showed that the parametric model was well over 3 orders of magnitude faster than MODTRAN. For example, for 621 profiles (approximately 28 vertical layers each) analysis of the all 7 emissive bands by the model took ~2 seconds while MODTRAN took ~5800 seconds (Table 2.4). Extending this example to the estimated 288 MODIS granules produced per day

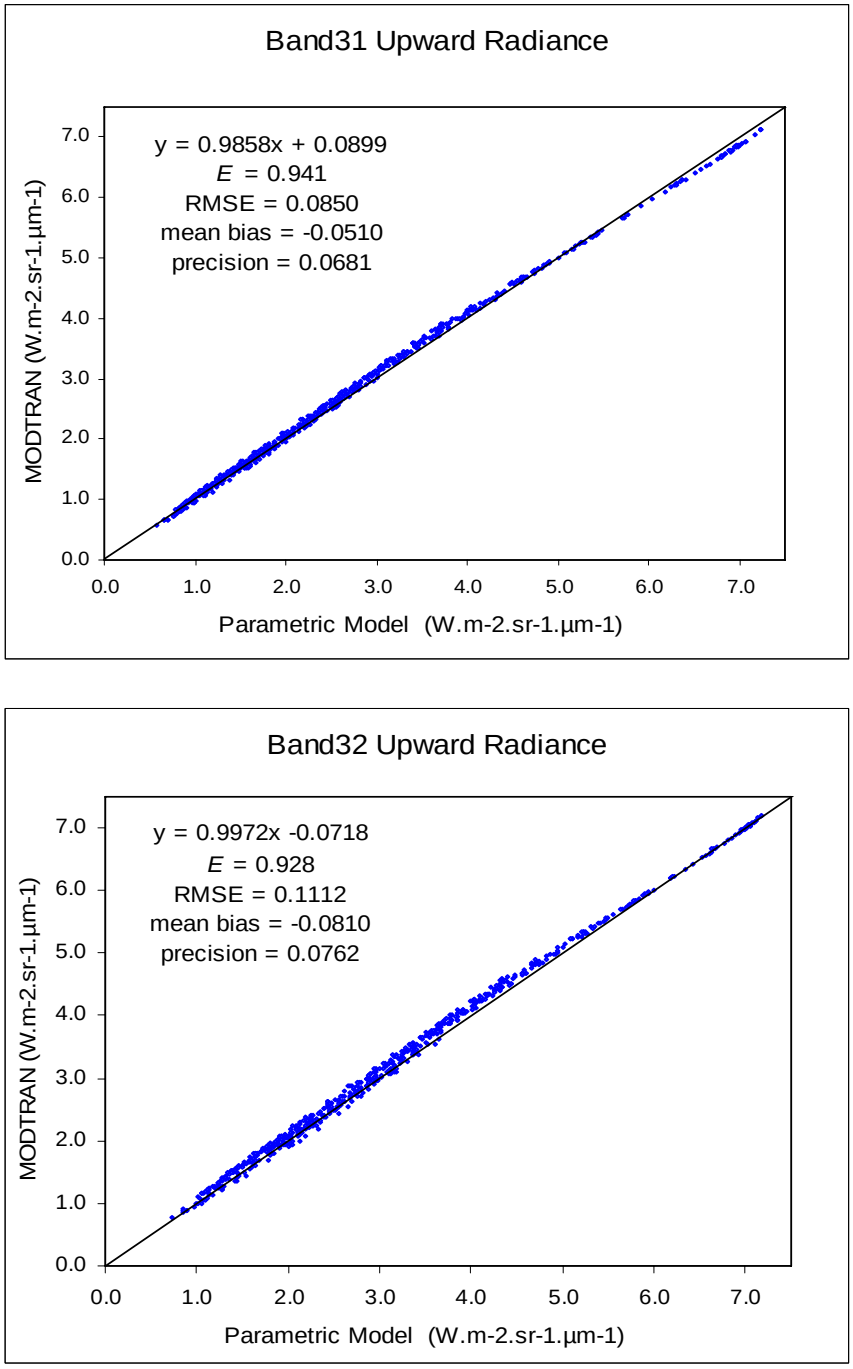

Figure 2.2: Relationship between MODTRAN and the parametric model derived upward radiance for MODIS bands 31 (11.0186µm) and 32 (12.0325µm). Deviation from the trend line for large upward radiances corresponds with large incidence angles and hot/moist profiles. In these cases biases are expected due to bending of the optical path which is not accounted for in the parametric model (see Section 2.4).

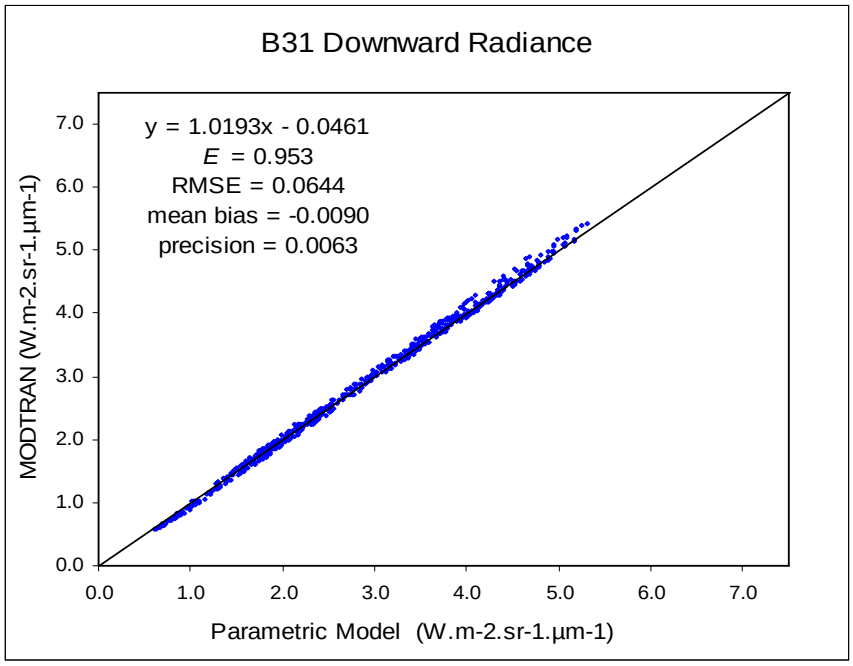

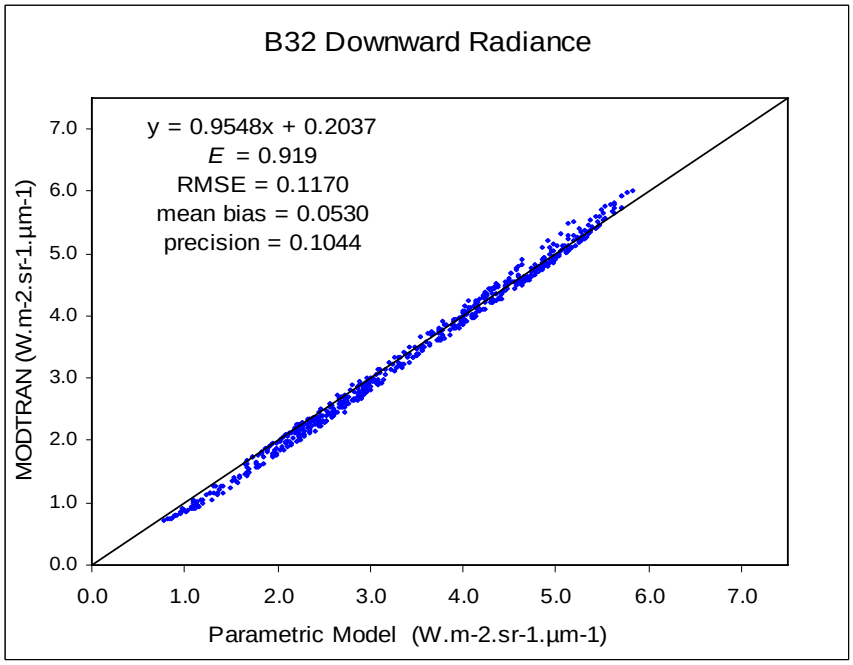

Figure 2.3: Relationship between MODTRAN and the parametric model derived downward radiance for MODIS bands 31 (11.0186µm) and 32 (12.0325µm). Deviation from the trend line for large upward radiances corresponds with large incidence angles and hot/moist profiles. In these cases biases are expected due to bending of the optical path which is not accounted for in the parametric model (see Section 2.4).

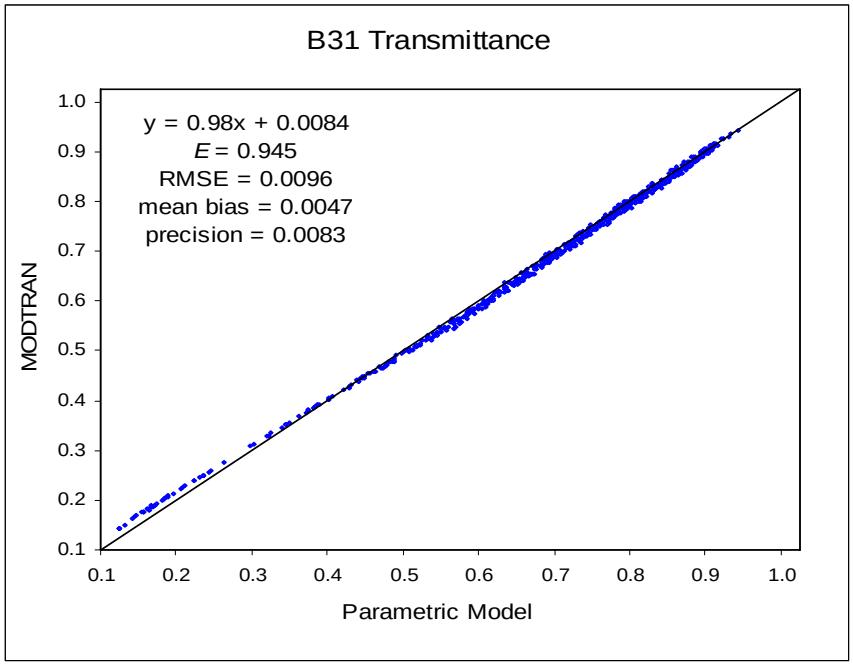

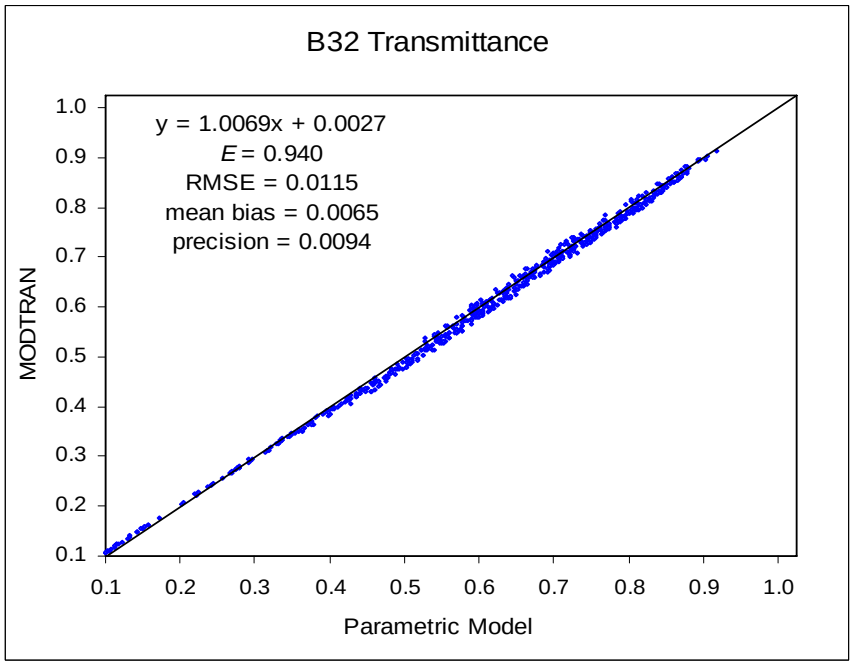

Figure 2.4: Relationship between MODTRAN and the parametric model derived transmittance.

Table 2.3: Preliminary evaluation of radiative transfer variables (a) transmittance, (b) upwelling radiance, and (c) downwelling radiance was based on comparison of the parametric model and MODTRAN retrievals for MODIS thermal bands (20-23, 29, 31, and 32). Radiance values are in W m^{-2} sr^{-1} μm^{-1}.

a.

Trans	Band	***E***	***RMSE***	***mean bias***	***precision***
MIR	20	0.8810	0.0130	0.0007	0.0034
	21	0.9880	0.0017	0.0002	0.0017
	22	0.9840	0.0019	0.0001	0.0019
	23	0.9790	0.0046	0.0021	0.0041
TIR	29	0.9110	0.0118	0.0049	0.0107
	31	0.9450	0.0096	0.0047	0.0083
	32	0.9400	0.0115	0.0065	0.0094

b.

Up	Band	***E***	***RMSE***	***mean bias***	***precision***
MIR	20	0.8660	0.0034	0.0004	0.0034
	21	0.9850	0.0005	-0.0002	0.0005
	22	0.9680	0.0008	0.0001	0.0008
	23	0.9840	0.0008	-0.0004	0.0007
TIR	29	0.8610	0.1318	0.0735	0.1094
	31	0.9410	0.0850	-0.0510	0.0681
	32	0.9280	0.1112	-0.0810	0.0762

c.

Down	Band	***E***	***RMSE***	***mean bias***	***precision***
MIR	20	0.6420	0.0061	0.0033	0.0084
	21	0.9260	0.0009	0.0002	0.0010
	22	0.8860	0.0012	0.0010	0.0021
	23	0.8060	0.0043	0.0029	0.0066
TIR	29	0.7470	0.2112	-0.0974	0.1876
	31	0.9530	0.0644	-0.0090	0.0663
	32	0.9190	0.1170	0.0530	0.1488

highlights the significance in processing speed, especially as it relates to operational processing. Assuming a conservative number of clear sky NCEP profiles (~300, less than half of what are typically analyzed) available from the above analysis and extending that to the 288 daily MODIS granules results in a processing time of nearly 10 days for MODTRAN and less than 5 minutes for the parametric model. In addition, consideration must be given to the fact that preliminary analysis was performed for profiles at the NCEP resolution (1° x 1°) and not MODIS (1km) in order to avoid introducing error from profile interpolation. Therefore, it can be realized that performing atmospheric correction operationally at MODIS TIR band resolution would be unrealistic with RT models such as MODTRAN and but can be achieved with an accurate and "fast" RTM.

Table 2.4: Computation time for MODTRAN and parametric model; comparison is based on multiple runs of a single granule on the same machine. Program execution was performed independent of each other (i.e. the model or MODTRAN is the only process running at the time on the machine).

	time in seconds	
#	MODTRAN	PM
1	5835.42	1.52
2	5956.15	1.83
3	5798.53	2.31
4	5772.33	1.75
5	5970.44	1.89
6	5959.38	1.77
7	5802.09	1.52
8	5913.51	1.52
9	5883.26	1.52
10	5840.35	1.5
mean	5873.15	1.71

2.5 Assessment of the Parametric Model Surface Brightness Temperature Calculations Using a Synthetic Dataset

The intention of this section was to evaluate the calculation of surface brightness temperature using realistic surface and simulated TOA radiance values, and the correction parameters generated from MODTRAN and the parametric model. Surface brightness temperature (SB(*T*)) was calculated for each of the NCEP atmospheric profiles introduced in the previous section. Simulated surface temperatures (*T*) were obtained from the temperature at the lowest atmospheric profile layer. The derivation of a realistic surface brightness temperature employed the Planck function, emissivity, and the assumed skin temperature, and was convolved with the MODIS band equivalent wavelength. The first step required calculating simulated surface radiance values:

$$L_i\left(T_{surf,i}\right)=\varepsilon_i\frac{\frac{c_1}{\lambda_i^5}}{\exp\left(\frac{c_2}{\lambda_i T_{bot}}\right)-1}\ [\mathrm{W.m^{-2}.sr^{-1}.\mu m^{-1}}] \qquad (2.22)$$

Where C_1 and C_2 are radiation constants ($1.1911 \cdot 10^{-8}$ W•m^{-2}•sr^{-1}•μm^4 and $1.4388 \cdot 10^4$ K μm, respectively), T_{bot} is the lowest profile layer reported temperature (here used as synthetic skin temperature), and λ_i is the MODIS band equivalent wavelength (Table 2.2). To account for surface emissivity (ε_i), surface radiance were calculated using emissivity values typical for surfaces observed in TIR (0.98, 0.99, and 1.0). Measured at-sensor brightness temperatures were simulated using atmospheric transmittance ($t_{\mathrm{mod},i}$), upward radiance ($L_{\mathrm{mod}\ atm\uparrow i}$), and downward radiance (L_{mod}

$_{atm\downarrow i}$) computed by MODTRAN, along with the surface radiance calculated above equation (2.22), using the following formula:

$$L_i\left(T_{toa,i}\right) = t_{\mathrm{mod},i}[L_i\left(T_{surf,i}\right) + (1-\varepsilon_i)L_{\mathrm{mod}\,atm\downarrow i}] + L_{\mathrm{mod}\,atm\uparrow i} \tag{2.23}$$

Atmospherically corrected transmittance, upward radiance, and downward radiance values were then generated by the proposed parametric model, and used along with simulated TOA radiance from (2.23) to calculate the surface radiance:

$$L_i\left(T^*_{skin,i}\right) = \left[\frac{L_i\left(T_{toa,i}\right) - L_{\mathrm{PM}\,atm\uparrow i}}{t_{PM,i}} - (1-\varepsilon_i)L_{\mathrm{PM}\,atm\downarrow i}\right] / \varepsilon_i \tag{2.24}$$

Where $L_i(T_{toa,i})$ is the TOA radiance from (2.23), $L_{PM\ atm\uparrow,i}$ is the parametric model generated upward atmospheric radiance, $t_{PM,i}$ is the parametric model generated atmospheric transmittance, and (1-ε) $L_{atm,i\downarrow}$ is the second order term accounting for downward atmospheric radiance.

Finally, a comparable surface skin temperature is calculated by inverting the Planck function again, this time for $L_i(T^*_{skin,i})$ from (2.24). In MODTRAN, bending of the optical path is accounted for when the view angle is greater than 60 degrees, but not in the proposed model. In such cases, the sensor does not actually "see" the surface and even small errors in atmospheric transmittance or atmospheric upward radiance have a large impact on surface brightness temperature. Therefore observations above 60° were excluded. Figure 2.5 shows a plot of the model calculated skin temperature against the synthetic skin temperatures for the MODIS

a.

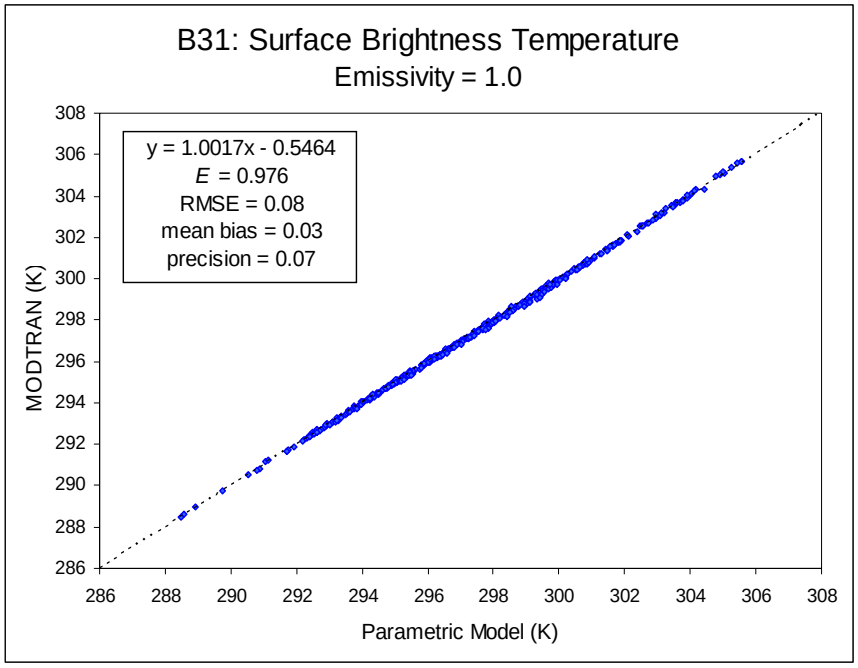

b.

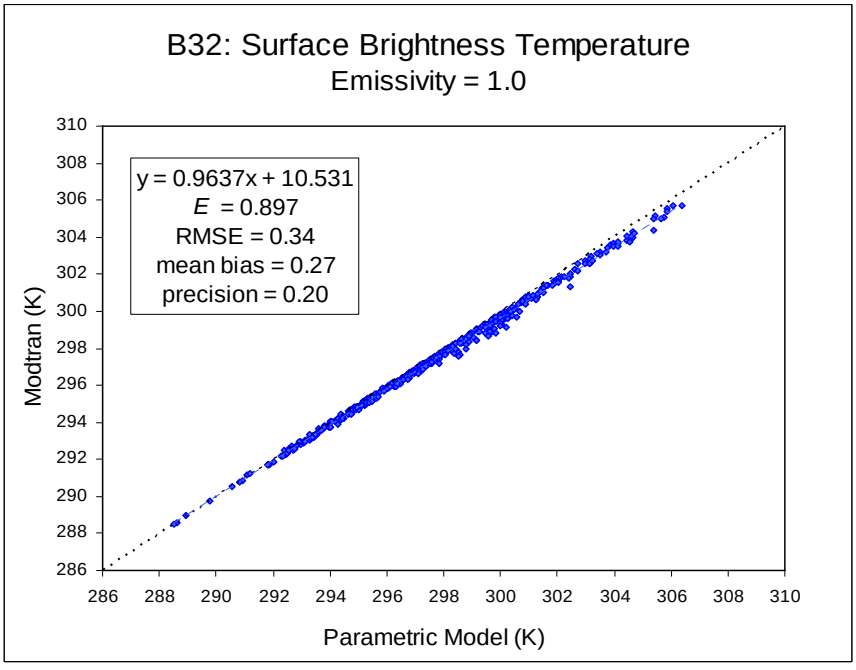

Figure 2.5: Surface brightness temperatures comparison between the parametric model and MODTRAN for MODIS bands 31 (a) and 32 (b), excluding any MODIS observations with view angles greater than 60° (n=423). Emissivity was set to unity. The 1:1 (dashed) line is plotted for reference.

a.

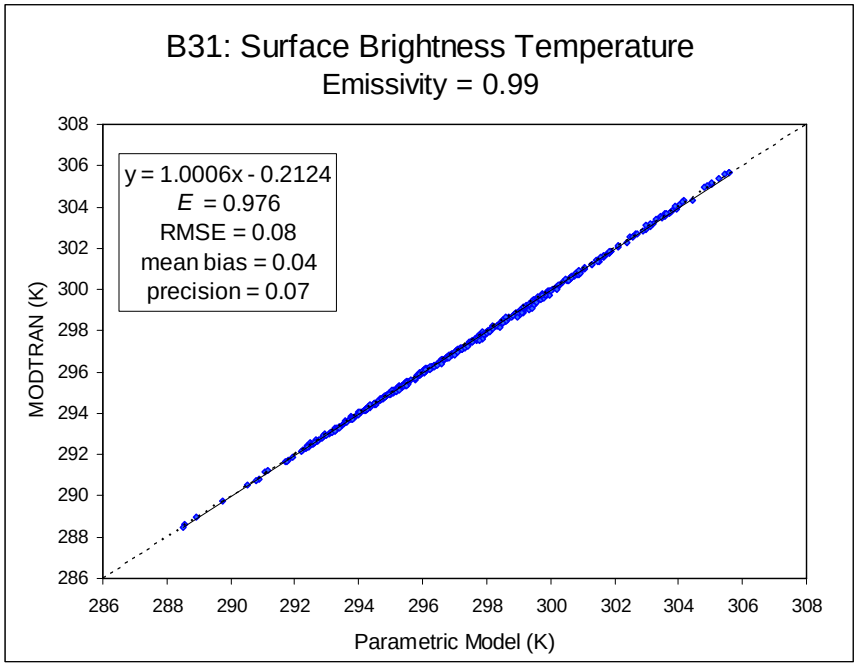

b.

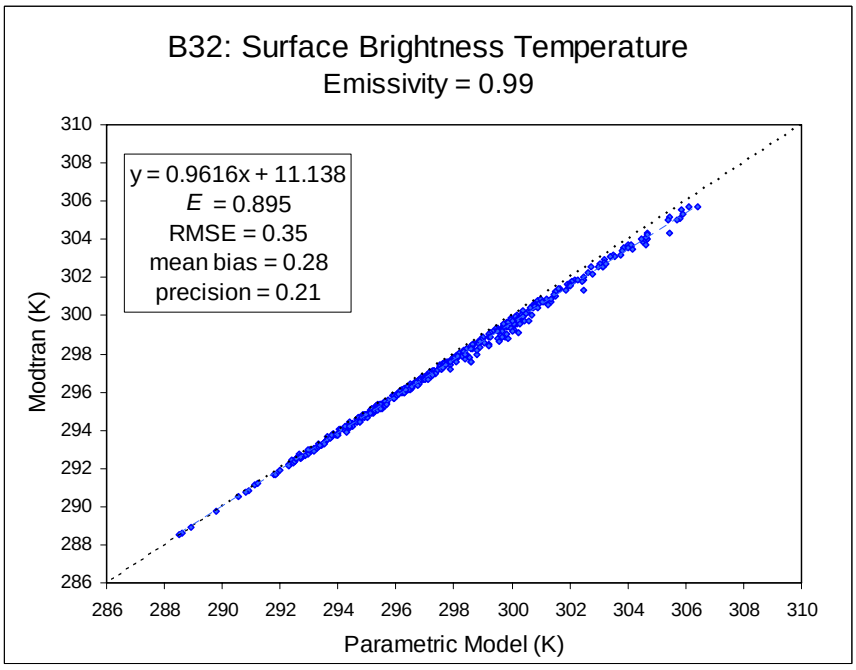

Figure 2.6: Surface brightness temperatures comparison between the parametric model and MODTRAN for MODIS bands 31 (a) and 32 (b), excluding any MODIS observations with view angles greater than 60° (n=423). Emissivity was set to 0.99. The 1:1 (dashed) line is plotted for reference.

a.

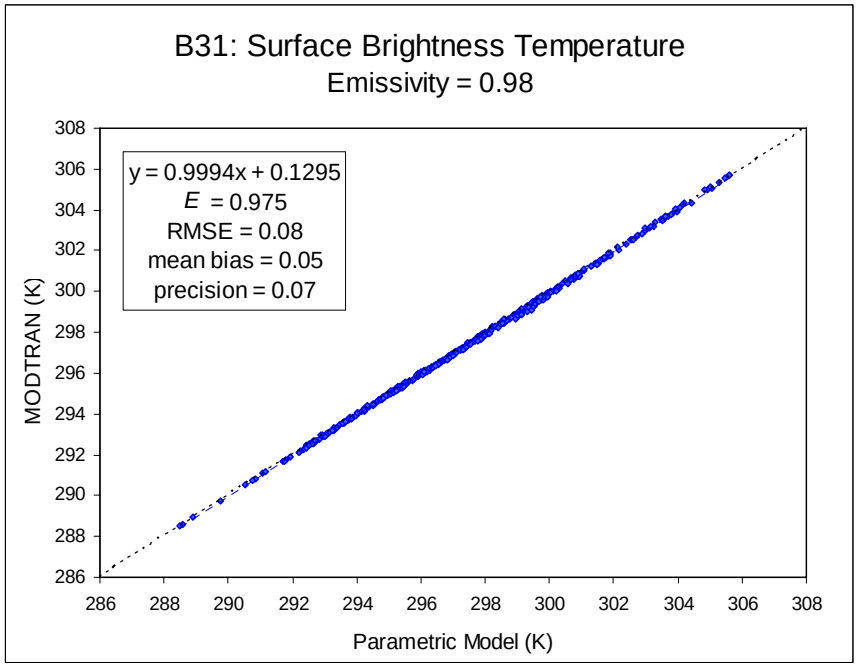

b.

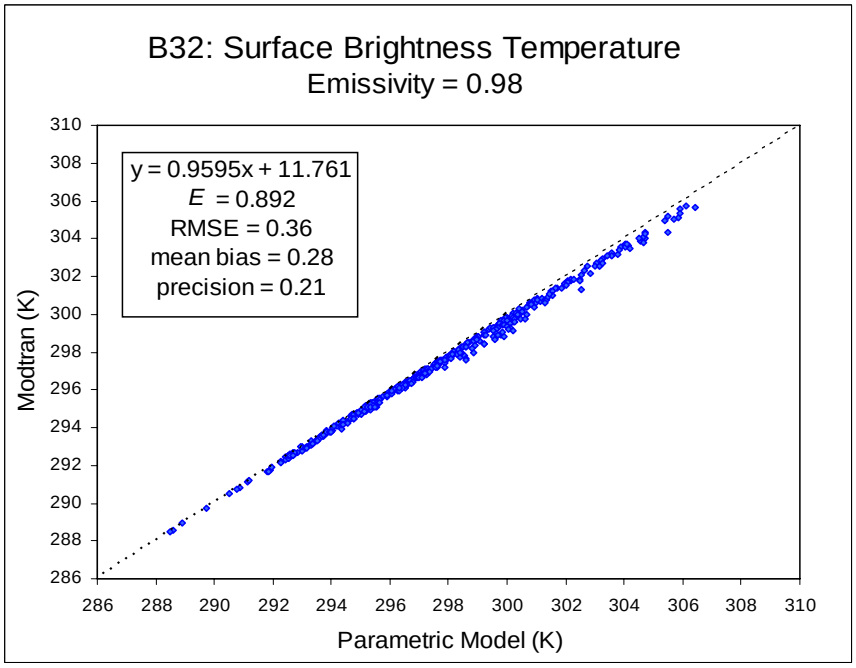

Figure 2.7: Surface brightness temperatures comparison between the parametric model and MODTRAN for MODIS bands 31 (a) and 32 (b), excluding any MODIS observations with view angles greater than 60° (n=423). Emissivity was set to 0.98. The 1:1 line (dashed) is plotted for reference.

granule observations in bands 31 and 32; emissivity was assumed to be unity. Additional emissivity values included 0.99 and 0.98 to represent realistic surface emission values for thermal infrared bands 31 and 32 (Figures 2.6 and 2.7).

Table 2.5 shows the performance of the parametric model for the 7 emissive bands analyzed (MODIS channel# 20-23, 29, 31, and 32). The performance of the model was also assessed when the surface temperature was assumed to be +/- 5K from the NCEP profile lowest layer temperature at each observation point. The results for this additional comparison are shown in Table 2.6. With exception of band 29, the results across the MIR and TIR bands examined in this study showed a good agreement ($E \sim 0.9$) and low error (RMSE < 0.4 K) across all emissivity values. For example, the bias for band 31 was small (< 0.1 K) for the three emissivity values, while band 32 had a similar degree of bias when emissivity was unity, but increased to 0.29 K when emissivity was set to 0.98. It is clear that as emissivity decreases from unity to 0.98 that a small increase in error and bias occurs. Greater accuracy and precision is exhibited in band 31comparisons and is likely the result of the placement of this band in an atmospheric window, thus reducing the effects of water vapor attenuation.

2.6 SST Evaluation

Evaluation of the accuracy of the parametric model proceeded with a comparison of an independent measure of temperatures. Since the split-window approach is accepted to be fairly accurate over water targets (± 0.5 K [*McClain et al.,* 1985; *Barton,* 1995; *Merchant and LeBorgne,* 2004]), due largely to stable emissivity, the

parametric model surface temperatures were compared with the current Aqua-MODIS SST product (MYD28). Given the standard deviation in SST temperature

Table 2.5: Statistical results for the evaluation of surface temperature calculations using the parametric model atmospheric correction parameters (transmittance, upward radiance, and downward radiance). Surface temperature is assumed to be the same as the lowest layer of the NCEP profile for each observation point (n = 421). Results are shown for emissivity values of 1.0, 0.99, and 0.98 and for 7 thermal bands MODIS bands (20-23, 29, 31, and 32).

1.00	Band	***E***	***RMSE***	***mean bias***	***precision***
MIR	20	0.988	0.038	0.024	0.030
	21	0.995	0.014	0.012	0.007
	22	0.998	0.006	-2.5E-04	0.005
	23	0.994	0.024	-2.8E-04	0.239
TIR	29	0.684	0.879	-0.833	0.282
	31	0.976	0.080	0.034	0.073
	32	0.897	0.335	0.267	0.202

0.99	Band	***E***	***RMSE***	***mean bias***	***precision***
MIR	20	0.989	0.037	0.022	0.030
	21	0.995	0.014	0.012	0.007
	22	0.998	0.006	-3.1E-04	0.005
	23	0.994	0.024	-7.6E-04	0.024
TIR	29	0.686	0.877	-0.828	0.290
	31	0.966	0.106	0.083	0.067
	32	0.895	0.346	0.277	0.208

0.98	Band	***E***	***RMSE***	***mean bias***	***precision***
MIR	20	0.989	0.036	0.021	0.030
	21	0.995	0.014	0.012	0.007
	22	0.998	0.006	-3.6E-04	0.005
	23	0.994	0.024	-1.3E-04	0.024
TIR	29	0.688	0.876	-0.823	0.299
	31	0.975	0.084	0.050	0.068
	32	0.892	0.356	0.285	0.214

Table 2.6: Comparison of RMSE results for 7 thermal MODIS channels and 3 different emissivity values. RMSE is based on the evaluation of surface temperature calculations using the parametric model derived correction parameters and an assumed surface temperature. In this table, the RMSE values highlight the effect of adjusting the assumed surface temperature (lowest layer temperature from the NCEP profiles) by either adding (a) or subtracting (b) 5K to the lowest layer temperature at each observation point (n = 421). The first column indicates the emissivity value used in the surface temperature calculations. The second column indicates the MODIS band number. The third column is the RMSE for the adjusted (±5K) assumed surface temperature. The fourth column is the RMSE for the original surface temperature calculations; again, using the lowest layer temperature of the NCEP profile at each observation point. The fifth column demonstrates the difference in between RMSE values in columns 3 and 4 (adjusted versus original).

1.00	Band	**adj +5K**	**original**	**diff**
MIR	20	0.060	0.038	-0.022
	21	0.014	0.014	0.000
	22	0.006	0.006	0.000
	23	0.024	0.024	0.000
TIR	29	0.864	0.879	0.015
	31	0.096	0.080	-0.016
	32	0.253	0.335	0.082

0.99	Band	**adj +5K**	**original**	**diff**
MIR	20	0.058	0.037	-0.021
	21	0.014	0.014	0.000
	22	0.006	0.006	0.000
	23	0.024	0.024	0.000
TIR	29	0.861	0.877	0.016
	31	0.089	0.106	0.017
	32	0.259	0.346	0.087

0.98	Band	**adj +5K**	**original**	**diff**
MIR	20	0.057	0.036	-0.020
	21	0.014	0.014	0.000
	22	0.006	0.006	0.001
	23	0.025	0.024	0.000
TIR	29	0.856	0.876	0.019
	31	0.083	0.084	0.001
	32	0.266	0.356	0.091

a.

1.00	Band	**adj -5K**	**original**	**diff**
MIR	20	0.032	0.038	0.006
	21	0.014	0.014	0.000
	22	0.009	0.006	-0.003
	23	0.024	0.024	0.000
TIR	29	0.907	0.879	-0.028
	31	0.127	0.080	-0.046
	32	0.444	0.335	-0.109

0.99	Band	**adj -5K**	**original**	**diff**
MIR	20	0.034	0.037	0.003
	21	0.014	0.014	0.000
	22	0.010	0.006	-0.004
	23	0.024	0.024	0.000
TIR	29	0.907	0.877	-0.030
	31	0.177	0.106	-0.071
	32	0.456	0.346	-0.110

0.98	Band	**adj -5K**	**original**	**diff**
MIR	20	0.036	0.036	0.000
	21	0.014	0.014	0.000
	22	0.010	0.006	-0.004
	23	0.025	0.024	0.000
TIR	29	0.907	0.876	-0.031
	31	0.141	0.084	-0.057
	32	0.467	0.356	-0.111

b.

retrievals and lacking *in situ* measurements, this analysis was used as a general comparison of temperature estimates as it is impossible to assume which is absolutely correct. The intention was to assess the consistency between the SST product and the results derived using the parametric model.

The MYD28 Level 2 product is produced daily at 1km resolution for day and night observations and available through the Ocean Color Data Processing System (http://oceancolor.gsfc.nasa.gov). MODIS per channel radiance values were retrieved from the MYD02 (L1B), calibrated, geolocated, 1km resolution product. Figure 2.8 shows Quicklook images of the granules used for this comparison.

This offered the necessary radiance values and view angles for the parametric model input. For atmospheric profile data, the MODIS atmosphere product (MYD07)[2] was used. The MYD07 product consists of several key variables necessary for radiative transfer modeling including temperature, moisture profiles, and standard pressure levels. These parameters are recorded in 20 vertical layers. This product is also generated daily, for day and night observations, at 5km horizontal resolution when at least 9 fields of view (FOV) are cloud free. The validation of sea surface temperature included 82 near-nadir Aqua-MODIS observations. The selection of near-nadir observations was intended to avoid any additional errors from angular effects. Results demonstrated a low RMSE (<0.5 K) and bias of -0.45 K (Figure 2.9). The precision was 0.19 K, suggesting that the bias is systematic and consistency between temperatures exists. The accuracy and precision is encouraging, as it showed that the model agrees well on a point-to-point basis.

---

[2] http://modis-atmos.gsfc.nasa.gov/_docs/MOD07:MYD07_ATBD_C005.pdf

a.

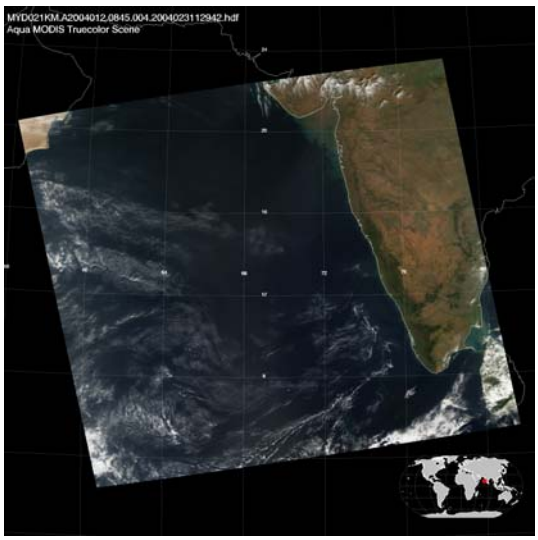

b.

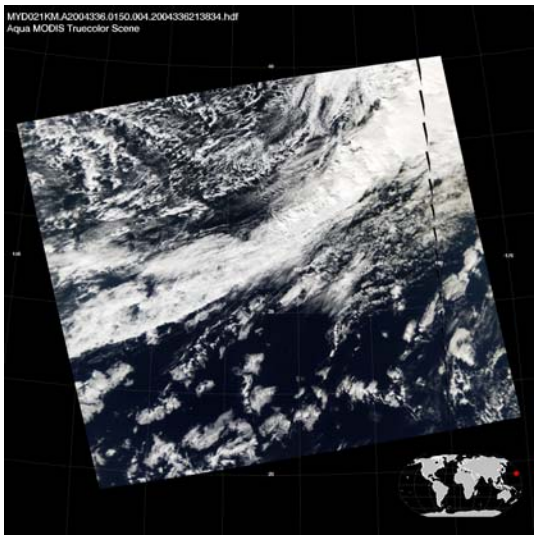

c.

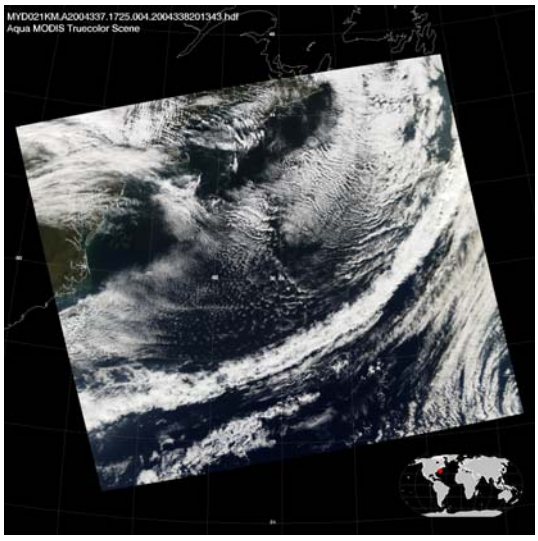

Figure 2.8: Quicklook images of the Aqua MODIS granules used in the SST comparison section (Section 2.6) and the results plot (Fig. 2.9): (a) granule 2004.012.0645 centered at 14°N, 70°E; (b) 2004.336.0150 centered at 30°N, 170°E; (c) 2004.337.1725 centered at 36°N, 64°W. Granule nomenclature indicates year.doy.hhmm, where doy is the day of year and hhmm is the time in hours-minutes (UTC).

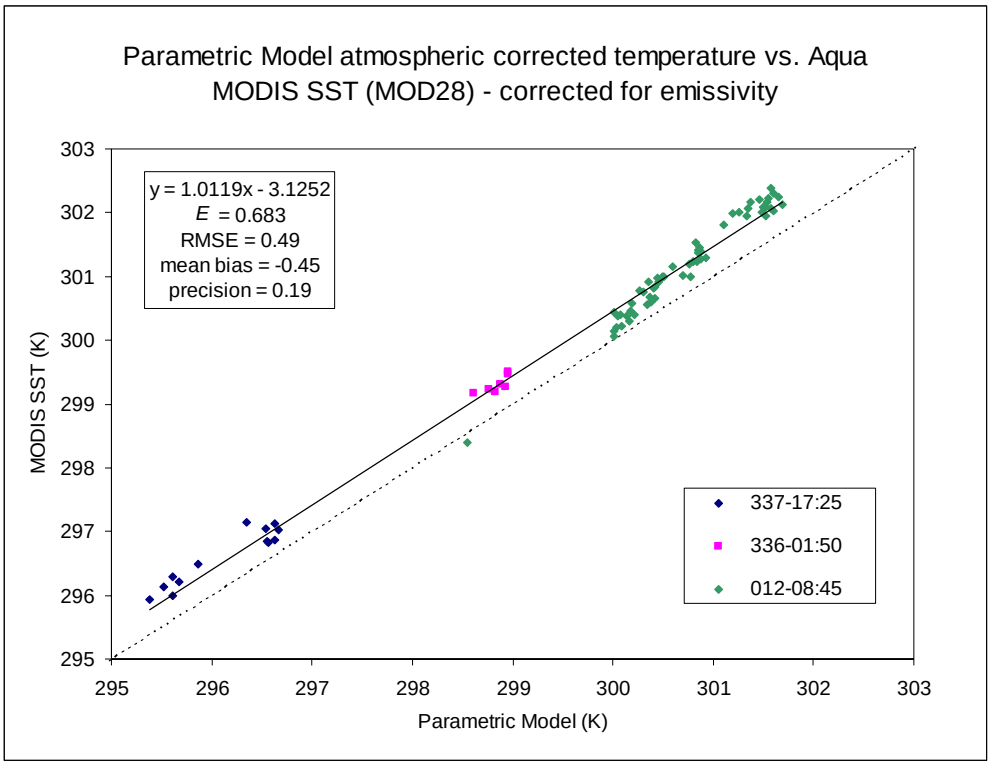

Figure 2.9: Comparison of the atmospherically corrected sea surface temperatures using the parametric model (MODIS band 31) versus the Aqua-MODIS sea-surface temperature product (MYD28). Since emissivity correction is performed for the MODIS SST product, emissivity was accounted for as well when deriving surface temperatures with the parametric model. An emissivity of 0.995 was assumed; generally accepted as a standard sea surface emissivity for MODIS band 31. Near-nadir observations are from 2004 (n = 78) with blue points corresponding with day of year (DOY) 337 at 17:25 UTC; magenta with DOY=336 at 01:50 UTC; and green with DOY=012 at 08:45 UTC. The 1:1 (dashed) line is plotted for reference.

2.7 *In situ* Validation

Ground based surface skin temperature measurements obtained with *in situ* radiometers provided the opportunity to evaluate the accuracy of the parametric model against real surface skin temperatures that have not been derived through other modeling schemes (e.g. the SST product from MODIS). *In situ* data from two studies

were used; one representing lake body targets and the other agricultural land surface temperatures.

In the first case, observations were made over Lake Tahoe, California/Nevada, using radiometers located on 4 permanently moored buoys (Figure 2.10) [*Hook et al.,* 2007]. Each radiometer has been tested and calibrated to National Institute of Standards and Technology (NIST) acceptable levels corresponding with an accuracy of better than ±0.2 K [*Barton et al.,* 2004]. Temperatures are continually recorded at 2 minute intervals, thus allowing for coincident observations with MODIS overpasses (n = 30). View angles ranged from 0.24° to 11.79°, while water vapor content ranged from 0.24 to 1.94 g cm^{-2}. Emissivity was obtained from the ASTER spectral library (http://speclib.jpl.nasa.gov). For a complete description of the study site, *in situ* observation methods, and results to validate satellite sensors see: [*Hook et al.,* 2003; *Hook et al.,* 2004; *Hook et al.,* 2005; *Tonooka et al.,* 2005].

Validation with land surface temperature observations were made with data provided by [*Coll et al.,* 2005]. Measurements were made with tripod mounted radiometers placed over stable, homogeneous sites in eastern Spain (Figure 2.11). Accuracy of the radiometer measurements was periodically checked against a calibrated blackbody and was consistently ±0.2 K. The box-method (*Rubio*, 2003) was used to obtain site specific emissivity. Four radiometers were assigned to each corner of the 1km study sites and carried along transects 100m long to obtain a mean LST temperature. Standard deviations of averaged transect radiometer temperature measurements showed minimal variation ($\sigma < \pm 0.5$ K) and therefore each site, as well as the study area, was assumed to be homogeneous. These ground based LST

measurements were collected within a 20 to 30 minute period centered at the overpass of MODIS Terra (n = 5) and only temperatures measured within 3 minutes of the satellite overpass were used for comparison.

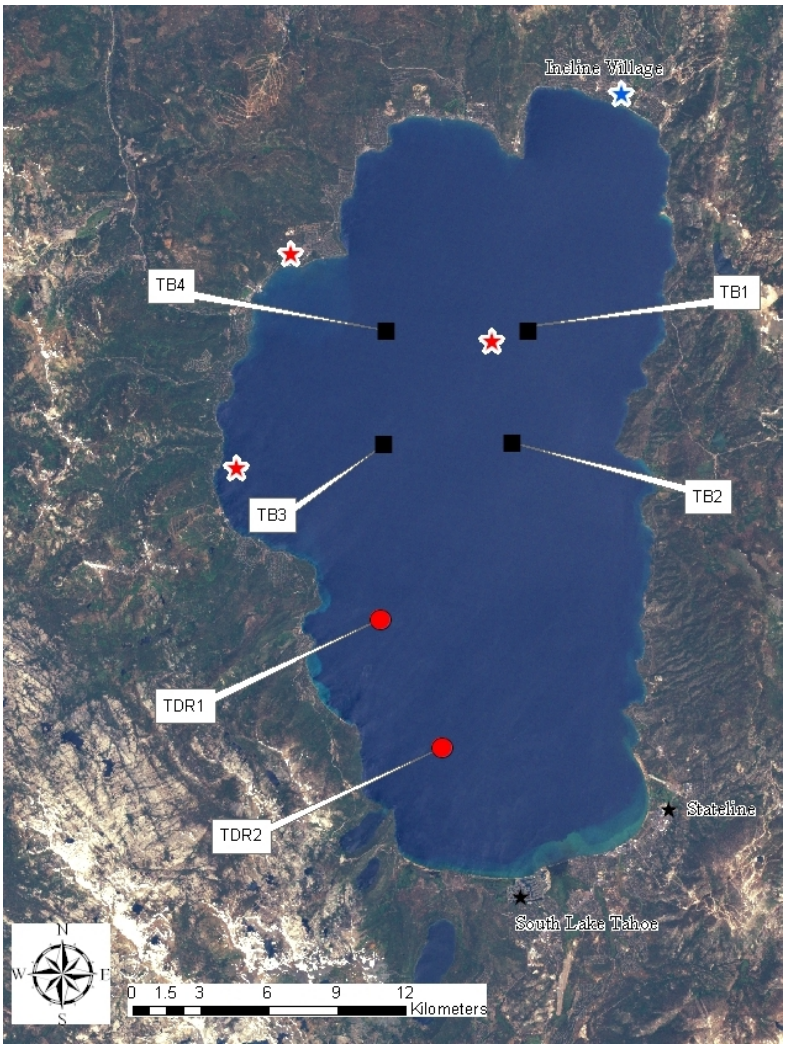

Figure 2.10: Lake Tahoe, California/Nevada showing the 4 National Aeronautics and Space Agency (NASA) buoys labeled as TB1, TB2, TB3 and TB4 (Tahoe Buoy #). Water properties are measured at the Midlake (star near TB1) and the Index station (star west of TB3). Meteorological measurements have been made at both Incline (blue star) and the USCG site (red stars northwest of TB4). University of California at Davis also maintains two additional floats (rafts) in the southern part of Lake Tahoe (TDR1 and TDR2) which measure meteorological variables and bulk temperature. South Lake Tahoe and Stateline towns are shown for reference (black stars).

View angles ranged from 5.47° to 27.78° and water vapor concentration ranged from 1.35 to 2.68 g cm^{-2}. A full description of the study site and methods can be found in [*Coll et al.,* 2005]. For both comparison cases MODIS (MYD07) profiles, retrieved at coincident observation times and locations to *in situ* temperature measurements were used in the parametric model to generate the necessary variables to estimate temperatures. Emissivity values for both site surface types were retrieved from the ASTER spectral library and based on the centroid value of the spectral response function in bands 31 and 32. Lake Tahoe emissivity was set to 0.991 for band 31 and 0.985 for band 32, while the agriculture site emissivity was set to 0.984 and 0.989 for band 31 and 32, respectively. Emissivity for agricultural surface types is not explicitly available from the ASTER spectral library so instead the emissivity listed for grass was used. Comparison between the emissivity used by [*Coll et al.,* 2005] of 0.985 and the emissivity values retrieved from the library showed they are quite similar. The comparison between the model and *in situ* temperature measurements showed a good agreement (MODIS band 31: E = 0.86, RMSE = 0.53 K; band 32: E = 0.78, RMSE = 0.84 K), with a slight systematic underestimation of the surface temperature by the model (band 31 bias = -0.22 K; band 32 bias = -0.42 K). The precision, however, showed that the standard deviation in the bias was nearly two times greater (band 31 precision = 0.49 K; band 32 precision = 0.76 K), indicating that on an individual basis, improper characterization of the atmospheric conditions and/or emissivity may exist. Figure 2.12 shows the plot of the temperature retrievals between the model and *in situ* observations for band 31 and 32.

A limited number of coincident observations (30 for Lake Tahoe, 5 for Valencia) were available for *in situ* comparison and therefore future investigations should include more data. Nevertheless, the analysis includes a range of temperatures for two discrete surface conditions with results that are encouraging.

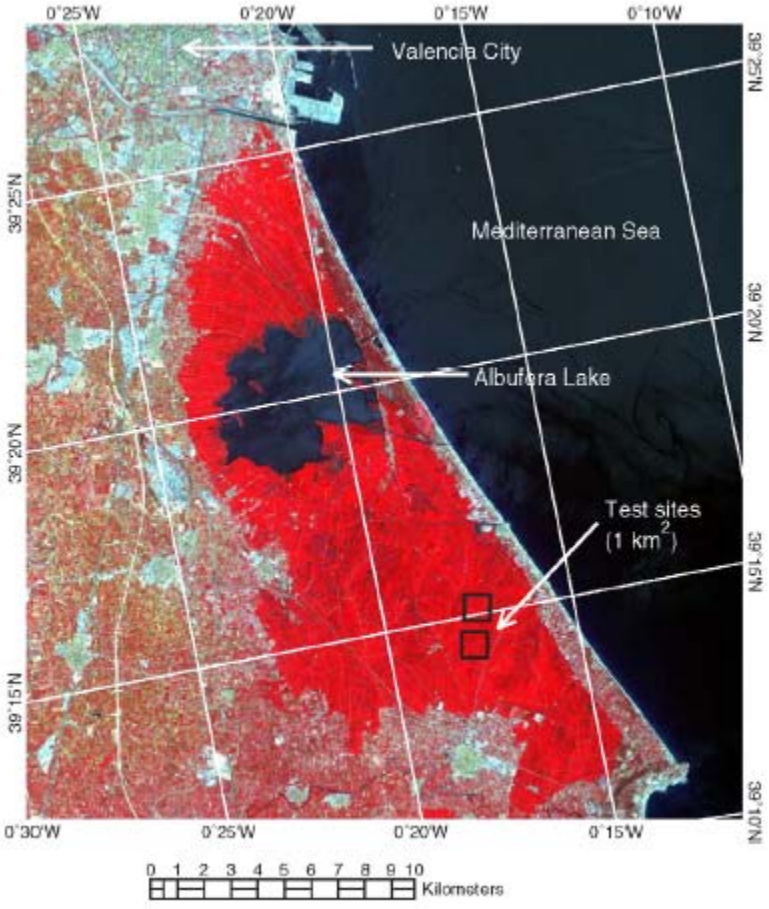

Figure 2.11: Study sites used for measurement of LST. *In situ* data were recorded along transects within flat, homogeneous plots consisting of cultivated rice fields. The above image is an ASTER color composite (R=0.81μm; G=0.66μm; B=0.56μm) from August, 2004. Courtesy of César Coll.

a.

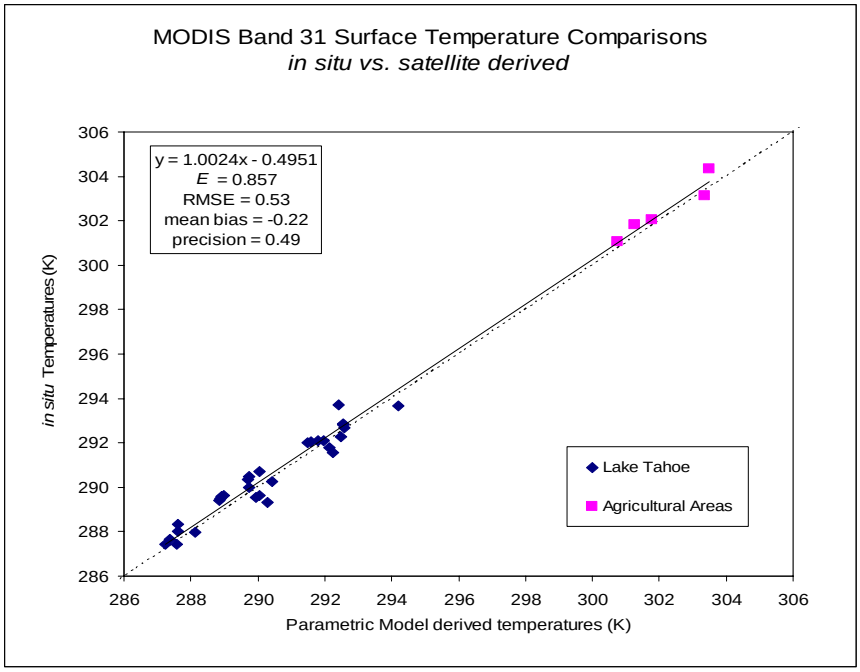

b.

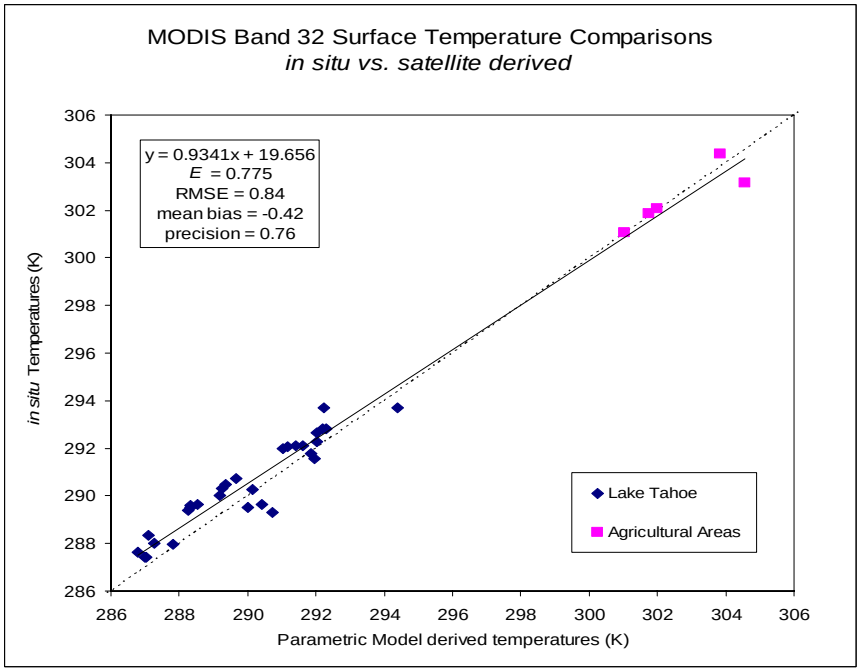

Figure 2.12: Comparison of surface temperatures derived from *in situ* radiometric measurements versus the parametric model derived temperatures for (a) band 31, and (b) band 32. Emissivity values used for the model calculated temperatures were retrieved from the ASTER spectral library. For Lake Tahoe, represented by the blue diamonds, was set to 0.991 and 0.985, while emissivity for the agricultural site was 0.984 and 0.989 (band 31 and 32, respectively). The MODIS atmosphere product (MOD07) was used for the atmospheric profile input data in the parametric model. The 1:1 line (dashed) is shown for reference.

2.8 Evaluating Atmospheric Effects on MODIS FRP Retrievals

The process of combustion releases energy through several pathways including conduction, convection, vaporization, and radiation. The MODIS sensor estimates the rate of radiative energy emitted from biomass burning, referred to as the fire radiative power (FRP, units in MW), using an empirical relationship relating the difference in the "fire pixel" and "background pixel" 4 μm brightness temperatures [*Kaufman et al.,* 1998]. The middle infrared (MIR) channel is ideally suited for several reasons: (1) typical fire temperatures (600 - 1200K) correspond with large amounts of black-body radiation which, according to Planck's Law, peak in this spectral region; (2) separation between fire and background temperatures is clearly distinguishable, and; (3) the MODIS 4 μm channel is situated in an "atmospheric window" to minimize perturbation. Nonetheless, some portion of energy will be lost to atmospheric attenuation, primarily due to N_2, CO_2, and water vapor [*Kaufman et al.*, 1998]. In the following section simulated fires were examined to evaluate what this loss of energy is and potential adjustments needed to the FRP measurements.

Simulated fires were comprised of 3 temperature components including a flaming (T_f) portion, a smoldering (T_s) portion, and the background (T_b) portion. Temperatures for each component were adopted from *Kaufman et al.* [1998] and randomly chosen within a specific range: 700-1300 K for T_f; 400-600 K for T_s; and 280-320 K for T_b. The fraction of each T_f and T_s component within a fire was allowed to vary randomly between 0.0001 and 0.01 (or between 100 m^2 and 10,000 m^2 in a MODIS 1km MIR pixel) and was based on realistic estimates of the minimal detectable area [*Giglio et al.,* 2003]. The T_b fraction was computed as 1 minus the

sum of the T_f and T_s components. The radiance for each component was calculated using the Planck function (equation (2.22)) and summed to produce a total fire radiance which represents the surface radiation to be adjusted for atmospheric effects.

The atmospheric correction parameters, $L_{atm\uparrow}$, $L_{atm\downarrow}$, and t, were generated from the parametric model using MOD07 profiles (see section 2.6) which were chosen to cover a range of land covers (Table 2.7) and based on active fires being present in the Quicklook images (e.g. Figure 2.13).

Table 2.7: Regions, date-time, and the number of profiles used from MOD07 to generate realistic atmospheric conditions to derive radiative transfer parameters.

Region	Time Stamp	# profiles
NHAF	2008001.1240	113
NHAF	2008116.1155	125
SHAF	2008229.1210	117
SHAF	2008229.1215	94
AUST	2008198.0440	233
AUST	2008214.0440	252
BOAS	2008167.0405	84
BOAS	2008182.0500	190
BONA	2008212.2005	143
BONA	2008221.1955	140
CEAS	2008198.0455	113
CEAS	2008222.1045	105
SHSA	2008229.1710	246
SHSA	2008245.1710	201

Over 2000 unique combinations of simulated fire radiances and atmospheric correction parameters generated from the MOD07 profiles were used in equation (2.23) to simulate TOA fire radiances. The water vapor content ranged from 0.88 to

5.6 g cm^{-2}. Emissivity was assumed to be unity. Finally, the MODIS FRP algorithm (equation (2.25)) was used to convert surface and TOA fire brightness temperature to FRP.

$$FRP\ [MW\ km^{-2}] = 4.34 \times 10^{-19} (T^8_{MIR} - T^8_{bg,\ MIR}) \qquad (2.25)$$

Where T^8_{MIR} is the fire pixel brightness temperature and $T^8_{bg,\ MIR}$ the background temperature; raised to the 8th power. More details about the MODIS FRP algorithm can be found in Chapter 3 as well as *Kaufman et al.* [1998].

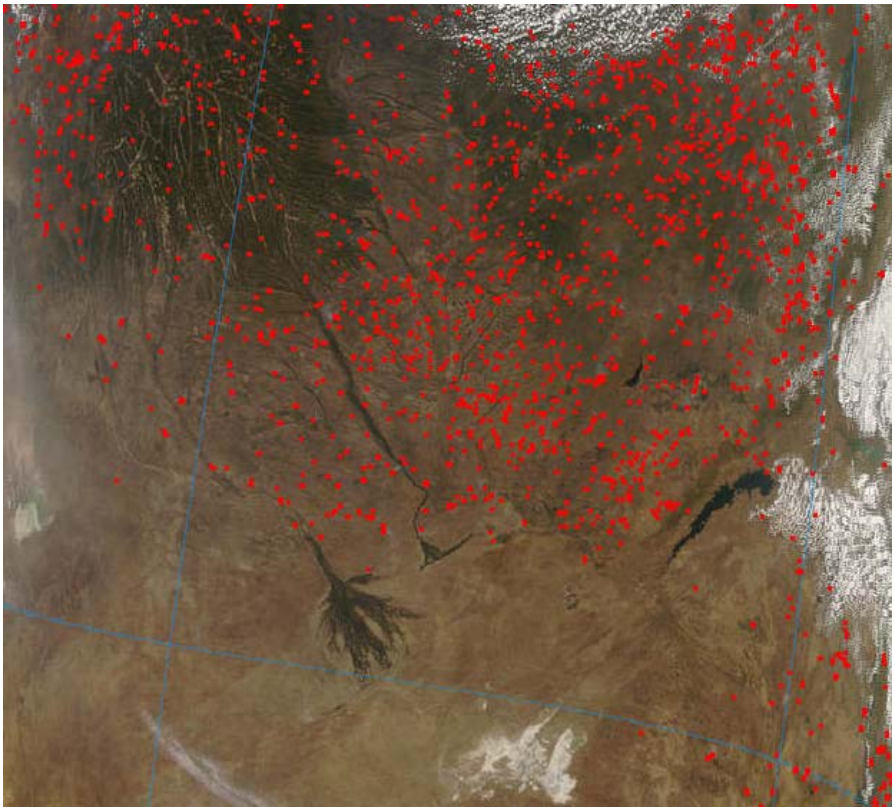

Figure 2.13: Example Quicklook from MODIS Aqua for central Africa on August 16th, 2008 at 1210 (UTC). 117 MOD07 profiles were processed in the parametric model for this granule.

The result from the comparison of the surface and TOA FRP across all regions and profiles suggests a 20% loss of instantaneous energy (Figure 2.14). View angle has a non-linear, inverse relationship with the bias between surface and TOA FRP, which for the purposes of this relationship was driven only by atmospheric conditions as point-spread function, fire location within a pixel, and scan-pixel size effects were not considered. The underlying cause of the bias associated with view angle was then examined.

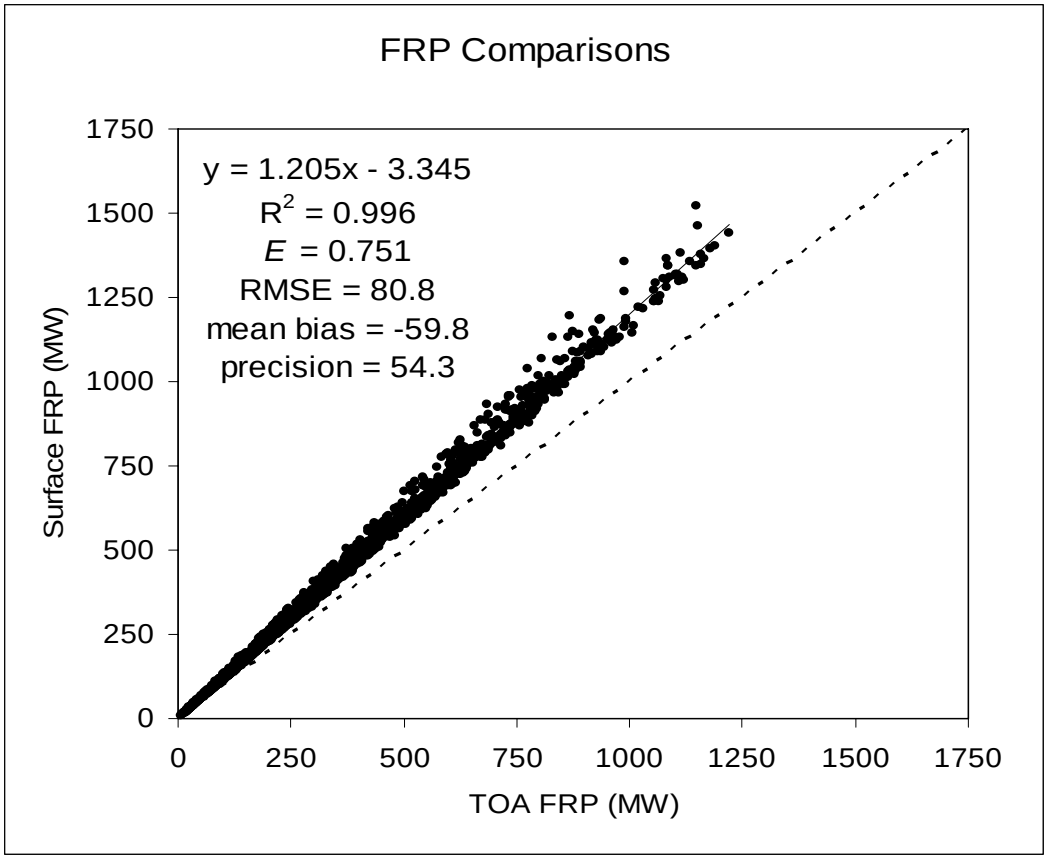

Figure 2.14: Comparison of simulated surface and TOA FRP. Radiances were simulated from randomly generated fire pixel temperature and fractional area components (fire, smoldering, and background). MODIS Aqua profiles were used to provide realistic atmospheric parameters used in the radiative transfer modeling. The 1:1 (dashed) line is plotted for reference.

Although water vapor is a strong absorber of thermal radiation, it did not show any influence on the bias in this case study. This is likely due to (1) optimal placement of the MODIS 4μm channel to minimize water vapor absorption, and (2) fires generally occur during dry periods when relative humidity is low (i.e. lower water vapor content in the atmosphere) relative to other times of the year.

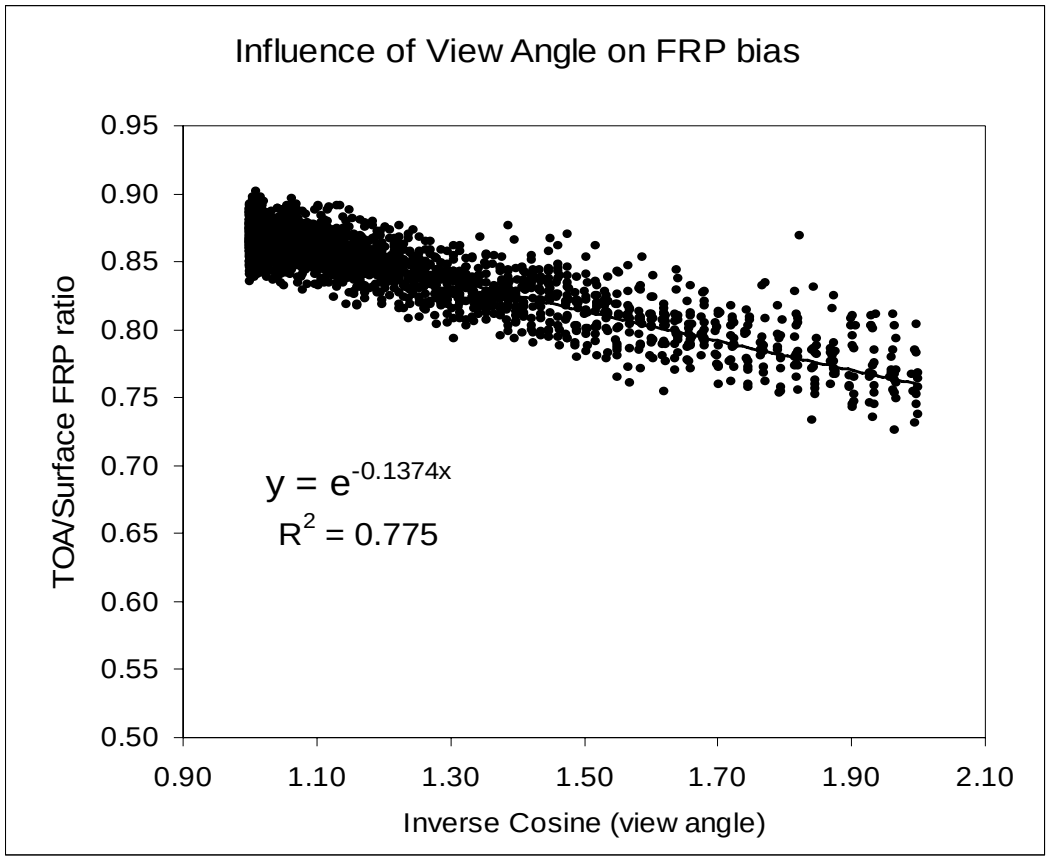

Figure 2.15: Influence of the inverse cosine of the view angle on the bias between TOA and surface FRP.

Beyond further comprehensive analysis of the atmospheric constituents, it was concluded that fire radiance is primarily being attenuated in the atmosphere by homogeneous gas species such as N_2 and CO_2. Therefore, provided the view angle is

known, a simple, but effective correction is offered, in which the bias between surface and TOA FRP can be estimated from an exponential function and applied to the TOA FRP to adjust for atmospheric effects. The function is physically based on the cosine effect of the view angle. Figure 2.15 provides a plot of the relationship between the bias and inverse cosine of the view angle, along with the corresponding exponential fit. The exponential function, rather than a linear fit, is appropriate given the nature of error with increasing view angle (*cosine effect*). Figure 2.16 provides a plot of the "corrected" TOA FRP using the exponential correction factor.

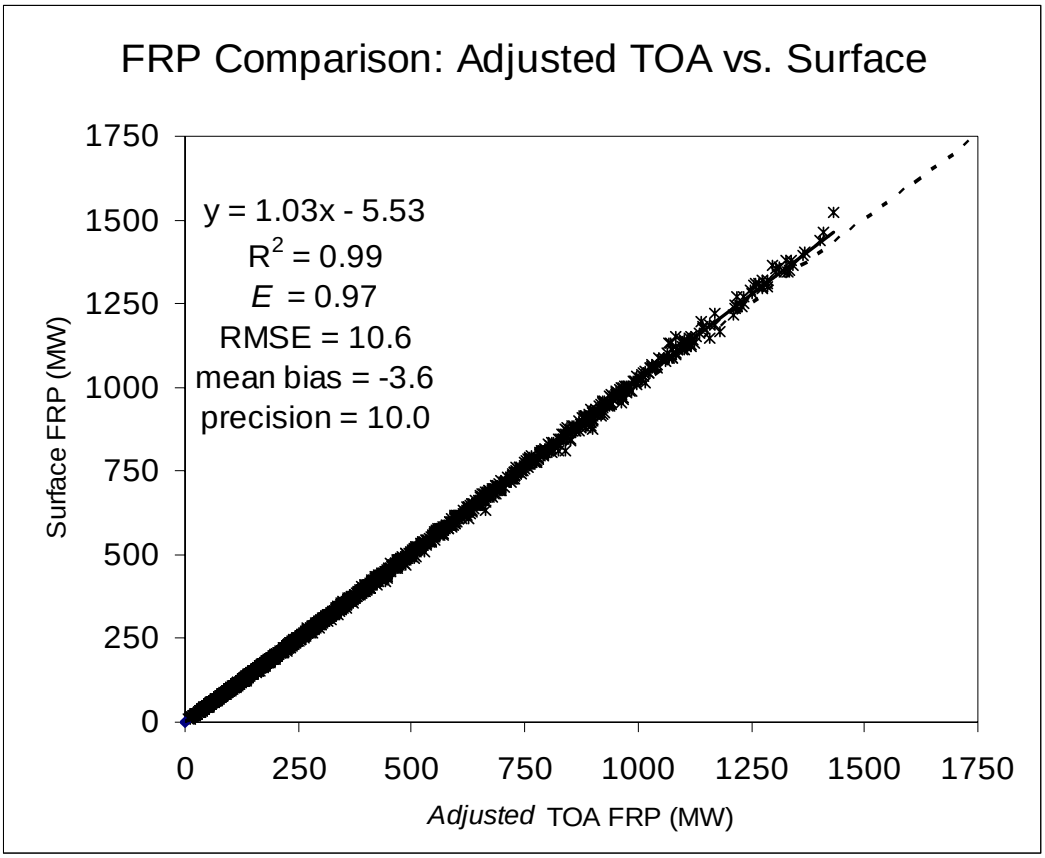

Figure 2.16: Simulated TOA FRP "corrected" for atmospheric effects compared with simulated surface FRP. The 1:1 (dashed) line is plotted for reference.

2.9 Atmospheric Profiles

An important aspect of the atmospheric correction in the longwave infrared is the accuracy of the atmospheric profile used in the correction model. As part of the evaluation process an additional analysis was included to test several sources of atmospheric data with the idea that an operational atmospheric correction scheme for MODIS could be developed using the parametric model and an accurate profile retrieved via coincident satellite sounding. Three sources of atmospheric profile data were compared; the Integrated Global Radiosonde Archive (IGRA), positioned as the reference data since *in situ* measurements are made along the path of ascent in the atmosphere; MODIS profile retrieval product (MYD07), discussed earlier; and the Atmospheric InfraRed Sounder (AIRS)[3].

The IGRA[4] database [*Durre et al.,* 2006] consists of 1500 globally distributed sounding stations with data records spanning over 30 years. Generally, each station makes two daily launches at 1100 and 2300 UTC. Profile observations are provided at standard, surface, tropopause, and significant levels. Standard level variables include pressure, temperature, geopotential height, dew point temperature, wind direction, and wind speed. The standard level product generally had a vertical resolution of 20 layers. The vertical resolution of the standard level product was expanded by including variables from the significant thermodynamic layer product, therefore creating a profile that included approximately 40 vertical layers. The radiosonde profiles were assumed to be the benchmark by which to compare other profiles. Since NCEP profiles are assimilated products incorporating radiosonde data,

[3] http://eospso.gsfc.nasa.gov/eos_homepage/for_scientists/atbd/docs/AIRS/AIRS_L1B_ATBD_Part_1.pdf
[4] http://www.ncdc.noaa.gov/oa/cab/igra/index.php

the above analysis was not replicated with this data. Rather, the intention is to view the radiosonde data as a potential source of data to act as a "truthing" product to validate the satellite derived profiles, much in the way that the Aerosol Robotic Network (AERONET)[5] system is used for aerosol retrievals. However, many radiosonde launch stations recorded sporadic or incomplete profile information which may limit the functionality as a global validation dataset. In some cases the data were completely missing for a given satellite overpass or the vertical content was too small to be useful (e.g. <10 layers).

AIRS is a high spectral resolution spectrometer with 2378 channels in the thermal infrared, ranging from 3.7μm to 15.4μm. The standard product provides global, twice daily coverage at 50 km horizontal and 28 layer vertical resolutions for any given location; the vertical resolution was interpolated to 40 layers to match the radiosonde profiles for consistency. Among the variables recorded, the most relevant includes geopotential surface and layer height, water vapor mixing ratio, water vapor saturation mixing ratio, surface and layer temperature, standard pressure levels, columnar water vapor, and quality flags. Since the AIRS sensor is aboard Aqua it provides temporally coincident observations with MODIS, but at higher spectral resolution and greater profile sounding vertical resolution. However, the spatial resolution of AIRS (50 km) is nearly 50 times coarser than MODIS radiance retrievals (1 km), and 10 times coarser than the MYD07 product (5 km).

It should be stated that near coincident observations were assumed from AIRS and MODIS. Although it is unrealistic to think that the timing, and therefore the

[5] http://aeronet.gsfc.nasa.gov/F_Info/system_info_additional.html

profiles retrieved from the three sources will be identical, this analysis offered an opportunity to investigate several sources of profile data to see how closely the temperatures, produced using at-sensor radiances, corresponded.

MODIS L1B radiance retrievals were once again used as the TOA observation data to be adjusted for atmospheric perturbations. Incorporating the radiosonde profiles into MODTRAN returned the necessary correction parameters which were then used to calculate synthetic "reference" surface brightness temperatures to compare with the parametric model. For comparison the two satellite-derived atmospheric profile products available aboard the Aqua satellite (AIRS and MODIS) were used with the parametric model to correct TOA radiances and calculate surface temperatures. Coincident observations between Aqua and radiosonde soundings were limited to the launch times of at IGRA stations. Also, stations were chosen that offered coastal launches and prevailing winds that would provide open water observations, reducing emissivity uncertainty, and allowing for comparison with AIRS and MODIS. Several locations in the Mediterranean Sea were chosen for their ideal physical location and coincidence of Aqua satellite overpass with radiosonde launch.

Figure 2.17 demonstrates the agreement between the "reference" temperatures and the AIRS-parametric model derived temperatures for MODIS bands 31 (E = 0.88, bias = -0.02°C) and 32 (E = 0.84, bias = -0.04°C). The RMSE for both bands indicates the error in the match between the temperature derivations is less than 1 K. The precision indicates, however, that on a point-by-point basis the temperatures deviate by an average of 0.5 K and 0.8 K for band 31 and 32, respectively. A limited

number of observations (n = 15) and an average difference of 0.44 g cm^{-2} in the water vapor content recorded by the radiosonde and AIRS may be the cause.

The corresponding comparison between the radiosonde-MODTRAN reference temperatures and the MYD07-parametric model temperatures showed less agreement for bands 31 (E = 0.50) and 32 (E = 0.13) than the AIRS-parametric model temperature comparisons above. Residual error and bias were greater as well (band 31 RMSE = 1.50 K, bias = 1.26 K; band 32 RMSE = 2.61 K, bias = 2.21 K) (Figure 2.18). The precision showed that the spread of data does not agree well either. The larger bias generated when using the MODIS profile data may be in part due to lower spectral resolution as compared with AIRS. In addition, the mean difference in water vapor content between MODIS and the radiosonde retrievals was 2.7 g cm^{-2}; significantly greater than between AIRS and radiosonde retrievals. Indeed, validation of MOD07 product for the most recent reprocessing ("Collection 5") demonstrated greater bias by the MODIS product clearly interpolation (spatial and temporal) of radiosonde measurements is necessary for atmospheric data to be used on a global, operational scale. Frequent and regular validation of the MODIS and AIRS profiles against radiosonde measurements would insure product accuracy and offer a quantitative measure of uncertainty in the products. Another consideration is the vertical resolution of soundings which influences the accuracy of RTM estimates. The advantage AIRS offers over MODIS is greater vertical detail of the atmosphere, but this is offset by the lower horizontal resolution. Something of a combination

a.

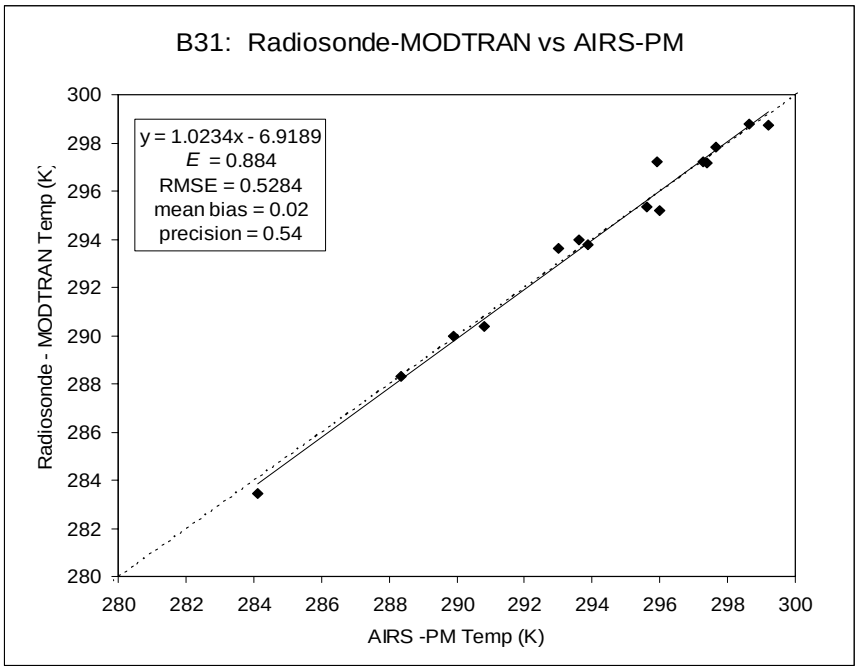

b.

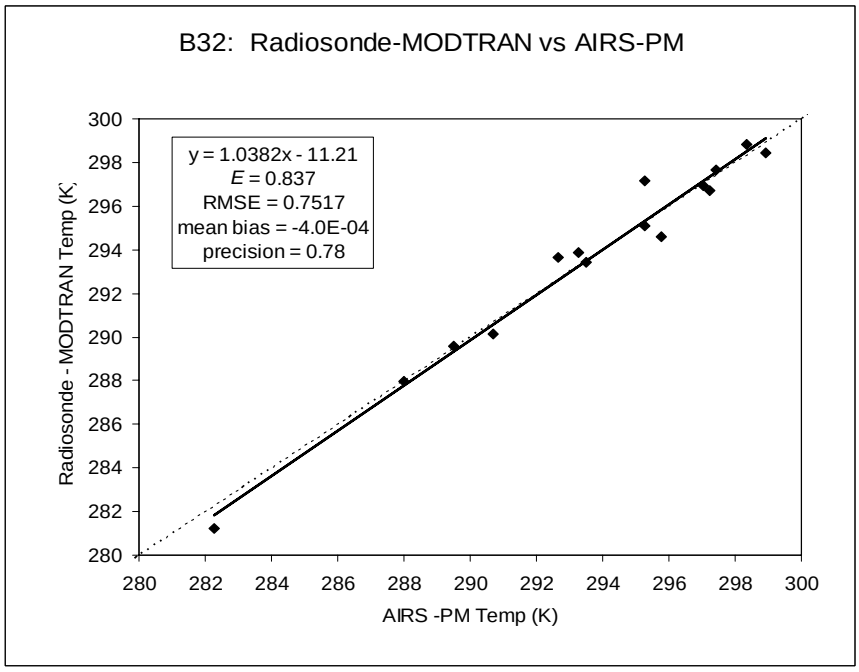

Figure 2.17: Comparison of calculated sea surface temperatures. Radiosonde profiles used in MODTRAN offer "reference" temperatures to compare the AIRS profile – parametric model derived temperature estimates. MODIS band 31 (a) and 32 (b). The 1:1 line (dashed) is shown for reference.

a.

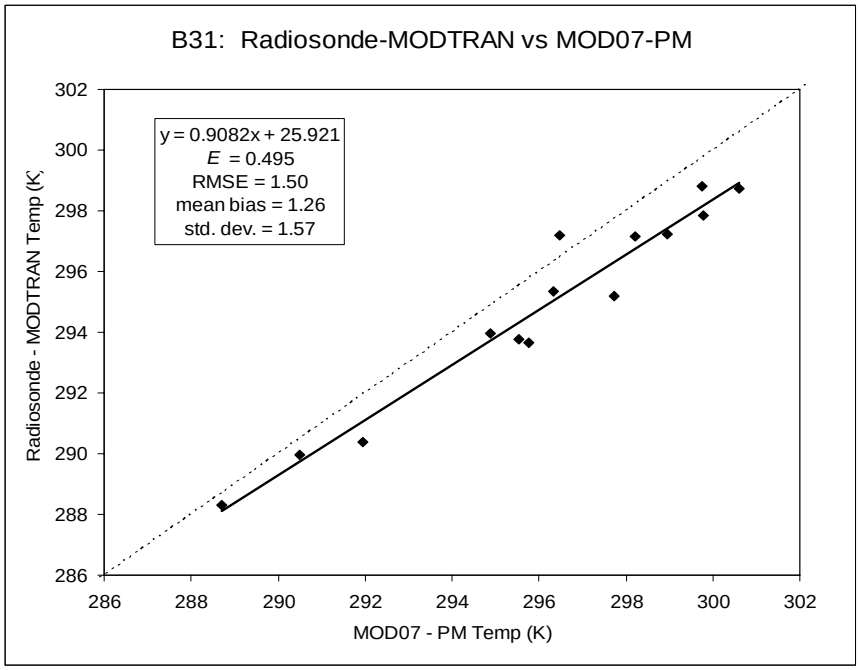

b.

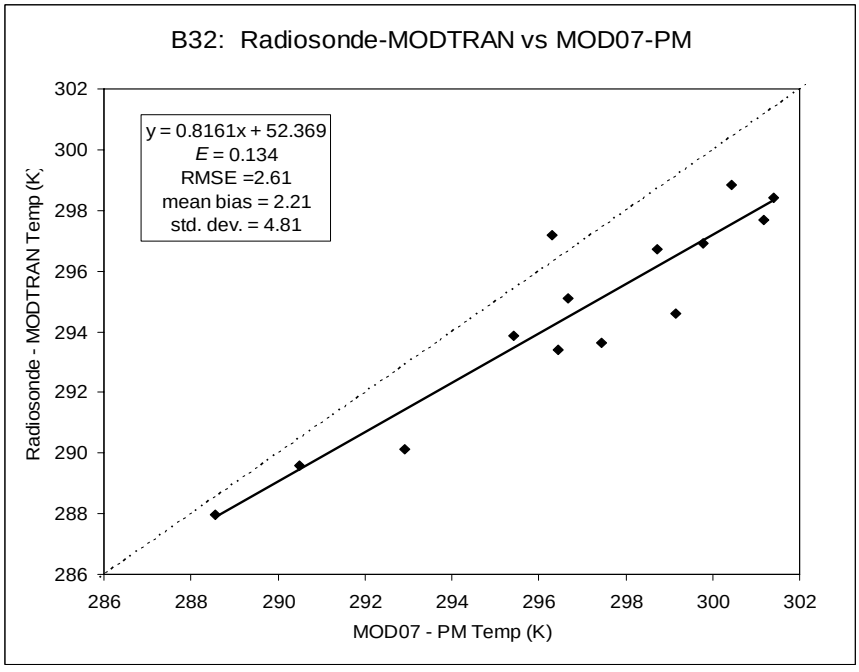

Figure 2.18: MODIS band 31(a) and band 32 (b) comparison between the radiosonde-MODTRAN "reference" surface temperatures and MOD07- parametric model derived temperatures. The 1:1 line (dashed) is shown for reference.

between the MODIS horizontal and AIRS vertical resolutions would offer greater detail about the true atmospheric conditions.

2.10 Conclusions

The parametric model offers an approach to operationally correct the at-sensor radiance values for atmospheric perturbations. Evaluation of the parametric model against MODTRAN showed consistent results for retrieval of correction parameters. Computation speeds to generate the correction parameters were over 3 orders of magnitude faster than MODTRAN. This is a significant increase when considering the enormity of performing such computations on a global, operational basis. Comparison of surface temperatures calculated using the parametric model against the MODIS SST (MYD28) product showed a good agreement (RMSE = 0.49 K) with individual point retrievals within -0.45 K ± 0.19 K of the MODIS estimates. It should be reiterated that the MYD28 product cannot be used as a surrogate for *in situ* measurements. Rather the comparison was intended to assess if the parametric model was consistent with estimates from a standard MODIS product.

Evaluation of MODIS surface temperature retrievals, corrected for atmospheric effects with the parametric model, versus *in situ* temperature retrievals demonstrated the model's ability to accurately retrieve correction parameters. For band 31, and both surface types (LST and SST), the bias was -0.22 K with an RMSE of 0.53 K. While the bias for band 32 was -0.42 K with an RMSE of 0.84 K. This is well within the reported LST accuracy of 1 K reported by [*Wan et al.,* 2002]. The precision for both bands was roughly a factor of 2 greater (0.49 K and 0.76 K, band 31 and 32,

respectively) indicating variability between retrievals, perhaps due to some heterogeneity in the surface conditions.

Applying the parametric model to evaluation of MODIS estimates of FRP reveals an approximately 20% underestimation in TOA FRP. Ideal placement of the MIR channel on MODIS limits the impact of water vapor attenuation on the observed fire radiation, but gaseous absorption by N_2 and CO_2 indeed play a role in reducing the energy sensed. Since gaseous species are rather homogeneous in the atmosphere the attenuated signal can best be characterized by the satellite view angle. A simple, yet effective correction factor showed that FRP could be adjusted by the inverse of the view angle cosine.

Consideration of the profiles used in radiative transfer modeling is paramount to achieving accurate correction for atmospheric effects. This study touched on a few sources of satellite profile data and demonstrated their relative accuracy when compared with radiosonde atmospheric retrievals. However, nonuniformity of atmospheric water vapor between profile sources suggests that obtaining a profile that accurately reflects the true atmospheric state may be difficult.

Chapter 3: Estimating Biomass Consumed from Fire Using MODIS FRE[6]

3.1 Introduction

Wildland fire is a global phenomenon which plays a pivotal role in affecting the dynamics of vegetation, hydrology, and atmospheric composition [*Innes*, 2000]. Recently, *Running* [2008] pointed to the impacts of fire disturbance in altering ecosystem carbon cycles; often shifting large carbon reservoirs to carbon sources. Projected increases in burned area with climate change, such as reported by *Flannigan et al.* [2005], underscore the importance of understanding fire in current and future climate conditions.

Quantifying the biomass consumed by fires is a key component to elucidate these dynamics. The biomass consumed (kg) is typically calculated as the product of burned area (km^2), fuel load (kg km^{-2}), and combustion completeness (fraction of available fuel burned) [*Seiler and Crutzen*, 1980]. However, accuracy of these components remains an issue that leads to an uncertainty in estimates of biomass consumed and related emissions of at least 50% [*Robinson,* 1989*; Korontzi et al.,* 2004; *van der Werf et al.,* 2006]. Despite improved datasets, uncertainty in current estimates suggests the need to explore alternative and complementary approaches. Vegetation fires can be thought of as the obverse of photosynthesis in which energy stored in biomass is released as heat (equation (3.1)).

---

[6] The following chapter is an expanded version of *Ellicott et al.,* [2009b]

$$(C_6H_{10}O_5)_n + O + \textit{ignition temperature} \longrightarrow CO_2 + H_2O + \textit{heat} \qquad (3.1)$$

The cascade of chain of reactions starts with the pre-heating of fuels ahead of the fire front and partial pyrolytic decomposition. Ignition signifies the transfer from pre-heating to combustion in which exothermic reactions start and the next phase, encompassing a combination of flaming and smoldering combustion, begins. Flaming combustion occurs when flammable hydrocarbon gases released during pyrolysis are ignited with wildfire flaming combustion temperatures in the range of 800 – 1400 K [*Lobert and Warnatz,* 1993]. Pyrolytic action involves the thermal decomposition of fuel resulting in the release of water, CO_2, and other combustible gases (e.g. CH_4) and particulate matter. The heat produced, often measured as heat yield (MJ/kg), is thermal energy transferred via conduction, convection, vaporization, and radiation and provides a metric of the total potential energy released if complete combustion of the fuel occurs. Although other factors, including slope, fuel arrangement, and wind speed influence the actual heat yield in a fire event, the theoretical value varies very little between fuel types [*Whelan,* 1995; *Stott,* 2000]. The radiant component is emitted as electromagnetic waves traveling at the speed of light in all directions and is proportional to the absolute temperature of the fire (assumed to be a black body) raised to the fourth power. It is the radiative component that is estimated from Earth observing satellite sensors, offering a method to quantify the biomass consumed, and assuming an emission factor (gas or aerosol mass emitted

per mass of fuel consumed, [*Andreae and Merlet,* 2001]) is known, the atmospheric emission load.

The foundation for using measurements of fire radiative energy (FRE) is based on the fact that the rate of biomass consumed is proportional to the rate of FRE. Integrating the rates over time and space yields the totals for biomass consumed and FRE. Based on simulated fires, *Kaufman et al.* [1998] revealed that an empirical relationship exists between instantaneous FRE (fire radiative power, or FRP) and pixel brightness temperature measured in the Moderate Resolution Imaging Spectroradiometer (MODIS) middle infrared channel (4 μm) and is the current MODIS FRP algorithm (equation (3.2)):

$$\text{FRP [MW km}^{-2}\text{]} = 4.34 \times 10^{-19} \left(T^{8}_{\text{MIR}} - T^{8}_{\text{bg, MIR}}\right) \qquad (3.2)$$

where FRP is the rate of radiative energy emitted per pixel (the MODIS 4μm channel has IFOV of 1km), 4.34×10^{-19} [MW km^{-2} Kelvin^{-8}] is the constant derived from the simulations, T_{MIR} [Kelvin] is the radiative brightness temperature of the fire component, $T_{\text{bg, MIR}}$ [Kelvin] is the neighboring nonfire background component, and MIR refers to middle infrared wavelength, typically 4μm.

Field experiments by *Wooster et al.* [2005] demonstrated the use of instantaneous and total FRE measurements to estimate biomass consumed from fire. A recent laboratory investigation of FRE and biomass fuel consumption by *Freeborne et al.* [2008] supported the accuracy of *Wooster et al.'s* [2005] findings and lends credence to the application of satellite based measurements of FRE. *Roberts and Wooster*

[2008] showcased the application of high temporal satellite based FRP measurements from the SEVIRI geostationary sensor to calculate FRE. However, to date no study has derived FRE at a global scale, in part due to limitations in temporal or spatial resolution of satellite sensors.

This chapter presents an approach to estimate MODIS FRP beyond the nominal retrievals. FRP was estimated at 0.5˚ spatial and monthly temporal resolution for 2001 – 2007 using the MODIS climate modeling grid (CMG) standard product [*Giglio*, 2005]. FRP estimates are integrated to calculate FRE and then applied to FRE-based biomass consumption coefficients to calculate the total biomass burned from fire in Africa. Finally, a comparison of biomass burned estimates with previously published estimates is presented and followed by concluding remarks.

3.2 Materials and Methods

3.2.1 MODIS FRP

The MODIS sensors, onboard the sun-synchronous polar-orbiting satellites Terra and Aqua, acquire four observations of nearly the entire Earth daily at 1030 and 2230 (Terra) and 0130 and 1330 (Aqua), equatorial local time. The first MODIS sensor was launched aboard the Terra satellite in 1999; the second was launched in 2002 aboard Aqua. In this research, fire radiative energy (FRE) was estimated at 0.5˚ spatial and monthly temporal resolution for 2001 – 2007 using the MODIS climate modeling grid (CMG) standard product [*Giglio*, 2005]. The CMG product provides monthly mean fire radiative power (FRP), as well as products describing cloud fraction and corrected pixel counts, at 0.5˚ spatial resolution [*Giglio*, 2005; *Giglio et*

al., 2006]. Monthly mean FRP was multiplied by the cloud-and-overpass-corrected fire pixel count, producing the total FRP released within a given grid cell for each time period. Five years of monthly CMG data (2003 to 2007) from both Terra and Aqua was also used to offer a long term (rather than a single year) characterization of the temporal variability between the two satellite observations. This variability is used later to parameterize the fire radiative power diurnal cycle.

In addition, the MODIS Level 2 fire product (MOD14) was included from Terra and Aqua. This fire product is collected daily at 1km resolution and includes, among other information, the latitude, longitude, FRP, and confidence of the fire detection. Since neither SEVIRI nor VIRS provide high latitude fire observations (i.e. boreal fires) the fire radiative power diurnal cycle characterization for these cases were supplemented by MODIS observations and is described later in section 3.3.1.

3.2.2 SEVIRI FRP

The Spinning Enhanced Visible and Infrared Imager (SEVIRI) was launched aboard the European Organization for the Exploitation of Meteorological Satellites (EUMETSAT) Meteosat-8 satellite on August 28th, 2002. SEVIRI's nominal position at 0° longitude centers it on Europe and Africa while providing a geographic viewing range between approximately 75°E - 75°W and 75°N - 75°S in the longitudinal and latitudinal directions, respectively. The SEVIRI sensor provides 15-minute temporal resolution across 11 spectral channels (0.6μm – 14μm) with a horizontal spatial resolution of 3km at the sub-satellite point and an instantaneous field of view (IFOV) of 4.8km. Of particular interest is the 3.9μm "fire" channel, which has a low noise-

equivalent temperature difference (NEdT) of less than 0.35k at 300k [*Roberts et al.*, 2005]. SEVIRI FRP observations were used from February and July, 2004. These two months capture the distinct period of fire activity in Africa which follows a latitudinal gradient, starting in the North and progressing South through the year, eventually shifting North again by December. A large number of observations were available for February and July (~1.3 x 10^6 and 2.1 x 10^6 fire pixels, respectively) providing an adequate sample to characterize the fire radiative energy diurnal cycle.

3.2.3 TRMM VIRS

The Visible and Infrared Scanner (VIRS) aboard the Tropical Rainfall Measuring Mission (TRMM) was launched in 1997 and though intended to monitor rainfall variability it has proven successful at fire detection and monitoring, owing to channel placements at 3.75μm and 10.8μm [*Ji and Stocker*, 2002; *Giglio*, 2007]. TRMM has an inclined (35°), precessing orbit so that VIRS observes the Earth between 38°N and 38°S. The precessing orbit also means that local overpass time changes to cover each hour of a day once per month. This drift in overpass time allowed *Giglio* [2007] to characterize the diurnal cycle of fire observations for a "typical" 24 hour period after corrections for overpass and cloud obscuration biases. Probability density functions (PDF) were used for 7 of the 15 diurnal cycles reported by *Giglio* [2007]. Although this data does not directly provide a quantity of FRP, the probability of fire detection for a given hour corresponds well with FRP as demonstrated by *Giglio* [2007]. Therefore it can be assumed that the shape of the TRMM PDF curves corresponds with the shape of the FRP diurnal curve.

3.3 Fire Radiative Energy

3.3.1 Fire Energy Diurnal Cycle

An important characteristic of the radiative energy emitted from fires is the diurnal cycle. *Giglio* [2007] characterized the hourly cycle of fire activity in the tropics and sub-tropics using the VIRS and showed that for most tropical and subtropical fires the temporal trajectory (or curve) follows a rather distinct pattern of increasing hourly fire activity into the early afternoon, followed by a rapid drop in activity (and associated fire radiative energy) through the evening. Describing the discrete observations as a continuous function simplifies quantifying the integral of the area beneath the curve which represents the total fire energy detected. *Roberts and Wooster's* [2008] application of geostationary observations from SEVIRI showcased the capability of high temporal FRP measurements for the calculation of time integrated fire energy.

In this research, an approach to estimate MODIS monthly totals of FRP for each hour outside the nominal retrieval times (again, 10 am/pm UTC for Terra; 1 am/pm UTC for Auqa) is developed. Integrating the hourly FRP totals for each month generates monthly FRE estimates to investigate biomass burning consumption, as well as aerosol emissions (Chapter 4). To characterize regionally representative fire energy temporal trajectories a combination of observations from SEVIRI, VIRS, and MODIS was used. Examination of the temporal trajectories was performed in 16 globally distributed regions. These were chosen to be large enough to be statistically robust, yet small enough to allow for spatial variability between regions (Table 3.1 and Figure 3.1). VIRS data, provided by *Giglio* [2007], offered regions in the tropics

Table 3.1: Climate modeling grid (CMG) regions used for examining the Terra/Aqua ratio and diurnal cycle of fire. Coordinates (X, Y) are for the upper left cell in each region.

x (CMG)	Y (CMG)	size (degree)	region name
406	160	7.5° x 7.5°	SEVIRI - eastern sahel
406	156	12.5° x 6°	SEVIRI - eastern sahel
380	160	10° x 10°	SEVIRI - central
361	161	10° x 10°	SEVIRI - central coast
399	200	7.5° x 7.5°	SEVIRI - south central
420	187	7.5° x 7.5°	SEVIRI - south east
399	185	7.5° x 7.5°	SEVIRI - central
400	156	18° x 8°	VIRS - eastern sahel
390	192	6° x 9°	VIRS - west central Africa
240	196	6° x 5°	VIRS - Brazil deforest
422	192	8° x 12°	VIRS - east central Africa
620	202	6° x 4°	VIRS - northern Australia
408	230	8° x 8°	VIRS - South Africa
510	136	10° x 8°	VIRS - India
480	43	20° x 6°	MODIS - north central Russia
65	42	15° x 7.5°	MODIS - Alaska-Canada border

and sub-tropics to supplement, and compare in the case of Africa, SEVIRI data. Two additional sites were included using MODIS daily FRP (MOD14) retrievals from high latitude boreal sites in Russia and North America. These retrievals were included to aid in characterizing the fire cycle beyond the geographic coverage offered by SEVIRI and TRMM (i.e. tropics and subtropics) and therefore provide insight into different fire energy emission cycles. As mentioned previously in section 3.2.1, MODIS is on polar-orbiting satellites and subsequently provides more frequent retrievals at higher latitudes. Although this bias is accounted for in the gridded CMG product [*Giglio et al.* 2006], the daily observation bias aids the analysis of the diurnal

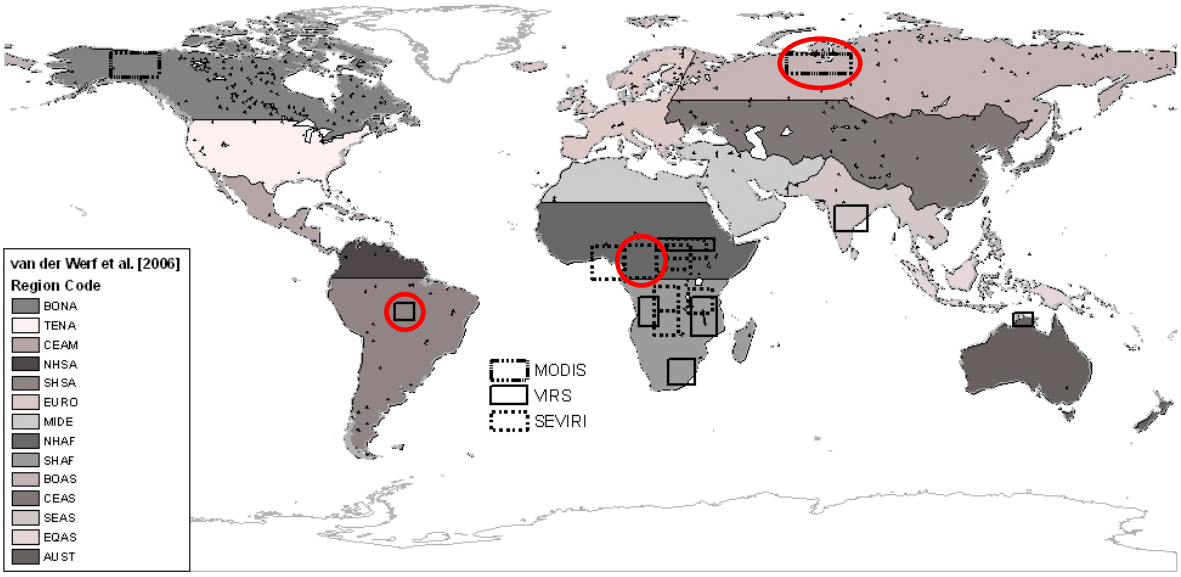

Figure 3.1: Global extent of regions used to analyze the diurnal cycle from SEVIRI, TRMM, and MODIS observations. The red circles highlight regions used as examples in Figure 3.2. The base map is the regional categorization from the Global Fire Emissions Database (GFEDv2) [*van der Werf et al.,* 2006].

cycle by providing additional retrievals beyond the nominal overpass times. On average, each satellite provided 4 to 6 overpasses per day at high latitudes. FRP observations were binned in hourly increments and normalized by the number of days in the month contributing to a binned hour. Several examples of the diurnal cycle are illustrated in Figure 3.2.

Using the data described a modified Gaussian function (equation (3.3)) was shown to provide a simple and accurate representation of the observed diurnal cycle:

$$FRP(t) = FRP_{peak}(b + e^{-\frac{(t-h)^2}{2\sigma^2}}) \quad (3.3)$$

Where t is time (hour) for which the discrete FRP is estimated and FRP_{peak} is the peak of the curve. The hour (h) of peak FRP generally occurs in the early afternoon, but this variable has little effect on the final FRE derivation. More importantly is σ which is the sigma (standard deviation) of the curve and provides details about the duration of fire activity. Equation (3.3) also includes a background FRP, b, which is a constant independent of time. The dependence of parameters of the diurnal cycle, h, σ, and b, were examined as a function of Terra-to-Aqua FRP (T/A) ratios. The T/A ratio is based on monthly CMG FRP values for 2003 - 2007 (n = 60) and represents the average ratio between Terra and Aqua FRP retrievals within a given region (Figure 3.2). As stated in section 3.2.1, the CMG FRP product is the summation of daily MODIS retrievals constituting daytime and nighttime fire detections. Figure 3.3 shows Terra and Aqua monthly mean FRP plotted over 60 months of data for several regions.

The contention is that given the simple Gaussian form adopted for the diurnal cycle, the variation in the T/A ratio can serve as a proxy for the fire energy diurnal cycle. Aqua's afternoon (1330 local time) overpass should correspond (generally) with the hour of peak fire energy. This is a function of local fire weather conditions as humidity decreases and fuels dry with an increase in ambient temperature and pre-heating by neighboring combusting fuels [*Whelan,* 1995]. Terra's morning overpass will likely correspond with less fire activity as compared with Aqua. In this research, it was theorized that the ratio between Terra and Aqua FRP should relate to

the variables in the Gaussian function, specifically the duration of peak activity (σ parameter) and the constant (background) fire energy (b). In addition, the Gaussian model appears adaptive to local diurnal cycles of fire radiative energy, as illustrated in Figure 3.2. A large difference between Terra and Aqua (e.g. 0.20 T/A ratio) would indicate a rapid increase in fire radiative energy and shorter duration of fire activity. Anthropogenic fires such as for pasture maintenance, agricultural clearing, or slash burning, offer a good example as they are typically set during early to mid-day and burn out by evening. A T/A ratio approaching 1.0 would represent a flatter, smoother fire radiative energy cycle where the fire is more active around the clock. Forest fires, particularly fires that are unmanaged, may burn with a relatively (to anthropogenic fires) consistent fire radiative energy throughout the diurnal cycle with a dip in energy in the cooler, often humid, early morning hours [*Whelan,* 1995]. This is evident in the CMG product when the Terra summation of FRP (1030 and 2230) is nearly the same, or even greater, than the Aqua summation (1330 and 0130). Boreal fires, which tend to burn for days to weeks with relatively consistent fire energy emissions, offer a good example of this scenario. In fact, ratios greater than 1.0 are possible, as seen in Figure 3.4b. In this case, because of changes in local weather conditions fires tend to subside in activity in the early morning hours as would be observed by Aqua at 0130. The result is that the sum of day and night FRP from Terra is greater than the sum of day and night FRP from Aqua.

Figures 3.4a, b, and c, respectively, show the variation of the diurnal cycle parameters h, σ and b as a function of the T/A ratio derived from the 2003 - 2007 period. The σ parameter shows a good correlation with the T/A ratio, highlighting

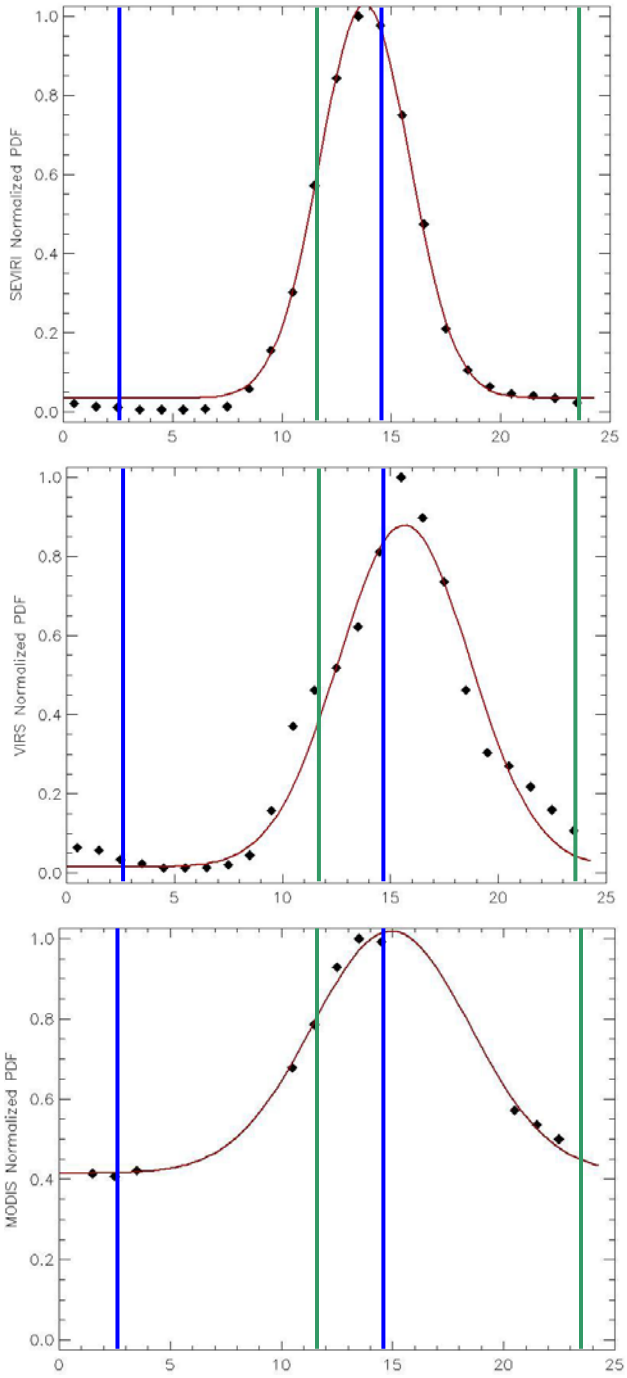

Figure 3.2: Fire radiative power diurnal cycles. The red curve (solid line) shows the fit of the diurnal cycle using a modified Gaussian function (Eq. (5)). Regions are highlighted with red circles in Figure 3.1 and correspond with (a) SEVIRI northern Africa region, (b) TRMM VIRS "Brazil deforestation" region; and (c) MODIS boreal Russia. Shown for reference are MODIS overpass times: Green vertical lines for MODIS-Terra and blue vertical lines for MODIS-Aqua.

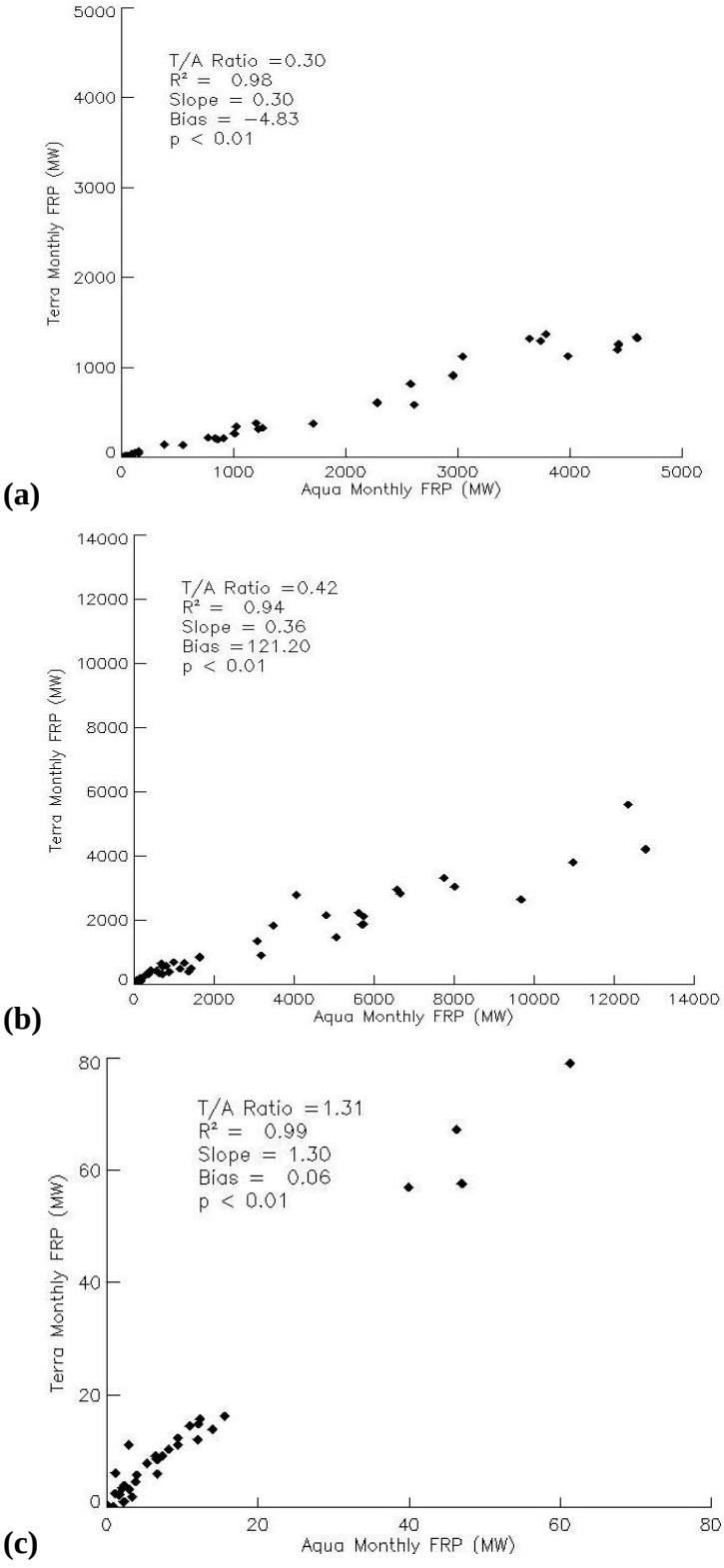

Figure 3.3: Ratio between monthly Terra and Aqua (T/A) CMG FRP from 2003-2007 (n = 60) for 3 study regions (see Figure 3.1) used to develop relationship with the temporal curve of fire observations within the corresponding region; (a) central Africa region used with SEVIRI diurnal curve characterization (Figure 3.2a); (b) TRMM Brazil "deforestation" region (Figure 3.2b); and (c) corresponds with MODIS boreal diurnal curve regions (Figure 3.2c).

that with low T/A values the width of the curve decreases (i.e. steeper curve), likely associated with rapid burning fire events. On the other hand, as the T/A ratio approaches 1.0 there is a correspondingly wider curve and thus greater σ value. The peak hour (h) of the diurnal cycle is not correlated with the T/A ratio, but values tend to fall around the expected range of early afternoon. A sensitivity test of the h parameter indicated that its influence on calculating FRE was minimal. For example, applying a range of plausible T/A ratios, between 0.1 and 1.2 (at 0.1 interval steps), to the h fit results in only a half-hour change in the peak hour.

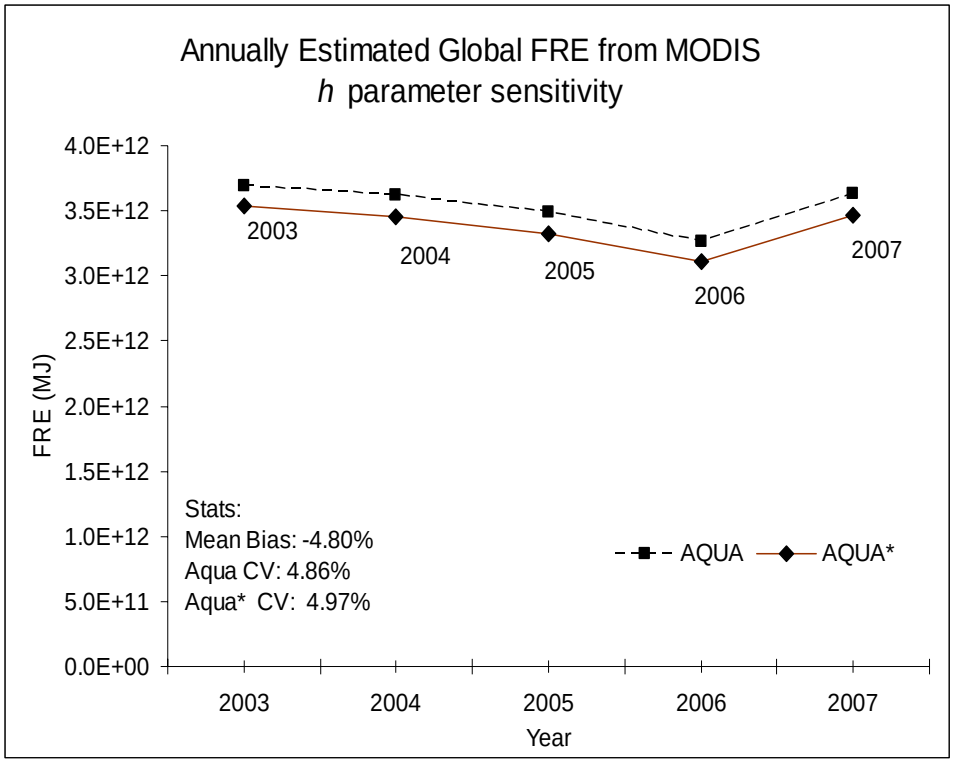

Figure 3.4: A sensitivity test for the modified Gaussian function h parameter. FRE estimates were made using a static h value of 13.64 (red line/triangles) and compared with FRE estimates made with the standard fitting process for h.

On the other hand, applying the same range of T/A ratios to the σ parameter results in a curve width at half maximum of over 4 hours. An example test is presented in Figure 3.4 in which the *h* value was fixed at 13.64 (based on using a global mean T/A ratio of 0.76) and FRE modeled using the fit shown in Figure 3.5a. The chart shows a 4.8% mean annual global underestimation in FRE when using a static *h* value, suggesting that this parameter does not strongly influence FRE, assuming the value is reasonable (i.e. a peak hour typically near noon local time). Monthly mean bias between 2003 and 2007 was similar as well (4.7%).

The background level of the diurnal cycle, *b*, (Figure 3.5c) shows a small level of constant FRP for most fires sampled over Africa (less than 0.1). However, substantial background is observed over the boreal sites with *b* nearly 1.0 for T/A ratio. This is indicative of fires that burn more continuously (i.e. day and night).It should be noted that the diurnal cycle characterization is based on observations made using SEVIRI, TRMM, and two high latitude regions for MODIS. Application of this process to other regions will include some amount of error and this uncertainty is discussed later in the dissertation.

3.3.2 Computation of the FRE from Aqua CMG FRP and T/A ratio

Using the relationships calculated in Figure 3.5 and the mean T/A ratio per cell, FRE was estimated using MODIS CMG FRP for 2001 – 2007. The CMG product was chosen because it offers a global scale dataset necessary for comparison with the OCBC inversion product (Chapter 4). Additionally, it offered an output product which is appropriate for use with climate models, while retaining temporal and spatial

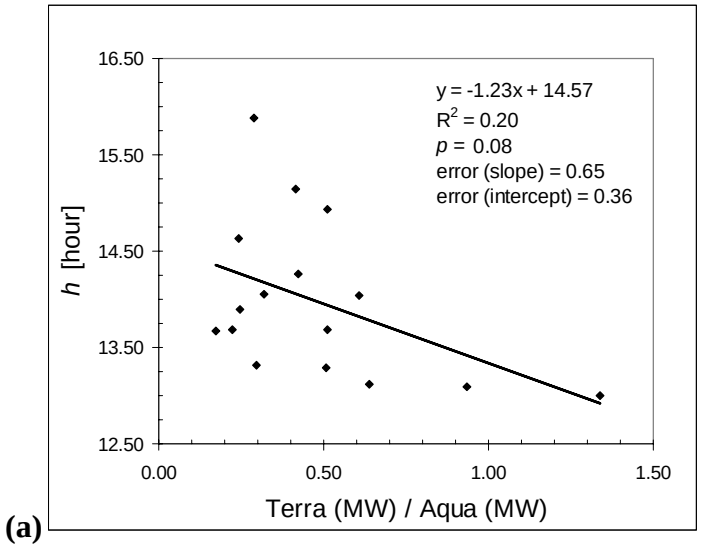

(a)

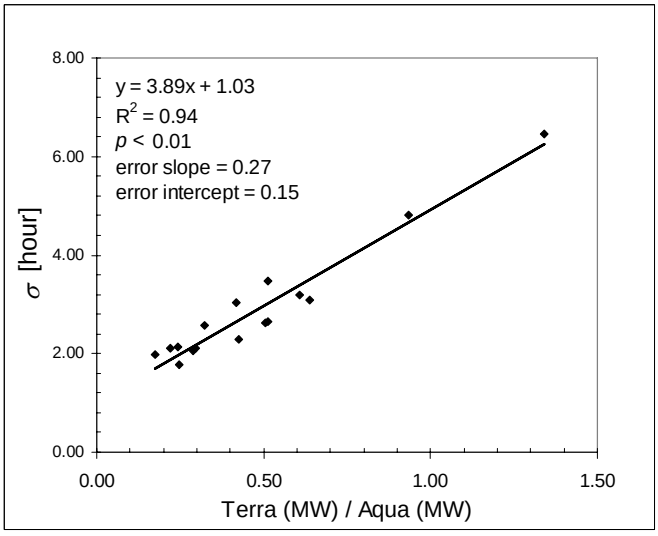

(b)

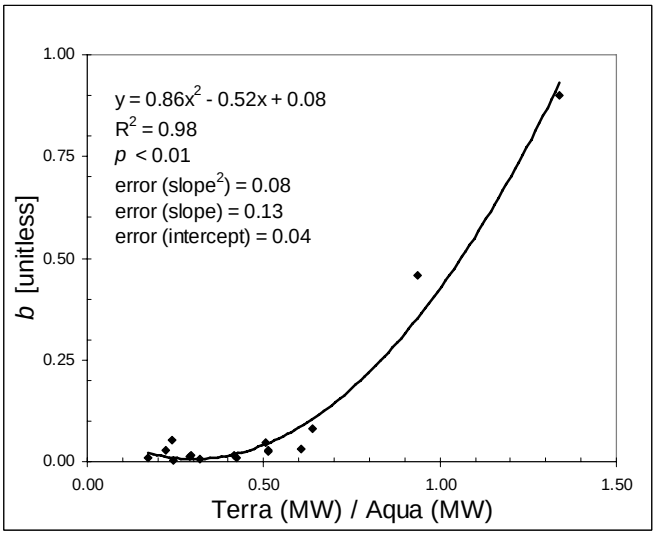

(c)

Figure 3.5: (a) Variation of the peak hour of the diurnal cycle, h, as a function of the Terra/Aqua FRP ratio. Note that the relationship is weak ($R^2 = 0.2$) and not significant at $p < 0.05$; (b) The width of the diurnal cycle, σ, as a function of the Terra/Aqua FRP ratio. The σ value (in hours) corresponds with the width of the curve at half-maximum FRP; (c) Variation of the background level of the diurnal cycle, b, as a function of the Terra/Aqua FRP ratio.

resolution adequate for regional discrimination of fire activity. Terra MODIS FRP was used for 2001 and 2002 as Aqua MODIS was not yet available (only partial availability in 2002). Subsequent years (2003-2007) were estimated with Aqua. The MODIS CMG FRP represents the sum of the FRP obtained during the day and night overpasses, therefore, using Aqua as an example, the following equation can be written, being adopted for the fire diurnal cycle described in the previous section:

$$CMG\ FRP = FRP_{peak}[(b + e^{-\frac{(13.5-h)^2}{2\sigma^2}}) + (b + e^{-\frac{(01.5-h)^2}{2\sigma^2}})] \quad (3.4)$$

CMG FRP is the total (mean *x* cloud-and-overpass corrected pixel count) FRP value from the CMG product.

There are two reasons to justify not setting FRP_{peak} to be equal to the Aqua CMG FRP; (1) as stated earlier, this value is the summation of *both* day and night fire retrievals and cannot be assumed to be just the daytime peak FRP, and (2) although the Aqua afternoon (1330) overpass roughly corresponds with peak fire activity, there is a range of hours over which the true peak may occur (e.g. 1300 to 1800 local hour) as reported by *Giglio* [2007].

FRP_{peak} is computed in two steps: 1) Using the T/A ratio *b*, *h* and σ are estimated using the empirical relationship derived in section 3.3.1 (Figure 3.5). The *b*, *h* and σ parameters are then used to compute FRP_{peak} using equation (3.5):

$$FRP_{peak} = \frac{CMG\ FRP}{(b + e^{-\frac{(13.5-h)^2}{2\sigma^2}}) + (b + e^{-\frac{(01.5-h)^2}{2\sigma^2}})} \quad (3.5)$$

The fire radiative energy (FRE) is then computed as:

$$FRE = \int_0^{24} FRP_{peak}\,(b + e^{-\frac{(t-h)^2}{2\sigma^2}}) \qquad (3.6)$$

Examination of the yearly difference between Terra and Aqua estimated FRE for 2003 - 2007 (when both sensors were available) revealed a small mean annual bias in FRE (1.4%) which was subsequently applied to Terra MODIS FRE estimates for 2001 and 2002.

3.4 Results & Discussion

3.4.1 FRE

The estimated mean global FRE for 7 years (2001-2007) is shown in Figure 3.6. MODIS-based FRE estimates were first assessed for 12-months of data with FRE estimated from SEVIRI. Results, as seen in Figure 3.7, suggest a good agreement between monthly estimates of FRE. (y=0.78x, R^2=0.85, E = 0.50, $p < 0.01$). The RMSE was 54e+09 MJ, or approximately 34% of the SEVIRI monthly mean FRE. MODIS and SEVIRI were both adjusted for atmospheric attenuation (MODIS is explained below while the SEVIRI dataset were corrected by *G. Roberts* using MODTRAN). The underestimation of MODIS FRE may be due to incomplete characterization of the temporal cycle of FRP in as well as overcorrection in the SEVIRI product, which is intended to account for omission errors [*Roberts and Wooster*, 2008]. It should be clear that although SEVIRI data was used to develop the temporal trajectory of FRP this does not influence the magnitude of the actual

discrete estimates of FRP made using MODIS. An additional comparison of the FRE estimates from Aqua MODIS (692×10^9 MJ) for July, August, September and October 2004 with FRE reported by *Roberts and Wooster* [2008] from SEVIRI (921×10^9 MJ), for the same period and corresponding area in southern Africa, reveals that the MODIS FRE values appear consistent.

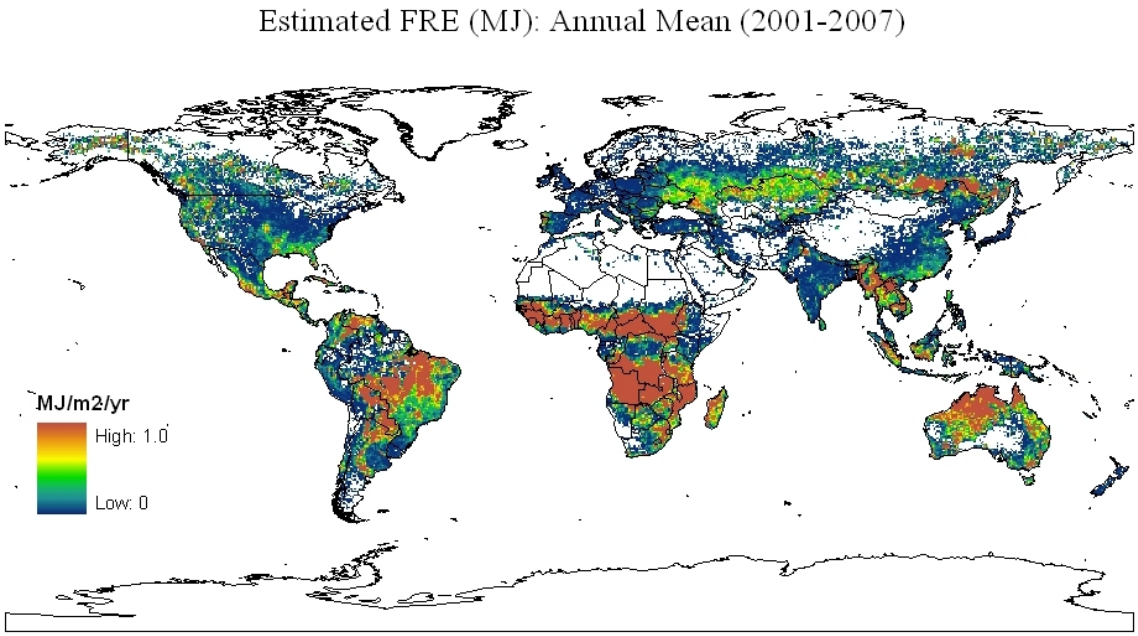

Figure 3.6: Estimated annual mean FRE (MJ/m^2) from Aqua (2003-2007) and Terra (2001-2002) MODIS. Integrated energy was calculated from FRP (MW) values derived from a Gaussian function using modeled parameters.

Atmospheric correction was applied to MODIS FRP calculations using the approach described in Chapter 2. Since nominal view angles are not available in the gridded CMG dataset, an average view angle was assumed. The CMG FRP aggregation excludes any observations with scan angles greater than 40° and therefore an assumed average scan angle of 20° for the CMG product was employed. The average scan angle corresponds with a 22.33° view angle which was used in the atmospheric correction scheme. To test the effect of the scan/view angle assumption, the simulated FRP from Chapter 2 were plotted again (see Figure 2.16), but instead of explicitly using the view angle information from the simulations, the exponential correction factor was applied to the inverse cosine of 22.33° for all observations (Figure 3.8). The results indicated that the view angle assumption offered a good fit to the simulated surface FRP, and while the RMSE nearly doubled, the error was a rather small proportion of the mean and median surface FRP value (6.4% and 8.6%, respectively).

Regional distribution of FRE showed that Africa, South America, and Australia dominate in terms of energy liberated from biomass burning. Africa, often referred to as the "fire continent", was responsible for nearly half of the global annual average fire radiative energy. Partitioning global results using the Global Fire Emissions Database regional map (see Figure 3.1) [*van der Werf et al.,* 2006] showed Africa (NHAF and SHAF) generated, on average, 47% of the global FRE. South America (NHSA and SHSA) was responsible for another 20% of the mean annual FRE with SHSA accounting for 18.5% of this.

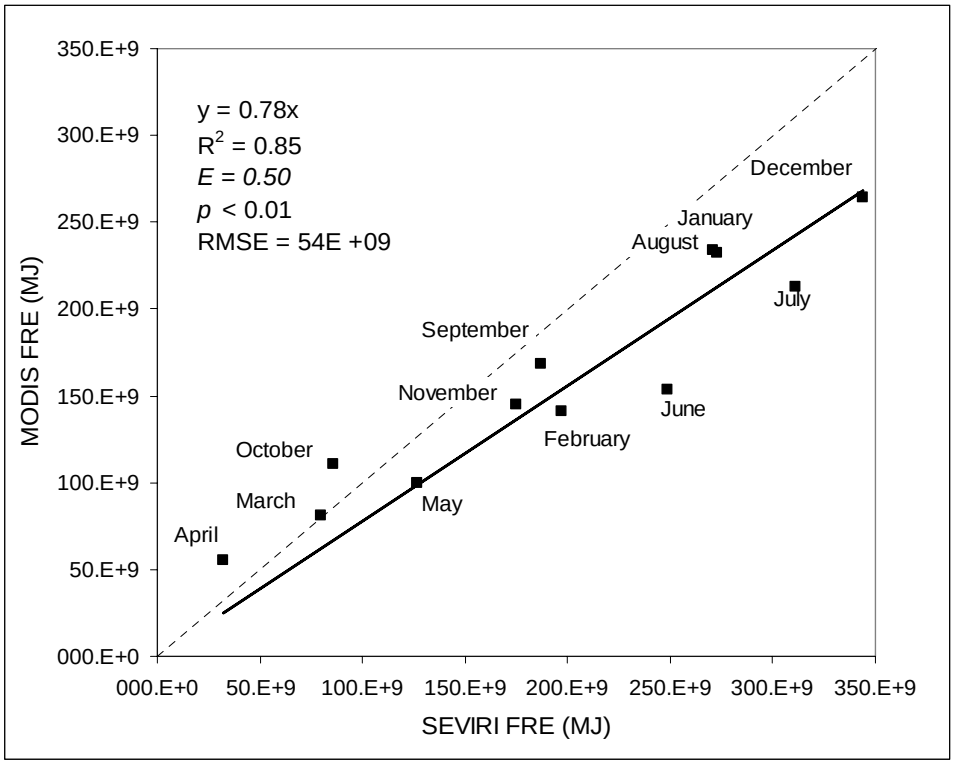

Figure 3.7: FRE comparison for Africa 2004 between MODIS, estimated using the parameterization method described in this paper, and SEVIRI from *Roberts and Wooster* [2008, *personal communication*]. The dashed 1:1 line is shown for reference.

Of particular interest in South America is the "arc of deforestation" [*Fearnside and Hall-Beyer*, 2007] which was responsible for 68% of the average FRE in the southern-hemisphere South America (SHSA) region and 13% globally. Other regions of intensive fire activity are Australia (9%), boreal fires (BONA and BOAS) which made up roughly 7.5% and Central and Southeast Asia (CEAS and SEAS) with approximately 5% each. These proportions are consistent with previous estimates of fire detections and emissions [*Dwyer et al.,* 2000; *Bond et al.,* 2004].

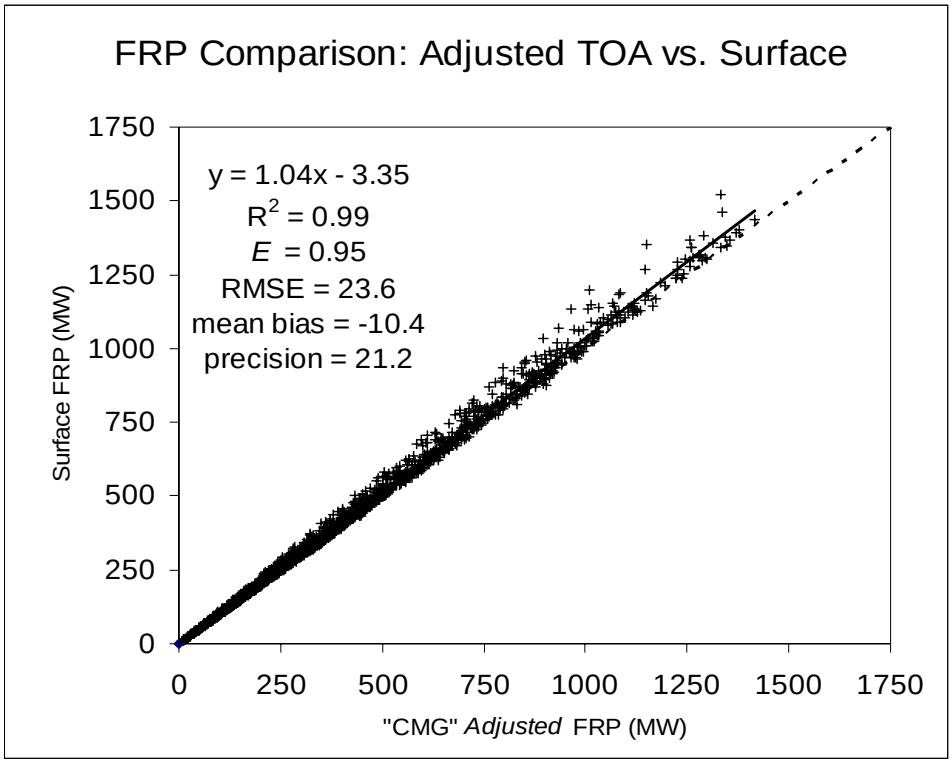

Figure 3.8: Simulated TOA CMG FRP, "corrected" for atmospheric effects, compared with simulated surface FRP. "CMG" FRP is adjusted using an assumed mean view angle of 22.33° and the exponential correction factor (Figure 2.15) for all "observations". The 1:1 (dashed) line is plotted for reference.

3.4.2 Biomass Consumed

The next step was to estimate the dry biomass consumed from fire using an FRE-based combustion factor (0.368 ± 0.015 kg/MJ) established by *Wooster et al.* [2005]. The combustion factor was developed from experiments using fuels representative of dry season savanna vegetation fires. As such, the comparison was constrained to biomass burning in Africa for which the fire experiments were intended [*Roberts et al.,* 2005; *Roberts and Wooster*, 2008].

A 12 month total biomass consumed comparison using SEVIRI FRE (858 Tg DM) and MODIS FRE (700 Tg DM) revealed agreement in the estimates, but again a

roughly 20% underestimation by MODIS seen in the FRE approximation (Figure 3.7). Although using a static FRE-based combustion factor based on *Miscanthus* fuels may seem to neglect the heterogeneous nature of wildland fires, *Freeborn et al.* [2008] demonstrated that fuel type was relatively insignificant (<12%) in explaining the variability in biomass consumption as a function of FRE. This is supported by previous investigations of fuel heat yield [*Stott*, 2000]

Comparing the biomass consumption estimates from MODIS for Africa with the GFEDv2 highlights the significant differences in annual estimates. FRE-based estimates had an average biomass burned of 726 ± 30 Tg DM for Africa between 2001 and 2007, or roughly 3.5 times less than reported in the GFEDv2 (2586 Tg DM). Alternatively, using the recently published combustion factor (0.453 ± 0.068 kg/MJ) from *Freeborn et al.* [2008] reduced the margin of difference (894 ± 134 Tg DM), but was still nearly a factor of 3.

Based on a similar result found by *Roberts and Wooster* [2008] fuel load (kg/m^2) estimates were investigated as a potential source of bias. The FRE-based fuel load was estimated using biomass burned (described above), burned area from *Giglio et al.* [2009], and the annual mean combustion completeness for Africa (0.77) reported in the GFEDv2. Mean fuel load for Africa between 2001 and 2007 was estimated to be 1.58 kg/m^2 in the GFEDv2 while 0.38 kg/m^2 for the FRE-based estimate, indicating the discrepancy in biomass consumed may be directly related to this difference. *Reid et al.* [2005] reported a mean grassland/savanna fuel load from a literature review of 0.4 kg/m^2 which corresponds well with fuel load measures for Africa savannas made by *McNaughton et al.* [1998] and *Hely et al.* [2003] (0.35 and 0.38 kg/m^2,

respectively). These results suggest that the fuel load estimates used in the GFEDv2 are indeed high. Although these values are for grassland/savanna only, which are generally lower than woody vegetation biomes, their use is appropriate in most cases for Africa since this is the dominant biome in which fire occurs [*Dwyer et al.*, 2000].

Finally, annual emissions of carbon and CO_2 for Africa were estimated. Applying the combustion factor by *Wooster et al.* [2005] and assuming a dry matter carbon content of 45% a mean of 326 ± 13 Tg C yr^{-1} and a CO_2 range of 1196 ± 49 Tg CO_2 yr^{-1} was calculated.

3.5 Conclusions

A method to estimate fire radiative energy from discrete MODIS FRP observations was presented. The approach was developed from SEVIRI, VIRS, and MODIS data to characterize the fire diurnal cycle as a modified Gaussian function. The function variables are parameterized based on the relationship with monthly Terra/Aqua (T/A) FRP ratios from 16 globally distributed regions. Sensitivity analysis of the parameter describing the hour of peak fire energy (h) revealed that despite a poor agreement between the regional curving fitting and T/A ratio for this parameter, it played a relatively minor role in the FRE estimation process. Atmospheric attenuation was accounted for based on the exponential fit described in Chapter 2. The correction for the CMG FRP product assumed a mean view angle of 22.33°, and while this assumption incurs a degree of error it is relatively small compared to the potential error introduced by ignoring atmospheric effects. The FRE calculation described in this chapter is a potentially significant contribution to remote

sensing science as the calculation of FRE from MODIS FRP has not yet been achieved, and therefore presents a first of its kind. Comparison is limited, but initial evaluation against FRE estimates from the geostationary SEVIRI sensor indicated that the approach presented produces comparable estimates. The underestimation of MODIS FRE suggests room for improvement as well as potential overcorrection for omission errors in the SEVIRI product [*Roberts and Wooster*, 2008].

Chapter 4: Estimating Global Biomass Burning Emissions of Organic and Black Carbon[7]

4.1 Introduction

Aerosols influence Earth's radiative balance through scattering and absorbing the shortwave radiation. The Intergovernmental Panel on Climate Change (IPCC) [2007] reported the direct radiative forcing impact of biomass burning aerosols as 0.03 Wm^{-2}, with approximately a factor of 4 uncertainty (±0.12) In addition, aerosols can influence Earth's climate in more complex and indirect pathways such as changing cloud albedo and lifetime. However, there is good deal of uncertainty in estimating the forcing effects of biomass burning aerosols, in part due to an incomplete understanding of the optical properties of smoke and aerosol-atmosphere interactions. A prerequisite to understanding these interactions at regional and global scales is reliable estimates of aerosol emissions from wildland fires, both spatially and temporally. As discussed in Chapter 1, although efforts to quantify biomass burning emissions have improved over the past several decades the inaccuracies of input data and variations in the methodologies employed may lead to an uncertainty in emission estimates of at least 50%, and possibly much greater [*Robinson*, 1989; *Andreae and Merlet*, 2001; *van der Werf et al.,* 2003; *French et al.*, 2004; *Korontzi et al.*, 2004].

The rate at which energy is emitted by a fire, or the fire radiative power (FRP), during combustion can serve as a proxy for the rate of gas and aerosol emissions

[7] The majority of this chapter was published in *Vermote, Ellicott, et al.* [2009]

released [*Kaufman et al.*, 1996; *Kaufman et al.*, 1998]. Integrating the FRP over the lifespan of a fire event and multiplying this value by an emission coefficient (EC_x), which describes the quantity of gas or particulate matter emitted per megajoule (MJ) of energy released (g/MJ), yields the total emissions from a fire (equation. (4.1)). (Note: The term *Emission Coefficient* [*Ichoku and Kaufman,* [2005] rather than *Emission Factor* is used to avoid confusion between the former, which is in units of grams per energy released, and the latter which is in grams per mass of fuel consumed (g/kg)).

$$Emission_x = EC_x \int FRP\, dt \tag{4.1}$$

In this chapter the relationship between the estimates of FRE made in Chapter 3 and a new MODIS-derived inversion product of daily integrated biomass burning aerosol emissions is explored. The inversion product is generated from the MODIS fine mode aerosol optical thickness and inverse modeling transport processes adopted from the Goddard Chemistry Aerosol Radiation and Transport (GOCART) model. The inversion yields the sources (locations and intensities) of fine mode aerosols [*Dubovik et al.*, 2008] attributed to biomass burning. Fine mode aerosols are defined as particles with an aerodynamic diameter less than 2.5μm (PM2.5). The fine mode aerosol optical thickness is converted to mass using a conversion factor (see Section 4.2). The organic and black carbon (OCBC) mass is then calculated based on the proportion of PM2.5 mass composed of OCBC which was reported by *Andreae and Merlet* [2001] for the three biomes considered in this study. Although it could be suggested that emission estimates be made utilizing only the inversion product,

production of this product is still rather time-consuming and it is not intended for an operational approach.

The relationship between FRE and OCBC estimates within several biomes is investigated to generate emission coefficients. The slope of the relationship within each biome is used as the representative emission coefficient to forward model estimates of OCBC from FRE. As previously stated, this type of generalization will incur a degree of uncertainty and given the incomplete understanding of aerosol optical properties a level of uncertainty in any emission estimate is implicit. Therefore these and other issues are addressed in an error budget (Section 4.4).

An overview of the data and products used in this Chapter is provided in section 4.2. The methodology used to generate FRE-based emission coefficients is presented in section 4.2.3, while section 4.3 offers a review of the potential sources and magnitude of error in the data and estimates. Results are provided and discussed in section 4.4 with concluding remarks in section 4.5.

4.2 Materials and Methods

4.2.1. OCBC Emissions from Inverse Modeling

Contrary to conventional approaches which rely on the emission inventories, this study incorporates OC and BC emission fields using global observations of aerosol from satellites. The distribution of fine mode aerosol optical thickness (AOT) derived from MODIS measurements allows global monitoring of the daily dynamics of biomass burning events. However, these AOT distributions do not provide detail regarding the exact location and strength of the aerosol emission sources since the

aerosol fields observed from satellites include both freshly emitted aerosol and aerosol emitted prior to the actual satellite overpass; the latter being redistributed and transformed by atmospheric processes (advection by winds, rain washout, deposition, etc.). Therefore, this study relies on the information provided by inverse modeling that accounts for atmospheric processes and derives the aerosol emissions from satellite observations. Specifically, the aerosol source information retrieved by the *Dubovik et al.* [2008] algorithm from MODIS fine mode aerosol AOT measurements was used.

Dubovik et al. [2008] used the Goddard Chemistry Aerosol Radiation and Transport (GOCART) aerosol transport model to invert MODIS optical depth measurements to derive a spatially and temporally resolved description of surface fine mode aerosol sources. These aerosol sources produce other species besides those generated from biomass burning, such as anthropogenic combustion (e.g. from coal burning), which represent a very small fraction of emissions in the regions of significant fire activity and can be neglected in this analysis. Although exceptions do exist (for example, Northern India) they are limited. The fine mode aerosol is converted to PM2.5 mass by using the average mass extinction coefficient (β_e) value of 7.6 ± 1.9 m^2/g which relates the dry mass of particulate matter to the fine mode optical depth [*Chin et al.,* 2002]. Organic and black carbon mass were then estimated from the PM2.5 mass using an average fraction of 0.68 [*Andreae and Merlet,* 2001]. Organic carbon, associated with smoldering combustion, is characterized by light scattering properties and thus has implications for negative climate forcing. Black carbon, on the other hand, is generally a product of flaming combustion and

dominates light absorption by aerosols, resulting in a positive climate forcing [*Lenoble,* 1991; *Sato et al.,* 2003]. The typical ratio of OC to BC adopted in this research is 7:1 [*Chin et al.,* 2002].

Total OCBC emissions for 2003 (30.5 Tg) are shown in Figure 4.1. Regions of fire activity are clearly visible, including the Arc of Deforestation in Brazil, Central America (e.g. Yucatan Peninsula), Southeast Australia, Southern Africa, and Southeast Russia. There are regions where the OCBC product is not fully corrected for anthropogenic and biogenic sources which can be seen in Eastern China, Europe, and portions of the United States south of the Great Lakes.

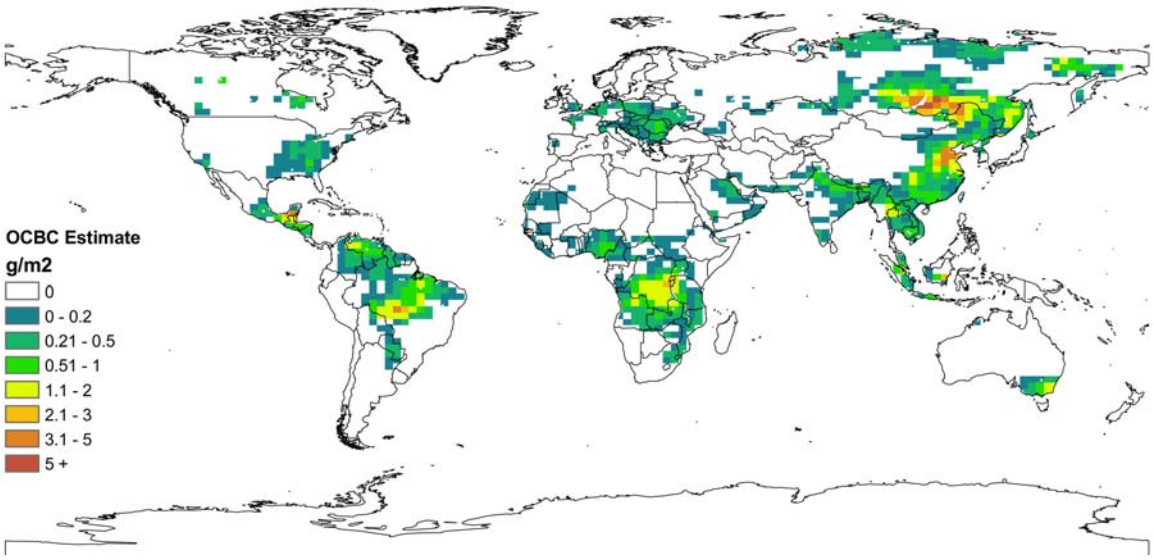

Figure 4.1: Organic and black carbon particulate matter emissions mass (g/m^2) for 2003 (30.5 Tg) estimated through observations from MODIS and inverse transport modeling with GOCART.

Dubovik et al. [2008] optimized the inversion process by employing adjoint modeling to reduce the computational burden of modeling back trajectories. Despite this, the

inversion process is still time-consuming and not realistic as a near-real-time operational product. Therefore the approach to estimate emissions using FRE and FRE-based emission coefficients provides a simple and efficient method by combining the robustness of the inverse method with the temporal variability obtained from near real-time observations of FRP.

4.2.2. FRE

Fire radiative energy monthly estimates from 2003 were generated using the process described in Chapter 3 and used for comparison with the OCBC estimates above. Figure 4.2 shows the monthly average FRE (MJ) per m^2 in 2003.

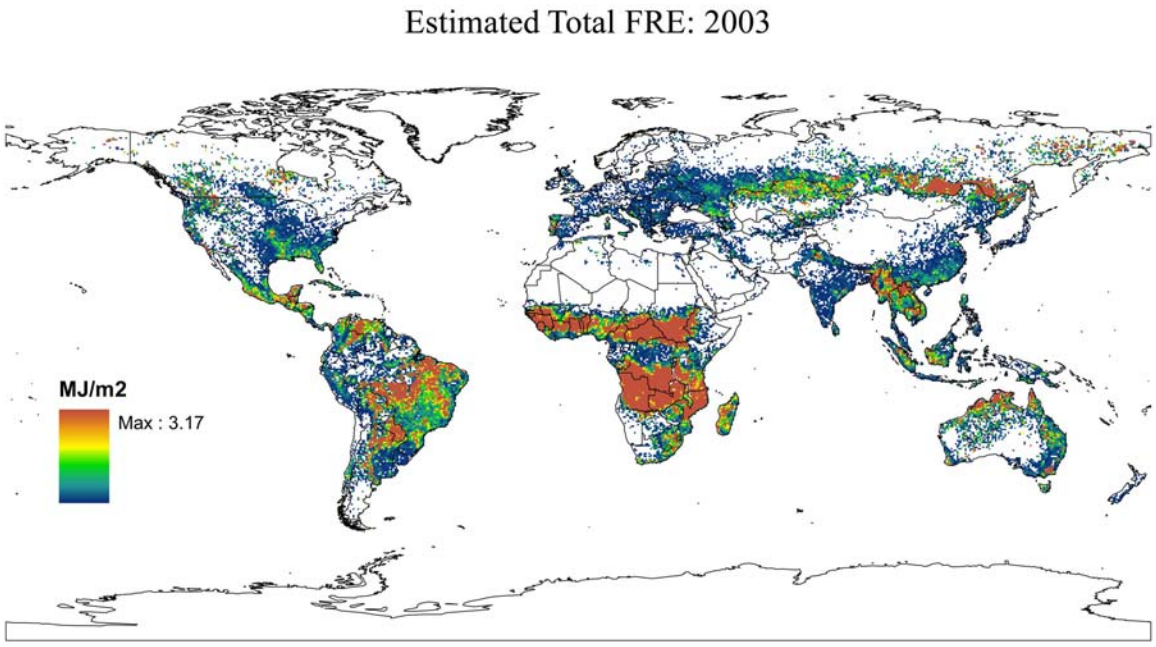

Figure 4.2: Estimated 2003 FRE (MJ/m^2) from Aqua MODIS. Integrated energy was calculated from FRP (MW) values derived from a Gaussian function using modeled parameters.

4.2.3 Emission Coefficients

The emission factor is generally defined as the amount of gas or particulate matter emitted (g) per mass of fuel consumed (kg). The factors are typically based on extensive field and laboratory validation and applied across similar biomes [*Andreae and Merlet*, 2001]. Evaluation of uncertainty in emission factors [*Robinson*, 1989] and the wide range of values reported in the literature [*Andreae and Merlet*, 2001; *Chin et al.*, 2002; *Chin et al.*, 2007; *Freeborn et al.*, 2008], suggests emission factors vary naturally by at least 30%.

In their research on rates of energy and aerosols released from fires *Ichoku and Kaufman* [2005] explained that replacing the fuels consumed (*M*) in equation (1.1) with FRE necessitates that the emission factor must be based on fire energy. Thus, an emission factor for OCBC is expressed using g/MJ instead of g/kg. This is referred to as the *Emission Coefficient* (*EC*) to avoid any confusion with the traditional term.

The FRE and OCBC emission product were compared over multiple sites (Figure 4.3) and constrained by vegetation type, as described by *van der Werf et al.* [2006]. The vegetation types include three broad categories: Non-forest (savanna/grassland), tropical forest, and extratropical forest (which include temperate and boreal forest).

Over southern Africa the area chosen for the analysis contained 95% grassland/savanna fires and 5% tropical forest fires and was used to derive the grassland/savanna emissions coefficient (Figure 4.4) which was estimated to be 2.47 g/MJ with an uncertainty of 0.27 g/MJ.

a.

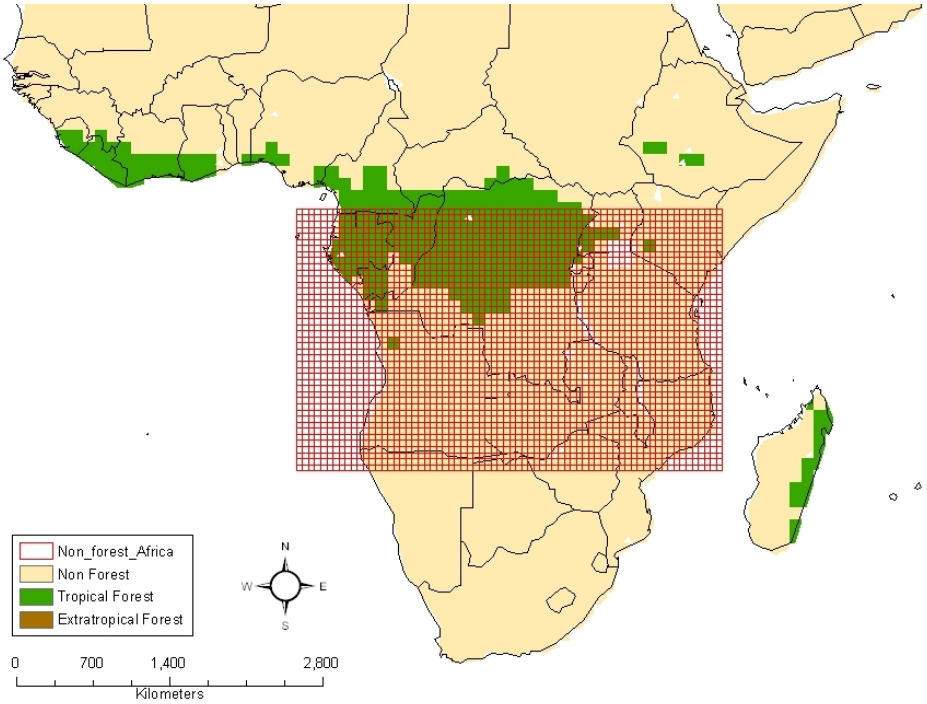
Non_forest_Africa
Non Forest
Tropical Forest
Extratropical Forest
N
W
E
S
0
700
1,400
2,800
Kilometers

b.

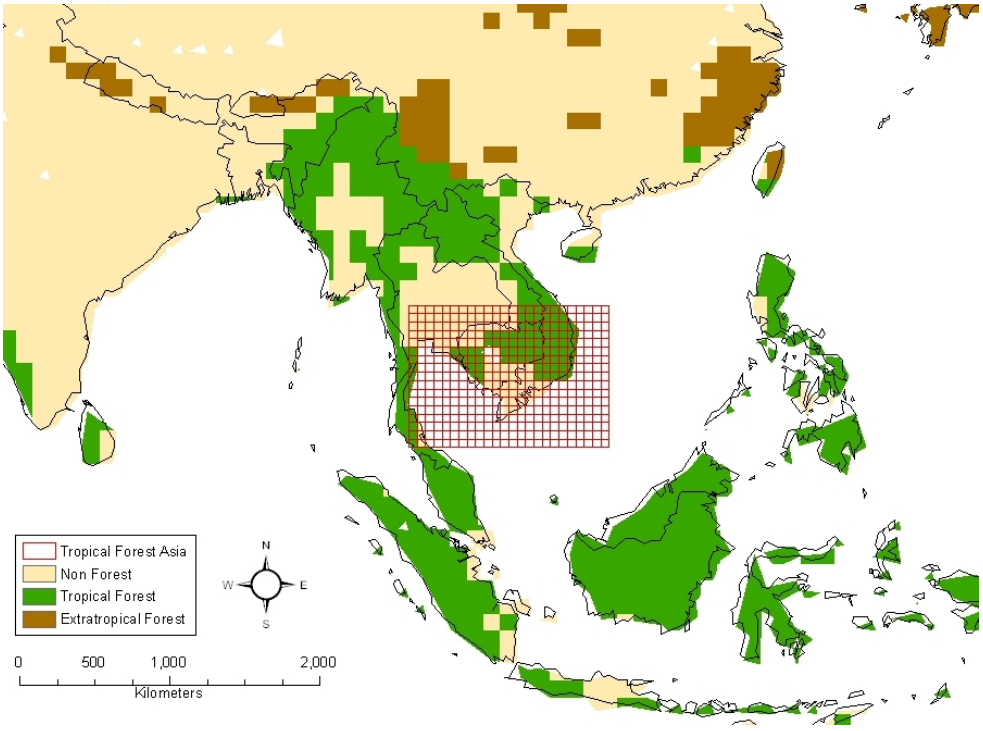
Tropical Forest Asia
Non Forest
Tropical Forest
Extratropical Forest
N
W
E
S
0
500
1,000
2,000
Kilometers

c.

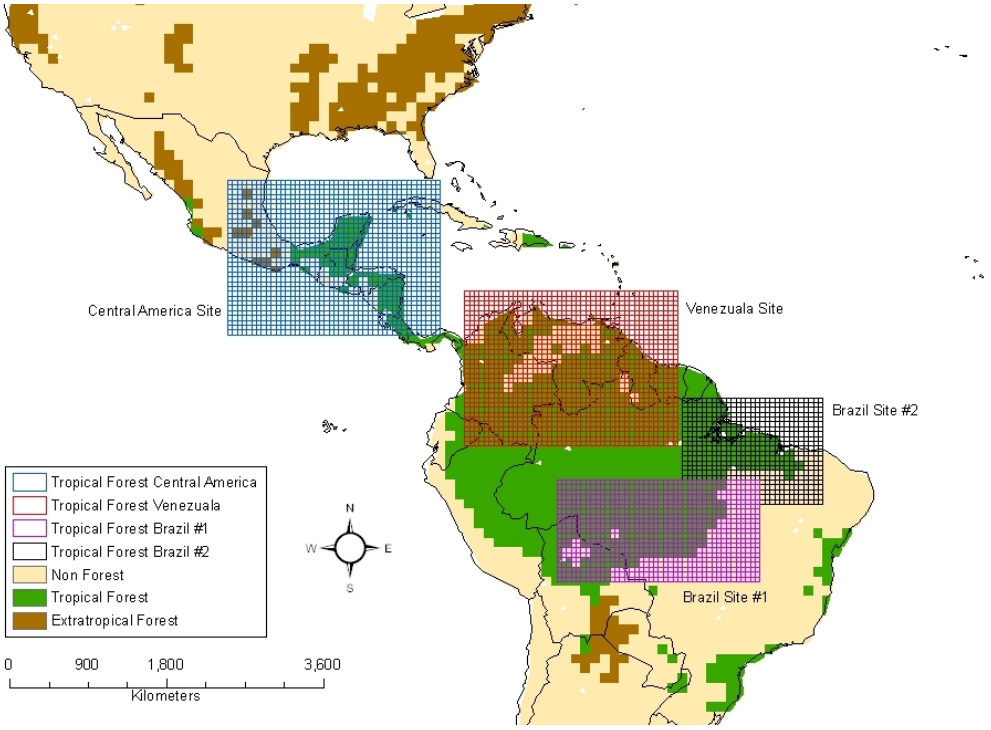
Central America Site
Venezuala Site
Brazil Site #2
Brazil Site #1
Tropical Forest Central America
Tropical Forest Venezuala
Tropical Forest Brazil #1
Tropical Forest Brazil #2
Non Forest
Tropical Forest
Extratropical Forest
N
W
E
S
0
900
1,800
3,600
Kilometers

d.

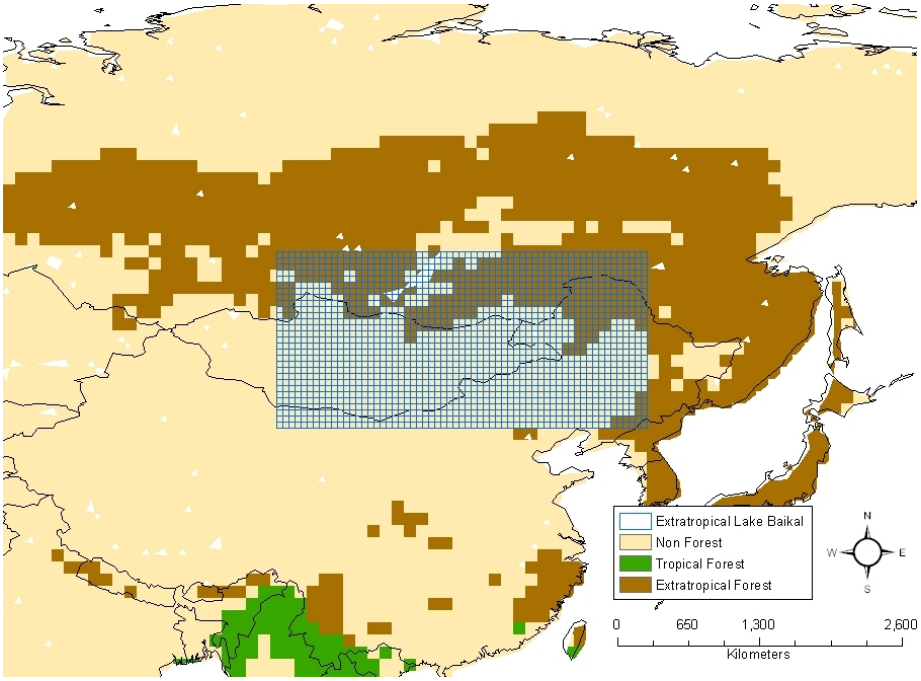
Extratropical Lake Baikal
Non Forest
Tropical Forest
Extratropical Forest
N
W
E
S
0
650
1,300
2,600
Kilometers

e.

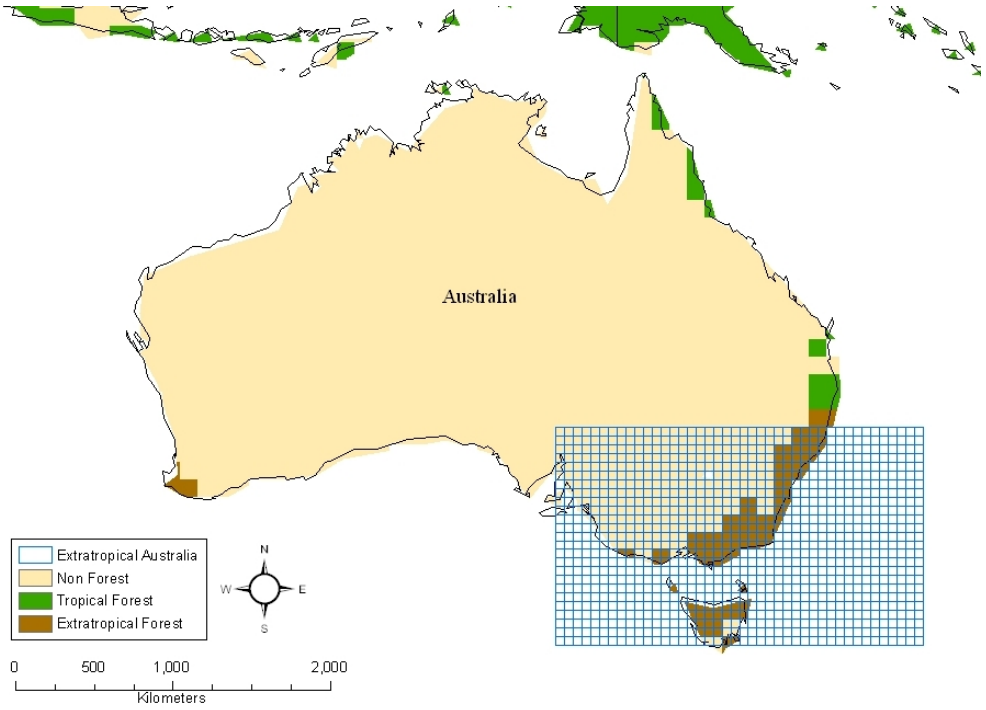

Figure 4.3: The following figures show the emission coefficient sites used to compare FRE and the inversion-based OCBC emissions to determine an appropriate emission coefficient. Comparisons were performed for 3 different biomes based on the vegetation categorization used by *van der Werf et al.* [2006] and available in the GFEDv2. (a) "Non-tropical" site (corresponding with savanna/grassland vegetation); (b and c) tropical forest sites (this is the same as the IGBP's landcover 2); and (d and e) extratropical forest sites.

The emission coefficient can be converted to an emission factor, for comparison-sake, using an energy-to-mass conversion factor of 0.41 ± 0.04 kg/MJ which is the average of the 0.368 ± 0.015 kg/MJ and 0.453 ± 0.068 kg/MJ values found by *Wooster et al.* [2005] and *Freeborn et al.* [2008], respectively. Dividing the emission coefficient by the energy-to-mass conversion factor yields an emission factor of 6.0 ± 1.3 g/kg for OCBC. This is nearly a factor of two higher than the value suggested by *Andreae and Merlet* [2001] for savanna/grassland (OCBC [TC] 3.7 ± 1.3 g/kg). (It should be noted that the

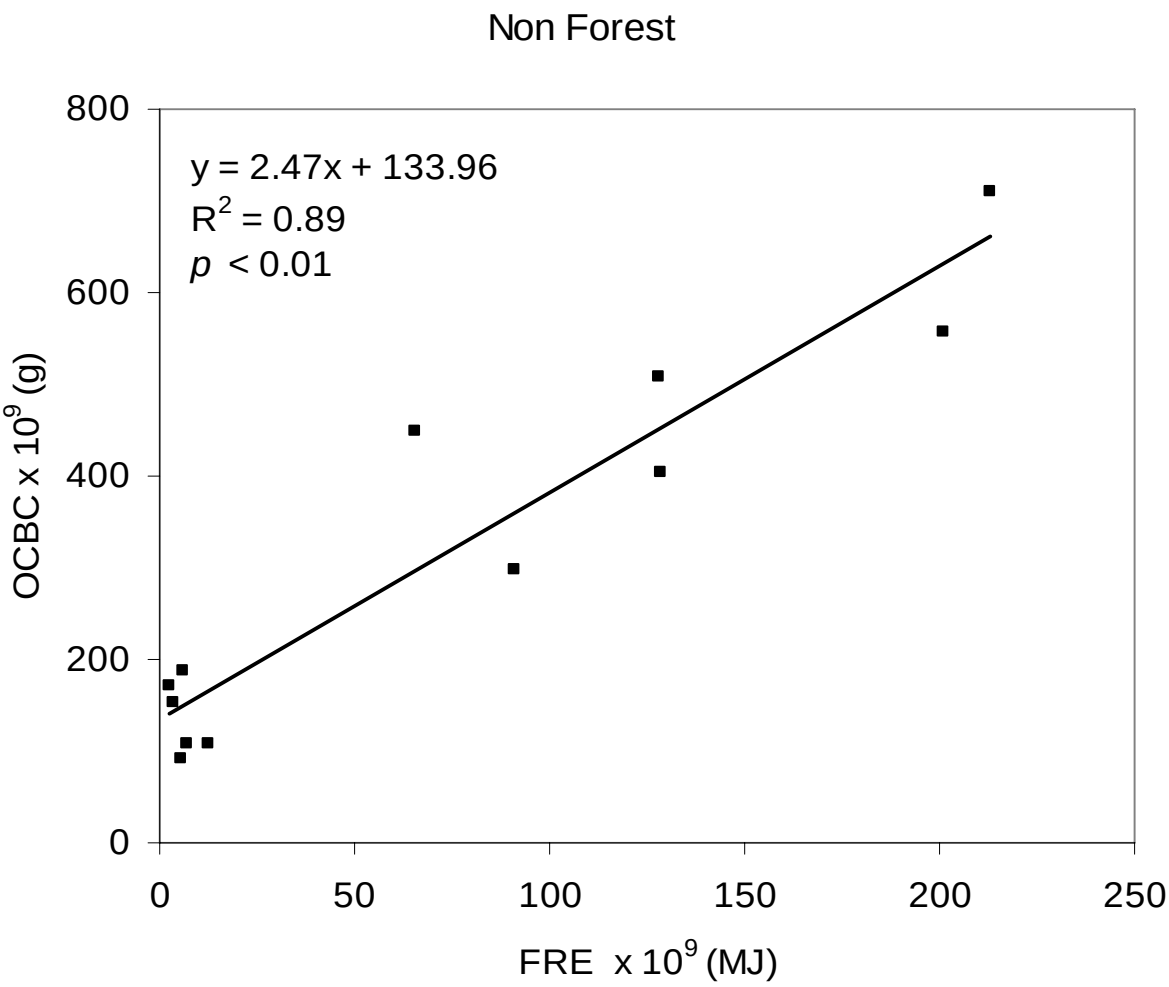

Figure 4.4: Relationship between monthly estimates of FRE and inversion-based OCBC for savanna/grassland biome (see Figure 4.3a) from southern Africa.

emission factors presented by *Andreae and Merlet* [2001] are based on the compilation of EFs reported from multiple authors using various measurement approaches). However, converting the PM2.5 emission factors for "Savanna/Grass" and "Woody Savanna & Cerrado" published by *Reid et al.* [2005] to OCBC emission factors (again, using a 0.68 fraction of OCBC in PM2.5) resulted in 4.5 ± 1.0 g/kg and 5.8 ± 1.4 g/kg, respectively, which tends to agree better with the FRE-based emission factor.

For tropical and extratropical sites (Figures 4.3b & c and 4.3d & e, respectively) a correction was applied to reduce the OCBC emission (per cell) to account for the fraction which was emitted from fires occurring in the grassland/savanna biome category. The average grassland/savanna fraction was 30% in tropical forests and 15% in the extratropical forests.

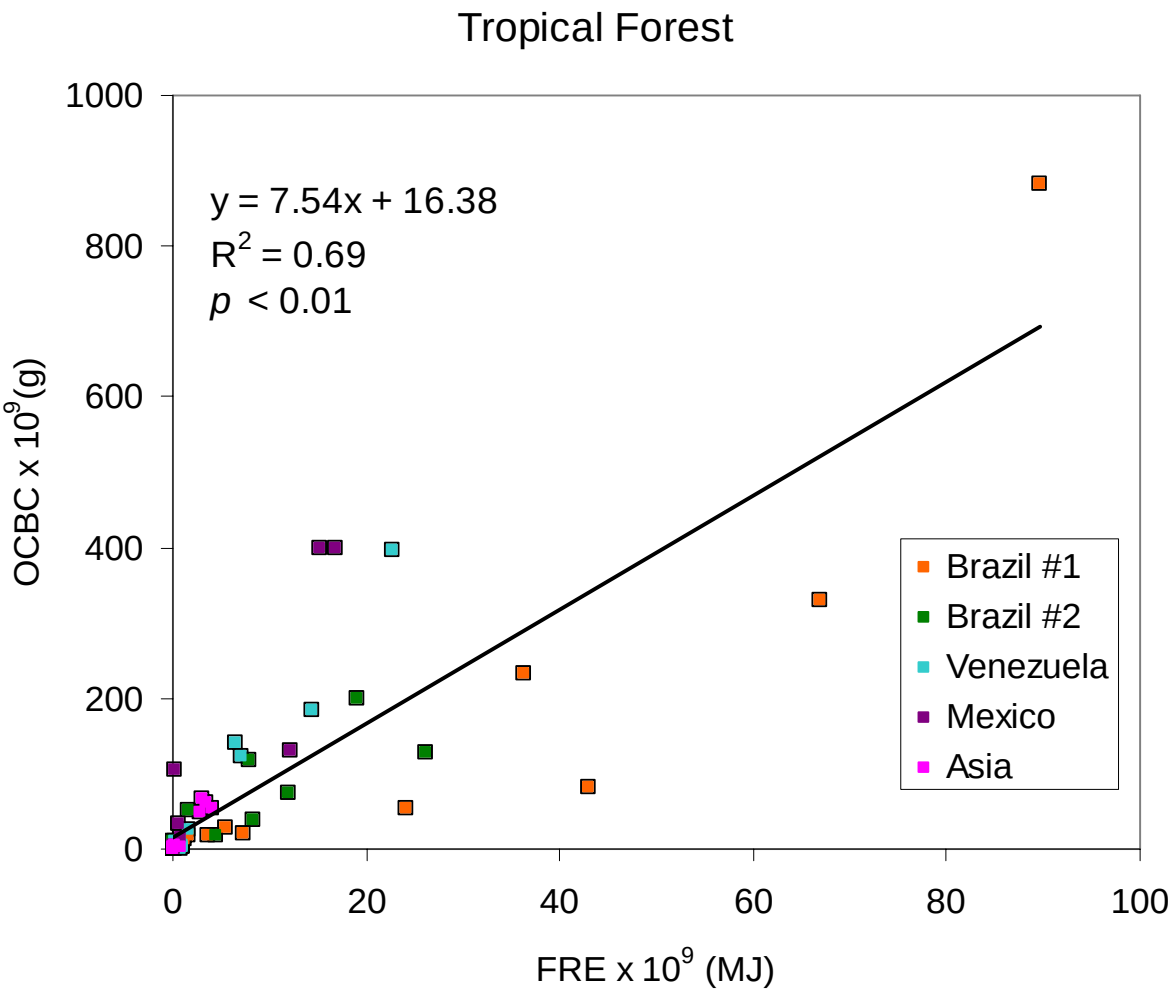

Figure 4.5: Relationship between monthly estimates of FRE and inversion-based OCBC for the tropical forest biome sites (see Figure 4.3b and c).

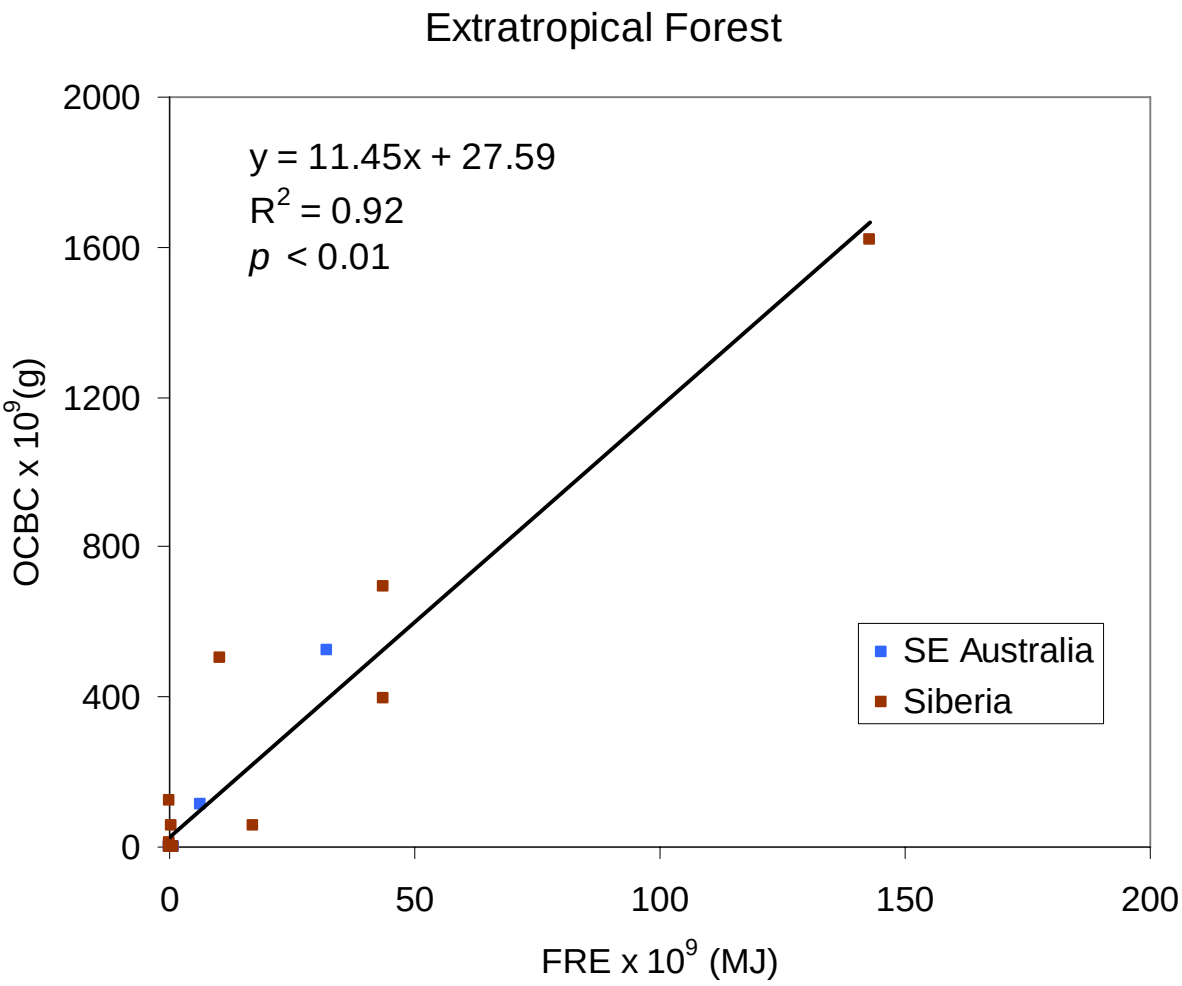

Figure 4.6: Relationship between monthly estimates of FRE and inversion-based OCBC for the extratropical forest biome (see Figure 4.3d and e) from Russia and Australia.

Figure 4.5 shows the derivation of the tropical forest emission coefficient from 5 sites distributed over Brazil (2), Venezuela (1), Mexico (1), and Southeast Asia (1) for which the emission coefficient was estimated to be 7.54 g/MJ with an uncertainty of 0.66 g/MJ. Once converted to an emission factor it equals a value of 18.4 ± 3.5 g/kg, which is again much larger than the value suggested by *Andreae and Merlet* [2001]

(6.6 g/kg). As a point of comparison, the emission factor presented here is closer to *Reid et al.* [2005] (8.3 ± 3 g/kg) and the 11.5 g/kg average tropical forest emission factor recently measured by *Yokelson et al.* [2008]. Once again, this assumes 0.68 fraction of OCBC in PM2.5.

Finally, one site over Southeast Australia and one site in the Lake Baikal region (Russia) were used to derive the OCBC emission coefficient for extratropical forests. Figure 4.6 shows the relationship between OCBC emissions and FRE over these sites. The coefficient obtained was 11.45 g/MJ with an uncertainty of 0.71 g/MJ. The conversion to an emission factor yields 27.9 ± 4.5 g/kg which is higher by a factor of ~3 to 5 than *Andreae and Merlet* [2001] (6.1-10.4 g/kg). For the boreal forests *Reid et al.* [2005] suggested an emission factor of 11 ± 3.5g/kg.

4.3 Error Budget

There is an inherent degree of uncertainty in any statistically-based estimate and when coupled with the use of remotely sensed data the magnitude of error can easily become quite large [*Robinson,* 1989; *Cahoon et al.,* 1991; *Robinson,* 1991). As pointed out by *French et al.* [2004], "little has been done to assess the uncertainty in the resulting [wildland fire emission] estimates". *van der Werf et al.* [2006] offered a thorough review of the sources of uncertainty in biomass burning emission estimates, but fell short of providing a quantitative approximation of each source and the total potential error. Generally, most estimates of uncertainty have been of a similar nature in which the author[s] provides a best-guess [*Andreae and Merlet,* [2001].

Several sources of error impact the accuracy of the estimates made in this research, especially when it comes to the AOT based OCBC emission product, which is computed indirectly from the MODIS fine mode aerosol optical thickness product. These sources were identified (Table 4.1) and the uncertainties calculated for OCBC emission estimates, the emission factors (Section 4.2.3), and the global aerosol burden (which is the input for computing the direct radiative forcing).

The first error source is related to the error in the characterization of the fire radiative energy diurnal cycle that impacts the accuracy of the FRE. Comparison of SEVIRI and MODIS, previously shown in Chapter 3 (Figure 3.6), showed a 27% RMSE which can be attributed to errors in the retrievals from both instruments. Therefore the number used in the error budget (*a* in Table 4.1) was set to the quadratic average ((27%) / (√2)), or 19%.

The accuracy of the empirical formula for computing FRP was taken from the evaluation performed by *Kaufman et al.* [1998] who showed a potential error of 16% using 150 simulated mixed-energy fire pixels. As a corollary, *Wooster et al.* [2003] found a theoretical accuracy (RMSD) of 65 x 10^6 J over a range of 0 to 2000 x 10^6 J (or 6.5% for the average) using their MIR FRE approach. This accuracy estimate was confirmed by the agreement between the BIRD and MODIS independently derived FRP (15%). This error could actually be larger for certain fires since the lower spatial resolution of MODIS appears to prohibit the less intensely radiating fire pixels from being detected. Thus, MODIS underestimates FRE for these fires by up to 46% in comparison to BIRD.

As demonstrated in Chapter 2, there is a component of atmospheric attenuation which the MODIS FRP algorithm does not account for. Although water vapor absorption is weak, several gases can impact energy received in the 4μm channel at TOA. The impact is both dependent on the observation angle and the total amount of gases, and therefore variable. A 20% underestimation in the MODIS FRP estimate, based on 2000+ simulations, was shown in Chapter 2. However, the simulations were for view angles between nadir and 60° and therefore not representative of the CMG product which excludes observations with a scan angle greater than 40°. Assuming a mean scan angle of 20°, corresponding with a view angle of 22.33°, the error in the TOA FRP estimate made by MODIS was calculated to be 17%.

Cloud obscuration impacts FRP estimates through the fact that fires are not detected (omission error). The 11% estimate of omission errors for MODIS fire detections made by *Schroeder et al.* [2008] over the Amazon region is likely a conservative estimate of the impact given the FRP CMG includes cloud correction [*Giglio*, 2005; *Giglio et al.*, 2006]. Along these same lines, *Hawbaker et al.* [2008] found that MODIS omission rates of small active fires were 73% for Aqua and 66% for Terra. Fires may be missed due to rapid burning, cloud cover, or simply because of spatial scales. However, *Hawbaker et al.* [2008] reiterated the point made by *Kaufman et al.* [1998] that these small fires likely have little impact in terms of total emissions.

The accuracy of aerosol optical thickness (AOT) measured by MODIS, determined based on comparisons with AERONET sun-photometer measurements, was estimated to be 0.05 + 15% over land and better over ocean [*Remer et al.*, 2002;

Levy et al., 2007]. The fine mode AOT accuracy is degraded to 0.05 + 20% (Levy, personal communication 2008). Therefore, assuming a mean AOT of 0.5, an error estimate of 30% was used.

The fine mode AOT was converted to PM2.5 dry mass using a value of 7.6 m^2/g for the mass extinction efficiency (β_e). This value assumes a fixed proportion of carbon in the PM2.5, as well as a particular density and relative humidity [*Chin et al.*, 2002]. Another source of error comes from the conversion of PM2.5 to OCBC using a fraction of 0.68. For example, *Andrea and Merlet* [2001] reported a range of 0.5 to 0.8 OCBC in PM2.5. Given all these factors, an overall error of 25% was assumed on the fine mode AOT to OCBC mass conversion.

Secondary aerosol processes, such as the production of organic aerosol from the photo-oxidation of volatile organic compounds abundant in biomass burning emissions [*Grieshop et al.*, 2008], are difficult to account for and represents a potentially large error source. A 25% error was assumed for this category, recognizing that the error might be larger.

The inversion of the emissions sources is dependent on how well the GOCART model accounts for the different processes. A measure of the accuracy, based on how well the MODIS and GOCART aerosol optical thickness measurements agree, was estimated to be 12% according to *Dubovik et al.* [2008].

FRE to combusted biomass conversion was used in order to convert the emission coefficients to emission factors. The conversion coefficient was originally published by *Wooster et al.* [2005] to be 0.368 g/MJ, but has recently been evaluated to 0.453 g/MJ by *Freeborn et al.* [2008], showing a potential error of 10%.

Using the different error sources in Table 4.1, an accuracy of 58% was calculated for the OCBC estimate, with a similar error for the emission factors. The biomass combusted error was lower (34%), while the error for an estimate of global fine mode AOT using this approach would be 34%. The smaller error in fine mode AOT relative to OCBC is because the conversion to mass [f and g in Table 4.1] is not necessary, and thus less error is introduced. This is an important point because it is fine mode AOT which is used to calculate the radiative forcing impact from biomass burning and thus less uncertainty is associated with the effects of fire on Earth's energy balance.

Table 4.1: Error budget for components used in this research.

Error Sources	Error estimates	Relative error (%)
(a) FRE from FRP (diurnal cycle)	Figure 7. SEVIRI comparison	19%
(b) FRP empirical formula	*Kaufman et al.* [1998]	16%
(c) Atmospheric effect on FRP	*Roberts & Wooster* [2008]	17%
(d) Cloud correction FRP	*Schroeder et al.* [2008]	11%
(e) Fine mode Aerosol optical depth (at 550_{nm})	Levy (pers. Comm., 2008)	30%
(f) Conversion of AOT to mass: b_e	Estimated for range of OCBC mass in PM2.5, relative humidity and ratio of OCBC	25%
(g) Secondary aerosol processes: impact on b_e	*Estimated error allocation might be larger [Grieshop et al.,* 2008]	25%
(h) GOCART inversion	*Dubovik et al.* [2008]	12%
(i) Conversion of FRE to biomass combusted	*Wooster et al.* [2005]*; Freeborn et al.* [2008]	10%
Emission estimate	Quadratic sum (a-h)	58%
Emission factors	Quadratic sum (a-i)	58%
Biomass combusted	Quadratic sum (a-d,i)	34%
Fine mode AOT	Quadratic sum (a-e,h)	34%

4.4 Results and Discussion

Using the monthly FRE product computed in Chapter 3 and the emission coefficients computed in section 4.3 a global OCBC emissions estimate for 2003 from biomass burning was produced (Figure 4.7). A total of 20 Tg of OCBC was emitted from biomass burning globally in 2003. This is lower than the 29.6 Tg of OCBC estimated by *Generoso et al.* [2007] for 2003 using a "top down" modeling approach and the 26.1 Tg reported in the Global Fire Emissions Database (GFEDv2, 2005)[8], but still within the error bars (50%) reported for each of the datasets.

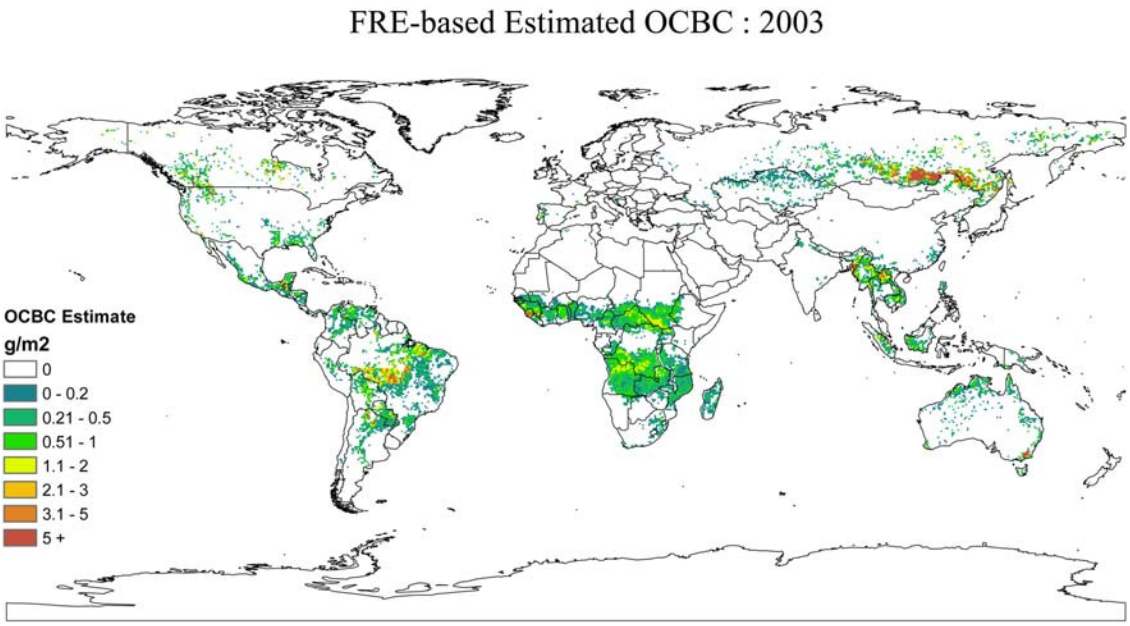

Figure 4.7: Total OCBC (g/m^2) emissions estimated from biomass burning for 2003. High source regions include east-central Brazil, central and southern Africa, Southeast Asia, Central America, and southeast Russia.

[8] GFEDv2 data available at http://ess1.ess.uci.edu/~jranders/data/GFED2/

Figure 4.8 offers a spatially explicit map of the uncertainty in the FRE-based OCBC emission estimate for 2003 based on the 95% confidence interval for the 3 biome specific emission coefficients. For each 0.5° cell, and respective biome, the uncertainty was calculated as the difference between the high and low range of OCBC emission divided by 2. As expected, since a linear relationship was used for the emission coefficients, the regions with the greatest FRE (and subsequently OCBC emission) demonstrate the greatest potential error.

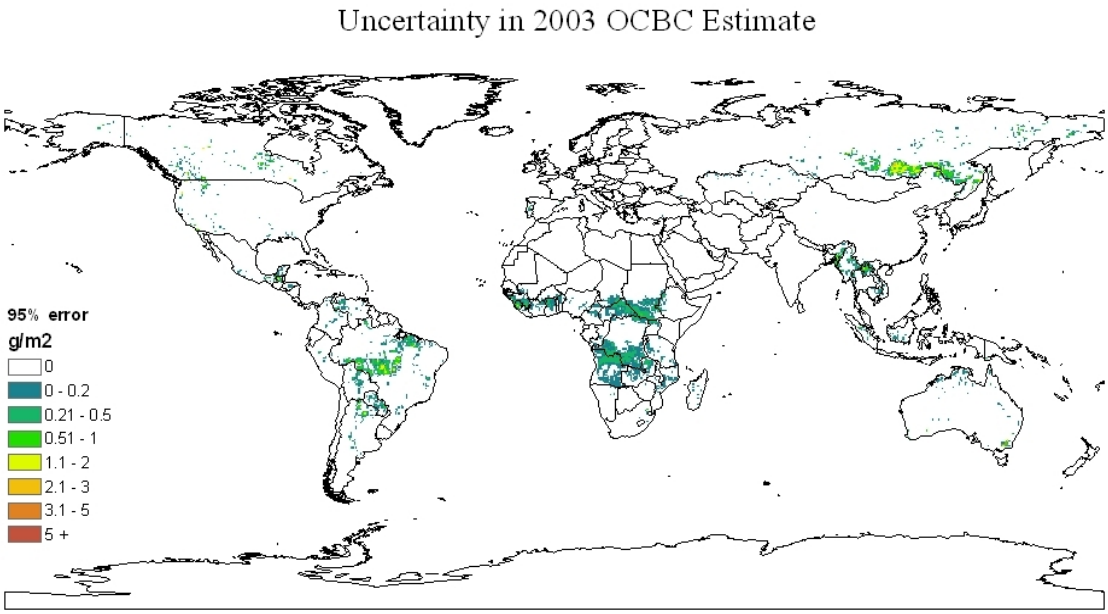

Figure 4.8: Uncertainty in OCBC emission estimates for 2003 (g/m^2).

For comparison purposes the region map (shown in Figure 4.9) used by *van der Werf et al.* [2006] was used. Africa (SHAF and NHAF) produced the greatest source of

OCBC emissions (5.2 Tg) in 2003 accounting for nearly 26% of the global burden. This is almost half of what is estimated in the GFEDv2 (9.2 Tg). Annually, Africa usually accounts for 50% of fires detected globally [*Dwyer et al.*, 2000] and roughly half of the vegetation burned [*Bond et al.*, 2004]. However, 2003 was atypical. as faguire events in other regions, especially Russian fires [*Kasischke et al.*, 2005; *Generoso et al.,* 2007], made significant contributions to atmospheric emissions, effectively altering the proportion of emission sources.

Emissions from regions defined as boreal North American (BONA) and boreal Asia (BOAS) contributed the greatest amount of OCBC (28% or 5.5 Tg). Much of this was due to the large scale fire event near Lake Baikal [*Generoso et al.,* 2007]. Indeed, the Lake Baikal regional fires [40-90°N; 60-180°E] of 2003 were responsible for 4.5 Tg of OCBC. This is close to the GFEDv2 value of 6.1 Tg of OCBC and similar to *Generoso et al.* [2007] estimate of 5.8 Tg for this same region and time frame.

South America (SHSA and NHSA) contributed to roughly 24% of the global burden of OCBC from fires (4.8 Tg this approach compared to 3.63 Tg for the GFEDv2). Of particular interest is the Arc of Deforestation [*Fearnside and Hall-Beyer*, 2007] which was responsible for 3.1 Tg, or 65%, of all emissions from South America and 15% of the global source. Southeast Asia (SEAS) and Australia (AUST) each produced roughly 5.7% and 4.8% of the global OCBC emission loads, (1.14 Tg and 0.95 Tg, respectively for this approach compared to 0.88 Tg and 1.72 Tg for the GFEDv2).

Tables 4.2 and 4.3 provide a global comparison of the FRE-based OCBC estimates with the GFEDv2 for the period 2001-2007. Years 2001 and 2002 were estimated using Terra FRP which had several data gaps due to instrument problems which may account for some of the underestimation in the FRE-based approach. It should be noted that the GFEDv2 accounts for soil organic carbon burning which is less likely to be detected by MODIS and therefore is not accounted for in the FRE-based estimate. This may explain the systematic underestimation in the emissions estimates compared to the GFEDv2 over Equatorial Asia (EQAS).

For North and South Africa (NHAF and SHAF), the FRE-based emission estimate and the GFEDv2 estimate showed a very small inter-annual variation during the 2001-2007 period (coefficient of variation (CV)[9] between 0.05 and 0.12) however there is about a factor 2 between the two estimates, as already noted for 2003. Comparison of biomass burned in Africa between FRE-based estimates and the GFEDv2 revealed a factor of 3 difference in fuel load (see Chapter 3) suggesting this as a potential source of discrepancy in emission estimates.

Emissions over boreal North American (BONA) and boreal Asia (BOAS) generally agreed between the FRE-based estimates and the GFEDv2 except in 2002 for BOAS (2.4 Tg and 4.5 Tg, respectively). In addition, the CV calculated for BONA and BOAS was similar between the two datasets and reflects greater inter-

[9] The CV is a normalized measure of variation calculated as the ratio of the standard deviation to the mean. It is a useful statistic for comparing the degree of variability between datasets despite differences in means or units.

Table 4.2: Comparison of regional (see Figure 4.8) biomass burning OCBC annual total emission estimates (Tg) made in this research (bold) versus the GFEDv2 (not bold)

	2001	2002	2003	2004	2005	2006	2007
BONA	**0.23,** 0.19	**0.88,** 0.88	**0.90,** 1.14	**0.92,** 1.32	**0.59,** 0.68	**0.82,** 0.53	**0.63,** 0.41
TENA	**0.47,** 0.34	**0.65,** 0.42	**0.58,** 0.25	**0.37,** 0.25	**0.43,** 0.35	**0.63,** 0.36	**0.96,** 0.60
CEAM	**0.43,** 0.21	**0.43,** 0.33	**0.54,** 0.95	**0.26,** 0.15	**0.58,** 0.40	**0.36,** 0.29	**0.34,** 0.27
NHSA	**0.37,** 0.44	**0.31,** 0.33	**0.52,** 1.08	**0.39,** 0.41	**0.29,** 0.29	**0.29,** 0.28	**0.40,** 0.48
SHSA	**2.86,** 2.74	**3.72,** 3.01	**4.28,** 2.55	**5.17,** 5.29	**4.53,** 5.54	**3.10,** 2.69	**4.48,** 5.85
EURO	**0.08,** 0.41	**0.05,** 0.67	**0.10,** 0.41	**0.05,** 0.48	**0.08,** 0.54	**0.09,** 0.92	**0.09,** 0.48
MIDE	**0.04,** 0.07	**0.03,** 0.08	**0.02,** 0.19	**0.03,** 0.05	**0.03,** 0.06	**0.03,** 0.05	**0.04,** 0.03
NHAF	**2.71,** 6.32	**2.52,** 5.61	**2.57,** 4.63	**2.57,** 4.92	**2.66,** 5.38	**2.34,** 4.53	**2.91,** 5.70
SHAF	**3.56,** 4.79	**2.80,** 4.61	**2.62,** 4.57	**2.62,** 4.55	**2.91,** 4.91	**2.64,** 4.30	**2.67,** 4.35
BOAS	**1.29,** 1.86	**2.40,** 4.50	**4.64,** 6.08	**0.79,** 1.15	**1.46,** 1.17	**1.71,** 2.29	**1.14,** 1.36
CEAS	**0.70,** 0.47	**0.86,** 0.61	**0.78,** 0.39	**0.81,** 0.52	**0.61,** 0.45	**0.71,** 0.53	**0.63,** 0.52
SEAS	**1.16,** 1.89	**1.00,** 0.94	**1.14,** 0.88	**1.52,** 2.05	**1.30,** 1.14	**1.20,** 0.89	**1.58,** 2.91
EQAS	**0.30,** 0.52	**0.74,** 2.76	**0.38,** 1.03	**0.60,** 1.86	**0.52,** 2.82	**0.73,** 4.65	**0.26,** 0.43
AUST	**1.95,** 1.61	**1.63,** 1.37	**0.95,** 1.72	**1.03,** 0.98	**0.51,** 0.53	**1.09,** 1.45	**0.90,** 1.03
TOTAL	**16.20,** 21.86	**18.01,** 26.12	**20.02,** 25.86	**17.11,** 23.98	**16.51,** 24.25	**15.74,** 23.75	**17.03,** 24.41

Table 4.3: Comparison of regional (see Figure 4.8) biomass burning OCBC annual mean, standard deviation, and coefficient of variation emission estimates made in this research (bold) versus the GFEDv2 (not bold).[10]

	MEAN	**SD**	**CV**
BONA	**0.71,** 0.74	**0.25,** 0.40	**0.35,** 0.55
TENA	**0.58,** 0.37	**0.19,** 0.12	**0.33,** 0.33
CEAM	**0.41,** 0.37	**0.11,** 0.27	**0.28,** 0.72
NHSA	**0.38,** 0.47	**0.09,** 0.28	**0.24,** 0.59
SHSA	**4.02,** 3.95	**0.83,** 1.52	**0.21,** 0.38
EURO	**0.08,** 0.56	**0.02,** 0.18	**0.25,** 0.33
MIDE	**0.03,** 0.07	**0.01,** 0.05	**0.23,** 0.70
NHAF	**2.61,** 5.30	**0.18,** 0.64	**0.07,** 0.12
SHAF	**2.83,** 4.58	**0.34,** 0.22	**0.12,** 0.05
BOAS	**1.92,** 2.63	**1.30,** 1.92	**0.68,** 0.73
CEAS	**0.73,** 0.50	**0.09,** 0.07	**0.13,** 0.14
SEAS	**1.27,** 1.53	**0.21,** 0.78	**0.17,** 0.51
EQAS	**0.50,** 2.01	**0.20,** 1.52	**0.39,** 0.76
AUST	**1.15,** 1.24	**0.48,** 0.42	**0.42,** 0.34
TOTAL	**17.23,** 24.32	**1.43,** 1.42	**0.08,** 0.06

[10] Values are in Tg OCBC. Mean, standard deviation, and coefficient of variation over the 2001 – 2007 period.

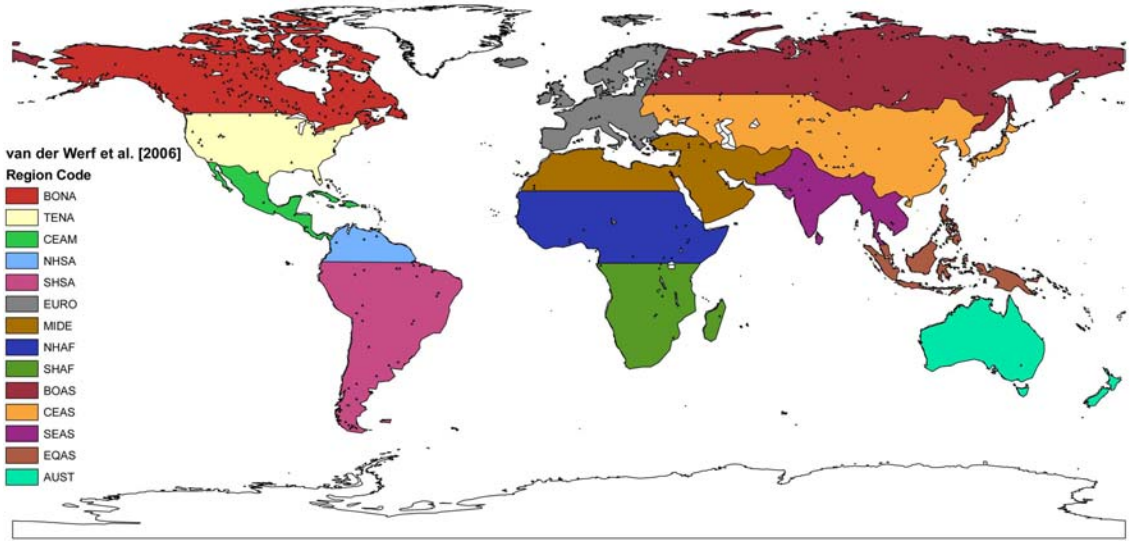

Figure 4.9: Regions used for comparison of results from this study with the GFEDv2. Regional descriptions are explained in *van der Werf et al.* [2006].

annual variability in the BOAS region. For the rest of the regions, the agreement between the GFEDv2 and the estimates made in this research were good for the entire 2001-2007 period; the average was 9.1 Tg for GFEDv2 and 8.1 Tg for the FRE-based estimate.

4.5: Conclusions

Biomass burning is the main global source of fine primary carbonaceous aerosols in the form of organic carbon (OC) and black carbon (BC). An approach to estimate biomass burning aerosol emissions based on the measurement of radiative energy released during combustion was presented. FRE based emission coefficients for the organic and black carbon (OCBC) component of fine mode aerosols were computed from multiple regions encompassing non-forest (savanna/grassland), tropical forest and extratropical forest biomes using OCBC emission estimates derived from the

MODIS fine mode aerosol product and an inverse aerosol transport model. The coefficient for savanna/grassland tended to agree with previously published values of emission factors, but the values obtained for forest biomes were a factor 3 to almost 5 higher. The FRE monthly data were then used to estimate OCBC emissions from biomass burning on a global basis. For 2001 to 2007, the annual estimates are comparable to previously published values. According to the FRE-based estimate, OCBC emissions were greatest in 2003 (20 Tg); roughly 14% above average and primarily driven by wildland fires in the Lake Baikal region (Russia).

A particularly interesting point is that despite the derived emission factors being between a factor 2 and 6 greater than the ones used in the GFEDv2 by *van der Werf et al.* [2006] (which were based on *Andreae and Merlet* [2001]), the annual global emission estimates are between 23% and 31% less than the GFEDv2. While this deviation is still within the uncertainty range shown in the error estimates (Table 4.1), another explanation may be related to uncertainties in the GFEDv2 product, particularly with respect to fuel load assumptions and inaccuracies in the burned area quantification as demonstrated in Chapter 3.

Chapter 5: Summary, Implications of the Findings, and Research Conclusions

5.1 Synthesis of Research

The atmosphere plays a fundamental role in regulating life on Earth. Changes in atmospheric composition can and do affect surface temperatures, hydrology, radiation budgets, weather, and even climate. Therefore, understanding the complex exchanges occurring between the atmosphere and surface requires accurate measurements of the variables characterizing both; for example atmospheric constituents, surface temperatures, and albedo. Quantifying these variables provides the necessary inputs for modeling the dynamic interactions and potential outcomes that result from changes in the relative proportions of atmospheric constituents. In light of the growing evidence for anthropogenic induced climate change, accurate characterization of the impact humans are having, both directly and indirectly, on altering Earth's systems is critical to guiding mitigation policy.

To that end, the goal of this research was to accurately estimate the organic and black carbon aerosol emissions from biomass burning using fire radiative energy (FRE) released as a proxy. As stated earlier, biomass burning is the main global source of organic carbon and black carbon (OCBC) aerosols which alter Earth's radiative balance through various, often opposing mechanisms. To fully understand the dynamics of these interactions, spatial and temporal estimates are needed at synoptic scales, requiring the use of satellite-based remote sensing. However, remote sensing of the surface from measurements taken at the top of the atmosphere requires

careful consideration of the at-sensor signal attenuation due to the atmosphere. This topic was described in Chapter 2. To date, research in this area has focused on the visible and near-infrared parts of the spectrum. Recent research by *French et al.* [2003] and *Petitcolin and Vermote* [2002] highlighted the potential application of a new parametric model for atmospheric correction of thermal infrared data. In Chapter 2, specific consideration was given to the impact of atmospheric attenuation on the MODIS "fire" channel which is used to develop fire radiative power estimates. Following atmospheric correction of the fire band, Chapter 3 described an innovative methodology to quantify the temporal trajectory of fire radiative energy flux from limited, discrete MODIS retrievals. The integral was calculated to produce the total fire radiative energy and then estimates of the biomass fuel consumed were made using an energy-to-mass coefficient. Finally, the crux of this dissertation was presented in Chapter 4 which detailed an approach to estimate OCBC emissions using FRE. The relationship was developed using estimates of OCBC from inverse modeling and the FRE produced in Chapter 3. The result was a global product of OCBC from fires at 0.5° spatial and monthly temporal resolutions. The new estimate was then compared to previously published estimates and an error analysis undertaken.

5.1.1 Thermal Atmospheric Correction to Enable Accurate FRP Estimates

Accurate retrieval of surface temperature from satellite observations requires correction of the thermal channels for atmospheric emission and attenuation. Chapter

2 presented a critical evaluation of a new parametric model tuned to MODIS channels and based upon the MODTRAN radiative transfer code. MODTRAN provides comprehensive and accurate (2-5% in transmittance) capabilities for modeling molecular and aerosol emission, scattered radiance, and atmospheric attenuation [*Berk et al.,* 1998; *Anderson et al.,* 2000]. Comparison with MODTRAN showed a good performance for the parametric model (RMSE < 0.02 for transmittance across all MODIS emissive bands) with computation speeds approximately 3 orders of magnitude faster than MODTRAN. From an operational standpoint this is encouraging because large satellite datasets could be ingested and processed at higher rates than what is achievable using MODTRAN. To test this new approach a comparison was undertaken of sea surface temperatures calculated using atmospheric correction parameters generated from the parametric model and the standard MODIS SST product. The results showed consistency in the estimates (E =0.68) with minimal error and bias (RMSE = 0.49K; bias = 0.45K). Evaluation of the surface temperatures made using the parametric model and MODIS against *in situ* land and water temperature measurements revealed accurate estimates (mean bias < 0.35 K) with little error (RMSE < 1 K). Investigation of profile sources and their effect on atmospheric correction offered insight into the application of the parametric model for operational correction of MODIS thermal bands.

A test of the atmospheric attenuation of MODIS fire channels was necessary prior to undertaking the analysis in Chapters 3 and 4 as atmospheric attenuation was found to reduce the surface FRP. Specific application of the parametric model revealed that the FRP is approximately 20% less at TOA than surface FRP. The bias was primarily

associated with the view angle, but designation of specific atmospheric constituents responsible for the attenuation was beyond the scope of this research. Consideration of atmospheric water vapor content did not yield any correlation with the loss of signal and therefore, at this point, it is assumed that homogeneous species, such as N_2 and CO_2 are responsible. A simple exponential correction factor proved adequate for adjusting the TOA FRP for the apparent loss of energy.

5.1.2 Satellite Driven Fire Radiative Energy Modeling

Application of satellite based measures of fire radiative energy (FRE) has been shown to be effective for estimating biomass consumed, which can then be used to estimate gas and aerosol emissions. However, the use of FRE has been limited in both temporal and spatial scale. In Chapter 3, an approach was presented to approximate the monthly total of hourly fire radiative power retrievals beyond the nominal MODIS FRP observations using the MODIS climate modeling grid (CMG) dataset. The method was based on higher frequency retrievals of instantaneous FRE than those offered from the nominal overpasses of MODIS. Date from the SEVIRI, VIRS, and MODIS sensors were used to model the fire diurnal cycle and a modified Gaussian function proved to be a simple, yet effective approximation of the temporal trajectory of FRP. The Gaussian function parameters were then related to the mean of monthly (n=60) Terra/Aqua (T/A) ratio of FRP from 16 globally dispersed regions. The FRE methodology described in this research adds value to the individual FRP retrievals made by MODIS and is important for assessing biomass burned and associated emissions. To date, the calculation of FRE from MODIS FRP has not

been achieved and therefore this estimate is a first of its kind. The capability for high temporal resolution comparisons were limited, but initial evaluation against FRE estimated using 15-minute retrieval data from the geostationary SEVIRI sensor for Africa showed that the approach produces similar estimates.

Fire activity is widespread with commonly active regions dominating the global picture. Africa, South America, Australia, and boreal regions all showed significant contributions to fire radiative energy production from biomass burning. Estimates of fuels consumed from fire were limited to Africa, but offered an interesting comparison with the Global Fire Emissions Database, version 2 (GFEDv2). GFEDv2 uses a bottom-up emissions calculation approach and can be considered an independent approach, using a combination of remotely sensed parameters with biogeochemical modeling to estimate biomass consumption. The result of the comparison indicated that the GFEDv2 estimate was nearly a factor 4 greater than the estimates in this study. An additional analysis of fuel load estimates from the two approaches suggested that perhaps the GFEDv2's numbers are too high and, in part, responsible for the significant difference in biomass consumption values.

Improvements to the FRE estimates may yield greater biomass burned, however this is unlikely to account for the large differences observed in the comparison with the GFEDv2. The gap in biomass burned estimates highlights the need for further reconciliation among methodologies to reduce uncertainty.

5.1.3 Global OCBC Estimation

An approach to estimate biomass burning aerosol emissions based on the measurement of radiative energy released during combustion was presented in Chapter 4. FRE based emission coefficients for the organic and black carbon (OCBC) component of fine mode aerosols were computed from multiple regions encompassing grassland/savanna, tropical forest and extratropical forest biomes using OCBC emission estimates derived from the MODIS fine mode aerosol product and an inverse aerosol transport model. The emission coefficient values for OCBC were: savanna/grassland (2.47 gOCBC/MJ), tropical forest (7.54 gOCBC/MJ) and extra-tropical forest (11.45 gOCBC/MJ). When the emission coefficients were converted to emission factors the savanna/grassland value agreed with previously published emission factors, but the values obtained for the two forest biomes were a factor 3 to almost 5 higher. Various explanations could be postulated for the discrepancy between the *Andreae and Merlet* [2001] emission factors and the ones derived in this study: 1) the emission coefficients are based on satellite observations that are not representative of fresh smoke emissions but represent smoke aged by several hours or days that may have resulted in significant mass increase of the aerosol through secondary aerosol formation [*Grieshop et al.*, 2008; *Yokelson et al.*, 2008]; 2) the FRP is systematically underestimated due to cloudiness [*Schroeder et al.*, 2008]; 3) canopy obscuration of fire radiative energy, especially in extratropical understory fires; 4) the limitation of the empirical formula used to estimate FRE; and 5) the conversion of emission coefficient to emission factor which is at least uncertain by 10% and may vary from biome to biome as the mechanisms regulating the

partitioning of the radiative, latent and conductive heat may vary. Examination of these possible explanations and reconciling the difference in emissions factors in different biomes is a topic for future research.

The FRE monthly data developed in Chapter 3 were then used to estimate OCBC emissions from biomass burning on a global basis for multiple years. For 2001 to 2007 the OCBC emissions were greatest in 2003 (20 Tg), roughly 14% above average and primarily driven by large wildland fires in the Lake Baikal region (Russia). Comparison with the GFEDv2 indicated that the FRE-based estimates were similar globally and regionally, but generally were slightly lower. Regional and temporal variations were similar as expressed by the means of standard deviation and coefficient of variation.

To reiterate the point made in Chapter 4, a source of confusion and potential error is the discrepancy in emission factors and emission loads derived from this research and the GFEDv2. Although the derived emission factors in this research were between 3 and 5 times greater than the ones used in the GFEDv2, the annual global emission estimates were roughly 30% less. The investigation of differences in fuels consumed and fuel loads in Chapter 3 implies that the GFEDv2 is at least partially accountable for the OCBC emissions differences.

5.2 Implications of the Findings

The result of the error budget in Chapter 4 showed a potential uncertainty in the OCBC estimate of approximately 58%. This would imply that the hypothesis developed for this research, that *the FRE-based estimate could yield accurate*

estimates with less uncertainty than current estimates, is unqualified. Although comparison with other published estimates of OCBC emissions from fire indicates a good agreement, this is not necessarily a valid assessment of the products accuracy or an indication of its significance. Indeed, a true validation is unrealistic at a global scale necessitating an intercomparison of published estimates as the next-best alternative to reach consensus in estimates. Regarding the uncertainty in these estimates, improvement may be easiest in the FRE-based methodology, given the direct geophysical approach and use of fewer variables, resulting in a reduction in the error of the product.

5.2.1 OCBC Impacts on Radiative Forcing

To put the estimated OCBC emissions into a broader context, their impact on global radiative forcing is considered. Radiative forcing (RF) offers an easily quantifiable and comparable variable for understanding climate change. It is defined by the *IPCC* [2007] as an "externally imposed perturbation in the radiative energy budget of the Earth's climate system". Essentially, the RF provides, to a first-order, a quantifiable measure of the change in the Earth-atmosphere balance of incoming solar radiation to outgoing infrared energy; the balance between which explains surface temperature. Measured at the top-of-atmosphere (TOA), RF is expressed in terms of the energy flux per unit area of the globe (W m^{-2}), and has become an important variable in expressing the impact of natural and anthropogenic parameters in influencing climatic alteration. The sign convention means a positive radiative forcing leads to warming in the troposphere while a negative sign results in a cooling.

The *IPCC* [2007] calls for all radiative efficiencies to be calculated in terms of "adjusted" cloudy sky radiative forcing calculated at the tropopause. This is where the temperature of the stratosphere is allowed to adjust so that it remains in global radiative equilibrium. This is because the stratosphere's adjustment timescale is a matter of months, compared to decades for that of the tropopause primarily because of the thermal inertia of the ocean. Radiative forcing calculated without stratospheric adjustments is referred to as "instantaneous" radiative forcing. However, with regards to aerosol RF, the *IPCC* [2007] notes that stratospheric adjustment has a negligible effect on differences observed between forcing impacts measured either at TOA or the tropopause and thus the TOA is used for quantifying the forcing effect.

Long-lived greenhouse gases, such as carbon dioxide (CO_2), methane (CH_4), and nitrous oxide (N_2O), are the largest contributors to radiative forcing and, owing to broad global networks of observations and the persistence of these gases in the atmosphere, are better understood and quantified than other RF agents. Aerosols, on the other hand, such as organic carbon (OC) and black carbon (BC), are short-lived (minutes to days) and heterogeneous in spatial and temporal distribution. As a result, there is greater uncertainty as to the atmospheric effect of aerosols and ultimately the radiative forcing impact [*IPCC*, 2007].

Direct effects of aerosols result in scattering and absorbing shortwave and longwave radiation and impact the energy flux between Earth's surface and the atmosphere. Indirect effects are caused by changes in cloud microphysical properties, and hence radiative properties. The *IPCC* [2007] refers to these as the cloud lifetime effect and cloud albedo effect. The impact on clouds may also affect hydrological

cycles on local to regional scales by what is referred to as the "semi-direct effect" in which cloud burn-off reduces the likelihood of supersaturation and thus rainfall [*Kaufman and Koren*, 2006].

The *IPCC* [2007] put the total direct radiative forcing impact of biomass burning aerosols around 0.03 W m^{-2} with approximately a factor of 4 uncertainty (±0.12). The RF estimate is taken from multiple studies reporting the forcing impact of biomass burning aerosols and is calculated as the average of the mean and median from all of the studies. The uncertainty range is calculated from the standard deviation of all these studies (0.07 W m^{-2}) multiplied by 1.645 to approximate a 90% confidence interval[11]. The uncertainty is important when considering the total net global forcing from all forcing agents is 1.6 W m^{-2}. This would suggest that given the error bars on the aerosol forcing a possible shift in the forcing sign is possible, resulting in either a warming or cooling effect from aerosol forcing. The indirect effects are complex and nonlinear and, although important, as of yet not completely understood or modeled and thus are neglected in the *IPCC* estimate of radiative forcing from biomass burning aerosols.

In this study the instantaneous direct radiative forcing impact is calculated for clear-sky conditions without the influence of the indirect forcing effects discussed above. The RF was calculated using NOAA's Geophysical Fluid Dynamics Laboratory (GFDL) atmospheric model (AM2). A full description of the model can be found in *Magi et al.* [2009]. For comparison, GFEDv2 forcing was calculated

[11] See IPCC 4th Report, Chapter 2: Changes in Atmospheric Constituents and in Radiative Forcing; and specifically Table 2.5 for studies used in the BB radiative forcing estimate.

(Table 5.1). The annual average (2001-2007) forcing is presented globally, for the tropics (22.5˚S – 22.5˚N), and for northern hemisphere mid-latitude (22.5˚N - 60˚N).

Table 5.1: TOA and surface direct radiative forcing impact (W/m^2) of biomass burning aerosol emission estimates from the MODIS FRE approach and the GFEDv2. Tropics refer to global regions between 22.5˚S and 22.5˚N. NH mid refers to northern hemisphere mid-latitudes between 22.5˚N and 60˚N.

	TOA *This Work*	TOA GFED	Surface *This Work*	Surface GFED
Global	-0.08	-0.20	-0.33	-0.53
Tropics	-0.21	-0.35	-0.94	-1.41
NH mid	-0.10	-0.24	-0.30	-0.46

The model was initialized with zero biomass burning emissions, but retaining other natural and anthropogenic sources. Radiative forcing is then reported as the short-wave difference in radiance before and after emissions are considered. Table 5.1 shows that the biomass burning aerosols over the tropics impose a greater forcing burden than in the northern hemisphere mid-latitudes although it is likely that some boreal fire emissions are missed with the *NH mid* latitudinal range selected and thus the forcing impact may be closer. The GFEDv2, not surprisingly shows a greater negative forcing which can be directly linked to the higher emission estimates (Chapter 4).

Comparison with the *IPCC* [2007] suggests that the "MODIS" TOA forcing of -0.08 W m^{-2} is within the range of uncertainty reported by the *IPCC* (±0.12 W m^{-2}). The negative forcing, however, can be attributed to the "clear-sky" set up of the GFDL AM2 which neglects the vertical position of the aerosol layer relative to clouds. *Keil et al.,* [2003] showed that ignoring any aerosol-cloud interactions, the

presence of clouds alone in modeling radiative forcing shifts the impact from negative to positive. This is due to greater absorption of sunlight, depending on the fraction of absorbing aerosols located above the clouds, by as much as a factor of 3 compared with aerosols within or below clouds.

The temperature response of the radiative forcing values shown in Table 5.1 can be calculated using a climate sensitivity parameter (λ) [*Ramanthan et al.,* 1985] which relates the forcing impact to temperature change. Thus, using a mean λ value of 0.5 K/(W m^{-2}) reported by [*Ramanthan et al.,* 1985] and used by the *IPCC* [2007], the expected change in temperatures is shown in Table 5.2.

Table 5.2: Expected temperature response to the biomass burning aerosol emissions radiative forcing impact, calculated using a climate sensitivity parameter of (λ) 0.5 K/(W/m^2).

	TOA *This Work*	TOA GFED	Surface *This Work*	Surface GFED
Global	-0.04	-0.10	-0.16	-0.27
Tropics	-0.11	-0.18	-0.47	-0.71
NH mid	-0.05	-0.12	-0.15	-0.23

Emission estimates from both this study and the GFEDv2 equate to a negative forcing at the surface and TOA, assuming clear-sky conditions. The GFEDv2 forcing is, on average, between 1.5 and 2 times stronger (more negative) which stands to reason given the difference in emission loading estimates. Nevertheless, the implications for global forcing suggest, at least to a first order, that aerosols from biomass burning have a cooling effect and may act as a partial offset to anthropogenic forcing agents such as CO_2 from fossil fuel combustion.

5.3 Future Research and Developments

The error budget produced in Chapter 4 highlighted various sources of error and provided insight into directions to follow to improve the estimates made in this research. The following section offers a discussion of potential future developments to some of the critical components in this study.

5.3.1 The Parametric Model

Consistent, periodic sampling to validate profiles, similar to the current aerosol – AERONET framework used for the MODIS aerosol product, should be developed. Although it was hoped that radiosonde data could provide the basis for site specific validation data, this research has shown that inconsistency in radiosonde launch timing and profile retrieval at some sites limits the effectiveness of this data source for synoptic, vicarious calibration. Nevertheless, a focus on developing an operational scheme for near-real time atmospheric correction using profile data retrieved from AIRS and MODIS should be considered; with MODIS providing the spatial resolution and AIRS providing the necessary accuracy.

5.3.2 Improving FRE Estimates

In order to truly validate FRE estimates greater spatial and temporal resolution data are needed. The evaluation of the FRE estimates with SEVIRI data offered a comparison with FRP retrievals made at higher temporal resolution, but incurred the downside of coarser spatial resolution. Future endeavors would include a scaling approach to test the temporal trajectory of instantaneous fire energy and total fire

radiative energy released from a fire event. This would include the use of *in situ* observations, perhaps with a combination of field and laboratory experiments to reconcile differences between these two approaches. The next tier of retrievals would be from airborne observations, perhaps including both tower platforms (for small scale fires) and unmanned aircraft. The Ikhana unmanned airborne vehicle (UAV) used by the fire research at NASA AMES offers some opportunities in this regard. Recent field work demonstrated that while monitoring FRP from a helicopter seems ideal, many factors can limit the success of this tactic and that greater flexibility in choice of fires to observe and timing allowed for observation is needed. Moderate to high spatial resolution satellite observations would be employed in the next scaling layer and allow for greater spatial coverage while being constrained by higher spatial and temporal observations. To that end, geostationary satellite observations would cap the scaling approach, providing high temporal (15 – 30 minute) retrievals to aid in characterizing the diurnal cycle of fire radiative power as has been shown in this research. Incorporating sensors such as the Geostationary Operational Environmental Satellites (GOES) would offer greater spatial coverage beyond the SEVIRI sensor. Careful consideration of the limitations of comparison between sensors at multiple scales would obviously be needed [*Schroeder et al.,* 2005].

Other considerations worth pursuing to improve FRP retrievals from the MODIS sensor include parameterization of the sub-surface organic layer burning. According to

French et al. [2004] surface organic layer burning is largest source of uncertainty in boreal biomass burning emission estimates. *Page et al.* [2002] estimated 0.19-0.23

Gt of carbon released to the atmosphere from peat combustion during 1997 Indonesian fires. Their estimates were based on peat thickness, pre-fire land cover, and burnt area data collected from ground measurements and Landsat TM/ETM imagery. Satellite imagery proved useful for classifying land cover and determining burn scars, but they discovered that due to residual haze after fires and frequent cloud cover the use of synthetic aperture radar (SAR) was necessary to determine the extent of burnt areas. Cloud cover has already been revealed by *Schroeder et al.* [2008] to limit fire detection capabilities for Brazilian fires. The spatial resolution of MODIS is another limitation to detecting fires in peatlands (and thus FRP estimation) as shown by *Siegert et al.* [2004]. Developing a connection between field estimates of surface and sub-surface organic burning, burned area, and FRP would allow for parameterization of this component of fire radiative energy.

5.3.3 OCBC Inversion Product

Future work will include refining the FRE-based emission coefficient estimates using the sources of error outlined in the error budget as guidance for components to improve. Closer examination of the emission coefficients and emission factors for Africa, a region which showed a strong correlation between FRE and inversion estimates of OCBC in 2003 will aid in understanding the spatial and temporal variability in this parameter.

For 2001 to 2007 the annual estimates were close to previously published values, however some regional differences warrant further investigation. Africa emission estimates were well correlated between the FRE-based approach and the GFEDv2,

but nearly a factor of 2 lower in the former. In a similar fashion, EQAS estimates were, on average, underestimated by about a factor of 4. Investigation of fuel loads, biomass burned, and in the case of EQAS, surface and sub-surface organic matter burning (i.e. peat) is needed.

The examination of several factors influencing aerosol emissions from vegetation fires warrant future consideration. These include, but are not limited to: radiative properties as a function of aerosol composition, smoke aging, the effect of relative humidity, and chemical composition of aerosol emissions. As an example, the proportion of organic and black carbon generally comprises between 55 and 75% of the total fine mode particulate matter (PM2.5), but this proportion, as well as the ratio of BC to OC, is critical to describing the radiative impact [*Magi et al.,* 2009].

The aging of smoke which results in the growth of aerosols by as much as 40% [*Reid et al.,* 2005] has implications for light scattering and absorbing properties. *Hobbs et al.* [1997] showed an increased scattering efficiency of aerosols as they aged. The increase was due to growth of the smoke particles as a result coagulation and gas-to-particle transformation, resulting in particle sizes with greater scattering potential. *Magi et al.* [2009] demonstrated through sensitivity tests that increasing the geometric mean diameter can increase both the aerosol optical thickness and single scattering albedo, resulting in significant changes to the radiative forcing impact.

Another component worth examining is the effect of relative humidity on the size distribution of OCBC. The impact has been shown to be most dramatic in the first hour of the aging process and results in greater total light scattering [*Magi et al.,* 2003]. Although relative humidity is generally not a major influence on aerosol size

distributions given most burning occurs in periods of low atmospheric water vapor content (< 30%), it could potentially be a factor in regions with burning occurring during periods of moderate-to-high relative humidity (i.e. > 50%) as might happen in early dry season fires or areas of active deforestation in the humid tropics [*Hobbs et al.,* 1997].

5.4 Conclusions

The research presented in this thesis shows that a direct global estimate of FRE and biomass consumed is currently feasible and offers an alternative and independent means of OCBC emissions estimates other than the bottom-up approach adopted by the GFEDv2 and others. It also provides the potential of measuring biomass consumed by fire using a FRE-based biomass consumption factor. The OCBC estimate made from satellite derived FRE is close to that reported in the GFEDv2 [*van der Werf et al.,* 2006] and to other estimates for similar time periods [*Hoelzemann et al.,* 2004; *Schultz et al.,* 2008]. The implications of the estimated OCBC in terms of RF suggest a cooling effect at both TOA and surface. Further research on this topic should focus on assessment of regional estimates of FRE, FRE-based emission coefficients, and subsequently OCBC emissions. Validation with higher spatial and temporal resolution data would go a long way towards constraining estimates and improving reconciliation with other global emission datasets. To that end, collaboration between researchers making *in situ* and remotely sensed measures of the variables discussed herein (rate of energy release, emissions, fuels consumed, fuel load, etc.) and the various approaches employed would offer a better

understanding of the dynamics of estimating biomass burned and associated emissions.

References

Anderson, G. P., J. H. Chetwynd, A. J. Ratkowski, G. W. Felde, J. A. Gardner, M. L. Hoke, B. Pukall, J. Mello, L. S. Jeong, and A. Berk (2000), MODTRAN4 – radiative transfer for remote sensing, paper presented at the Conference for algorithms for multispectral, hyperspectral, and ultraspectral imagery VI, Orlando, FL, 24-26 April.

Andreae, M. O., and P. Merlet (2001), Emission of trace gases and aerosols from biomass burning, *Global Biogeochem. Cycles*, *15*(4), 955–966.

Andreae, M.O. (2004), Assessment of global emissions from vegetation fires, *Int. Forest Fire News (IFFN)*, *31*, 112-121.

Barrie, L. A., J. Langen, P. Borrell, O. Boucher, J. Burrows, C. Camy-Peyret, J. Fishman, A. Goede, C. Granier, and E. Hilsenrath (2004), The changing atmosphere, An integrated global atmospheric chemistry observation theme for the IGOS partnership (IGACO).

Barton, I. J. (1995), Satellite-derived sea surface temperatures: Current status, *J. Geophys. Research*, *100*, 8777-8790.

Barton, I. J., P. J. Minnett, K. A. Maillet, C. J. Donlon, S. J. Hook, A. T. Jessup and T. J. Nightingale (2004), The Miami 2001 infrared radiometer calibration and inter-comparison. Part II: Ship board results, *J. Atm. Oceanic Tech*., *21*, 268-283.

Berk, A., L. Bernstein, G. Anderson, P. Acharya, D. Robertson, J. Chetwynd, and S. Adler-Golden (1998), MODTRAN cloud and multiple scattering upgrade with application to AVIRIS, *Remote Sens. Environ., 65*, 367-375.

Bond, T. C., D. G. Streets, K. F. Yarber, S. M. Nelson, J. H. Woo, and Z. Klimont (2004), A technology-based global inventory of black and organic carbon emissions from combustion, *Journal of Geophysical Research-Atmospheres*, *109*(D14), D14203, doi :10.1029/2003jd003697.

Boschetti, L., H. D. Eva, P. A. Brivio, and J. M. Gregoire (2004), Lessons to be learned from the comparison of three satellite-derived biomass burning products, *Geophysical Research Letters*, *31*(21), L21501, doi:10.1029/2004gl021229.

Cahoon Jr., D. R., , B. J. Stocks, M. E. Alexander, B. A. Baum, and J. G. Goldammer (2000), Wildland fire detection from space: Theory and application, in *Biomass burning and its inter-relationships with the climate system*, edited by J. L. Innes, M. Beniston, and M. M. Verstraete, pp. 1-15, Dordrecht, Kluwer Academic Publishers.

Cary, G. J., and J. C. G. Banks (2000), Fire regime sensitivity to global climate change: An Australian perspective, in *Biomass burning and its inter-relationships with the climage system*, edited by J. L. Innes, M. Beniston, and M. M. Verstraete, pp. 233-245, Dordrecht, Kluwer Academic Publishers.

Chapman, S.J., and M. Thurlow (1998), Peat respiration at low temperatures, *Soil Biology & Biochemistry*, *30*, 1013-1021.

Chin, M., P. Ginoux, S. Kinne, O. Torres, B. N. Holben, B. N. Duncan, R. V. Martin, J. A. Logan, A. Higurashi, and T. Nakajima (2002), Tropospheric Aerosol Optical Thickness from the GOCART Model and Comparisons with Satellite and Sun Photometer Measurements, *Journal of the Atmospheric Sciences*, *59*(3), 461-483.

Chin, M., T. Diehl, P. Ginoux, and W. Malm (2007), Intercontinental transport of pollution and dust aerosols: implications for regional air quality, *Atmospheric Chemistry and Physics*, *7*(21), 5501-5517.

Chou, M.-D., D. P. Kratz, and W. Ridgway (1991), Infrared Radiation Parameterizations in Numerical Climate Models, *J. Climate*, *4*, 424-437.

Cicerone, R. J. (1994), Fires, atmospheric chemistry, and the ozone layer, *Science*, *263*, 1243-1244.

Clough, S. A., R. W. Davies, and R.H. Tipping (1982), The line shape for collisionally broadened molecular transitions: A quantum theory satisfying the fluctuation dissipation theorem, in *Spectral Line Shapes*, Proc. of the 6th Int. Conf., Boulder, CO, 12-16 July.

Clough, S. A. (1995), The Water Vapor Continuum and its Role in Remote Sensing, *Optical Remote Sensing of the Atmosphere*, *2*, 76-78.

Coll, C., V. Caselles, J. M. Galve, E. Valor, R. Niclos, J. M. Sanchez, and R. Rivas (2005), Ground measurements for the validation of land surface temperatures derived from AATSR and MODIS data, *Remote Sens. Environ.*, *97*, 288-300.

Crutzen, P. J., L. E. Heidt, J. P. Krasnec, W. H. Pollock, and W. Seiler (1979), Biomass burning as a source of atmospheric gases CO, H_2, N_2O, NO, CH_3Cl, and COS. *Nature*, *282*, 253-256.

Crutzen, P. J., and M. O. Andreae (1990), Biomass Burning in the Tropics: Impact on Atmospheric Chemistry and Biogeochemical Cycles, *Science*, *250* (4988), 1669-1678.

Deschamps, P. Y., and T. Phulpin (1980), Atmospheric correction of infrared measurements of sea-surface temperature using channels at 3.7, 11 and 12μm, *Boundary-Layer Meteorology*, *18*, 131-143.

Dozier, J. (1981), A method for satellite identification of surface temperature fields of subpixel resolution, *Remote Sensing of Environment*, *11*(3), 221-229

Dubovik, O., T. Lapyonok, Y. J. Kaufman, M. Chin, P. Ginoux, R. A. Kahn, and A. Sinyuk (2008), Retrieving global aerosol sources from satellites using inverse modeling, *Atmospheric Chemistry and Physics*, *8*(2), 209-250

Durre, I., R. S. Vose, and D. B. Wuertz (2006), Overview of the integrated global radiosonde archive, *J. Climate*, *19*, 53-68.

Dwyer, E., S. Pinnock, J. M. Gregoire, and J. M. C. Pereira (2000), Global spatial and temporal distribution of vegetation fire as determined from satellite observations, *International Journal of Remote Sensing*, *21*(6-7), 1289-1302.

Ellicott, E., E. Vermote, F. Petitcolin, and S. J. Hook (2009a), Validation of a new parametric model for atmospheric correction of thermal infrared data, *IEEE Trans. Geosci. Remote Sens*., *47,* 295-311.

Ellicott, E., E. Vermote, L. Giglio, and G. Roberts (2009b), Estimating biomass consumed from fire using MODIS FRE, *Geophys. Res. Lett., 36,* L13401, doi:10.1029/2009GL038581.

Eugenio, F., J. Marcello, A. Hernandez-Guerra, and E. Rovaris (2005), Regional optimization of an atmospheric correction algorithm for the retrieval of sea surface temperature from the Canary Islands-Azores-Gibraltar area using NOAA/AVHRR data, *Int. J. Remote Sens.*, *26*, 1799-1814.

Fearnside, Philip (Lead Author); Mryka Hall-Beyer (Topic Editor). 2007. "Deforestation in Amazonia." In: Encyclopedia of Earth. Eds. Cutler J. Cleveland (Washington, D.C.: Environmental Information Coalition, National Council for Science and the Environment). [First published in the Encyclopedia of Earth March 15, 2007; Last revised March 30, 2007; Retrieved January 19, 2009]. <http://www.eoearth.org/article/Deforestation_in_Amazonia

Flannigan, M. D., K. A. Logan, B. D. Amiro, W. R. Skinner, and B. J. Stocks (2005), Future area burned in Canada, *Climatic Change,* 72, 1-16.

Freeborn, P. H., M. J. Wooster, W. M. Hao, C. A. Ryan, B. L. Nordgren, S. P. Baker, and C. Ichoku (2008), Relationships between energy release, fuel mass loss, and trace gas and aerosol emissions during laboratory biomass fires, *Journal of Geophysical Research-Atmospheres*, *113*(D1), D01301,doi:10.1029/2007jd008679.

French, A. N., J. M. Norman, and M. C. Anderson (2003), A simple and fast atmospheric correction for spaceborne remote sensing of surface temperature, *Remote Sens. Environ.*, *87*, 326-333.

French, N. H. F., P. Goovaerts, and E. S. Kasischke (2004), Uncertainty in estimating carbon emissions from boreal forest fires, *Journal of Geophysical Research*, *109*(D14).

García, L., and V. Caselles (1991), Mapping burns and natural reforestation using Thematic Mapper data, *Geocarto International*, *1*, 31–37.

Generoso, S., I. Bey, J. L. Attie, and F. M. Breon (2007), A satellite- and model-based assessment of the 2003 Russian fires: Impact on the Arctic region, *Journal of Geophysical Research-Atmospheres*, *112*(D15), D15302, doi:10.1029/2006jd008344.

Giglio, L., and C. O. Justice (2003), Effect of wavelength selection on characterization of fire size and temperature, *Int. J. Remote Sens.*, *24*, 3515-3520.

Giglio, L. (2005), MODIS Collection 4 active fire product user's guide: Version 2.2, http://modis-fire.umd.edu/documents/MODIS_Fire_Users_Guide_2.2.pdf (last accessed 20 September 2008).

Giglio, L., I. Csiszar, and C. O. Justice (2006), Global distribution and seasonality of active fires as observed with the Terra and Aqua Moderate Resolution Imaging Spectroradiometer (MODIS) sensors, *Journal of Geophysical Research-Biogeosciences*, *111*,G02016, Doi 10.1029/2005jg000142.

Giglio, L. (2007), Characterization of the tropical diurnal fire cycle using VIRS and MODIS observations, *Remote Sensing of Environment*, *108*(4), 407-421.

Giglio, L., T. Loboda, D. P. Roy, B. Quayle, C. O. Justice (2009), An active-fire based burned area mapping algorithm for the MODIS sensor, *Remote Sens. Environ., 113,* 408-420, doi: 10.1016/j.rse.2008.10.006.

Gottsche, F. M., and F. Olesen (2002), Evolution of neural network for radiative transfer calculations in the terrestrial infrared, *Remote Sens. Environ*., *80*, 157-164.

Grant, W. B. (1990), Water vapor absorption coefficients in the 8-13m spectral region: a critical review, *Applied Optics, 29*, 451-462.

Grieshop, A. P., J. M. Logue, N. M. Donahue, and A. L. Robinson (2009), Laboratory investigation of photochemical oxidation of organic aerosol from wood fires–Part 1: Measurement and simulation of organic aerosol evolution, *Atmos. Chem. Phys. Discuss*, *8*, 15699-15737.

Hawbaker, T. J., V. C. Radeloff, A. D. Syphard, Z. Zhu, and S. I. Stewart (2008), Detection rates of the MODIS active fire product in the United States, *Remote Sens. Environ.,* 112(5), doi :10.1016/j.rse.2007.12.008.

Hély, C., P. R. Dowty, S. Alleaume, K. K. Caylor, S. Korontzi, R. J. Swap, H. H. Shugart, and C. O. Justice (2003), Regional fuel load for two climatically contrasting years in southern Africa, *J. Geophys. Res., 101*, 23,551-23,568, doi: 10.1029/2002JD002341.

Hobbs, P. V., J. S. Reid, R. A. Kotchenruther, R. J. Ferek, and R. Weiss (1997), Direct radiative forcing by smoke from biomass burning, *Science, 275,* 1776-1778.

Hoelzemann, J. J., M. G. Schultz, G. P. Brasseur, C. Granier, and M. Simon (2004), Global Wildland Fire Emission Model (GWEM): Evaluating the use of global area burnt satellite data, *Journal of Geophysical Research-Atmospheres*, *109*,D14s04, doi :10.1029/2003jd003666.

Hook, S. J., F. J. Prata, R. E. Alley, A. Abtahi, R. C. Richards, S. G. Schladow, and S. O. Palmarsson (2003), Retrieval of lake bulk and skin temperatures using Along-Track Scanning Radiometer (ATSR-2) data: A case study using Lake Tahoe, California, *J. Atm. and Oceanic Tech.*, *20*, 534-548.

Hook, S. J., G. Chander, J. A. Barsi, R. E. Alley, A. Abtahi, F. D. Palluconi, B. L. Markham, R. C. Richards, S. G. Schladow, and D. L. Helder (2004), In-Flight Validation and Recovery of Water Surface Temperature with Landsat 5 Thermal Infrared Data Using an Automated High Altitude Lake Validation Site at Lake Tahoe CA/NV, USA, *IEEE Tran. Geosci. Remote Sens*., *42*, 2767- 2776.

Hook, S. J., W. B. Clodius, L. Balick, R. E. Alley, A. Abtahi, R. C. Richards, and S. G. Schladow (2005), In-Flight Validation of Mid- and Thermal Infrared Data From the Multispectral Thermal Imager (MTI) Using an Automated High-Altitude Validation Site at Lake Tahoe CA/NV, USA, *IEEE Tran. Geosci. Remote Sens*., *43,* 1991- 1999.

Hook, S. J., R. G. Vaughan, H. Tonooka and S. Geoffrey Schladow (2007), Absolute Radiometric In-Flight Validation of Mid and Thermal Infrared Data from ASTER and MODIS on the Terra Spacecraft using the Lake Tahoe CA/NV, USA Automated Validation Site, *IEEE Trans. Geosci. Remote Sens*., *45*, 1798-1807.

Ichoku, C., and Y. J. Kaufman (2005), A method to derive smoke emission rates from MODIS fire radiative energy measurements, *Ieee Transactions on Geoscience and Remote Sensing*, *43*(11), 2636-2649,doi:10.1109/Tgrs.2005.857328.

Innes, J. L. (2000), Biomass burning and climate: an introduction, *Biomass Burning and Its Inter-Relationships with the Climate System*, in *Biomass burning and its inter-relationships with the climate system*, edited by J. L. Innes, M. Beniston, and M. M. Verstraete, pp. 1-15, Dordrecht, Kluwer Academic Publishers.

IPCC, 2007: Climate Change 2007: The Physical Science Basis. Contribution of Working Group I to the Fourth Assessment Report of the Intergovernmental Panel on Climate Change [Solomon, S., D. Qin, M. Manning, Z. Chen, M. Marquis, K.B. Averyt, M. Tignor and H.L. Miller (eds.)]. Cambridge University Press, Cambridge, United Kingdom and New York, NY, USA, 996pp.

Ito, A., and J. E. Penner (2005), Historical emissions of carbonaceous aerosols from biomass and fossil fuel burning for the period 1870-2000, *Global Biogeochemical Cycles*, *19*(2), Gb2028,doi:10.1029/2004gb002374.

Jacob, F., A. Olioso, A. Gu, Z. Su, and B. Seguin (2002), Mapping surface fluxes using visible, near infrared, thermal infrared remote sensing data with a specialized surface energy balance model, *Agronomie*, *22*, 669-680.

Jacobson, M. Z. (2001), Strong radiative heating due to the mixing state of black carbon in atmospheric aerosols, *Nature, 409,* 695-697.

Ji, Y. M., and E. Stocker (2002), An overview of the TRMM/TSDIS fire algorithm and product, *International Journal of Remote Sensing*, *23*(16), 3285-3303, doi:10.1080/01431160110070816.

Kasischke, E. S., N. L. Christensen Jr, and B. J. Stocks (1995a), Fire, Global Warming, and the Carbon Balance of Boreal Forests, *Ecological Applications*, *5*(2), 437-451

Kasischke, E. S., N. H. F. French, L. L. Bourgeau-Chavez, and N. L. Christensen (1995b), Estimating release of carbon from 1990 and 1991 forest fires in Alaska, *J. Geophys. Res.*, *100*(D2), 2941-2951.

Kasischke, E. S., and J. E. Penner (2004), Improving global estimates of atmospheric emissions from biomass burning, *Journal of Geophysical Research-Atmospheres*, *109*,D14s01,doi :0.1029/2004jd004972.

Kasischke, E. S., E. J. Hyer, P. C. Novelli, L. P. Bruhwiler, N. H. F. French, A. I. Sukhinin, J. H. Hewson, and B. J. Stocks (2005), Influences of boreal fire emissions on Northern Hemisphere atmospheric carbon and carbon monoxide, *Global Biogeochemical Cycles*, *19*(1),Gb1012,doi:10.1029/2004gb002300.

Kaufman, Y., C. Tucker, and I. Fung (1990), Remote sensing of biomass burning in the tropics, *Journal of Geophysical Research*, *95*(D7), 9927-9939.

Kaufman, Y. J., L. Remer, R. Ottmar, D. Ward, R. R. Li, R. Kleidman, R. S. Fraser, L. Flynn, D. McDougal, and G. Shelton (1996), Relationship between remotely sensed fire intensity and rate of emission of smoke: SCAR-C experiment, *Global Biomass Burning*, 685–696.

Kaufman, Y. J., and R. S. Fraser (1997), The effect of smoke particles on clouds and climate forcing. *Science*, 277, 1636-1639.

Kaufman, Y. J., C. O. Justice, L. P. Flynn, J. D. Kendall, E. M. Prins, L. Giglio, D. E. Ward, W. P. Menzel, and A. W. Setzer (1998), Potential global fire monitoring from EOS-MODIS, *J. Geophys. Res.*, *103*(D24), 32215-32238.

Kaufman, Y. J., and I. Koren (2006), Smoke and pollution aerosol effect on cloud cover, *Science, 313*, 665-658.

Keil, A. and J. M. Haywood (2003), Solar radiative forcing by biomass burning aerosol particles during SAFARI 2000: A case study based on measured aerosol and cloud properties, *J. Geophys. Res., 108,* 8467, doi:10.1029/2002JD002315.

Kondratiev, K. Y. A. (1969), Radiation in the Atmosphere, in *International Geophysics Series*, vol 12, 911 pp., Academic Press Inc., New York.

Korontzi, S., D. P. Roy, C. O. Justice, and D. E. Ward (2004), Modeling and sensitivity analysis of fire emissions in southern Africa during SAFARI 2000, *Remote Sensing of Environment*, *92*(3), 376-396

Kratz, D. P. (1995), The correlated-k distribution technique as applied to the AVHRR channels, *J. Quant. Spectrosc. Radiat. Transfer*, *53*, 501-517

Kuhry, P. (1994), The role of fire in the development of *Sphagnum*-dominated peatlands in western boreal Canada, *J. of Ecology*, *82*, 899-910.

Lambin, E. F., and D. Ehrlich (1996), The surface temperature-vegetation index space for land cover and land-cover change analysis, *Int. J. Remote Sens., 17*, 463-487.

Legates, D. R. and G. J. McCabe, Jr. (1999), Evaluating the use of 'goodness-of-fit' measures in hydrologic and hydroclimatic model validation, *Water Resources Res*., *35*, 233-241.

Lenoble, J. (1991), The particulate matter from biomass burning: A tutorial and critical review of its radiative impact, in *Global biomass burning: atmospheric, climatic, and biospheric implication*, edited by J. Levine, pp. 381-386, Cambridge, Massachusetts, MIT press.

Levine, J. S. (2000), Global biomass burning: A case study of the gaseous and particulate matter emissions released to the atmosphere during the 1997 fires in Kalimantan and Sumatra, Indonesia, in *Biomass burning and its inter-relationships with the climate system*, edited by J. L. Innes, M. Beniston, and M. M. Verstraete, pp. 1-15, Dordrecht, Kluwer Academic Publishers.

Levine, J. S. (2003), Burning domestic issues, *Nature*, *423*, 28-29.

Levy, R. C., L. A. Remer, S. Mattoo, E. F. Vermote, and Y. J. Kaufman (2007), Second-generation operational algorithm: Retrieval of aerosol properties over land from inversion of Moderate Resolution Imaging Spectroradiometer spectral reflectance, *Journal of Geophysical Research-Atmospheres*, *112,* D13211, doi:10.1029/2006jd007811.

Lobert, J. M., and J. Warnatz, Emissions from the combustion process in vegetation, in *Fire in the Environment: The Ecological, Atmospheric, and Climatic Importance of Vegetation Fires,* edited by P. J. Crutzen and J. G. Goldammer, pp. 15-38, John Wiley, New York, 1993.

Magi, B. I., and P. V. Hobbs (2003), Effects of humidity on aerosols in southern Africa during the biomass burning season, *J. of Geophys. Research, 108,8495*, doi:10.1029/2002JD002144.

Magi, B. I., P. Ginoux, Y. Ming, and V. Ramaswamy (2009), Evaluation of tropical and extratropical Southern Hemisphere African aerosol properties simulated by a climate model, *J. of Geophys. Research, 114,* D14204, doi:10.1029/2008JD011128.

Matthew, K., C. M. Nagarani, and A. S. Kirankumar (2001), Split-window and multi-angle methods of sea surface temperature determination: an analysis, *Int. J. Remote Sens.*, *22*, 3237-3251.

McClain, E. P., W. G. Pichel, and C. C. Walton (1985), Comparative performance of AVHRR-based multichannel sea surface temperatures, *J. of Geophys. Research*, *90*, 11587-11601.

McNaughton, S. J., N. R. H. Stronach, and N. J. Georgiadis (1998), Combustion in natural fires and global emissions budgets, *Ecological Applications, 8*(2), 464-468.

Merchant, C. J., and P. Le Borgne (2004), Retrieval of sea surface temperature from space, based on modeling of infrared radiative transfer: capabilities and limitations, *J. Atm. and Oceanic Tech.*, *21*, 1734-1746.

Minnett, P. J. (2003), Radiometric measurements of the sea-surface skin temperature: the competing roles of the diurnal thermocline and the cool skin, *Int. J. Remote Sens.*, *24*, 5033-5047.

Moore, P. (2002), The future of cool temperate bogs. *Environmental Conservation*, 29, 3-20.

Page, S.E., F. Siegert, J. O. Rieley, H. V. Boehm, A. Jaya, and S. Limin (2002), The amount of carbon released from peat and forest fires in Indonesia during 1997, *Nature, 420*, 61-65.

Penner, J. E., R. E. Dickinson, and C. A. O'Neill (1992), Effects of aerosol from biomass burning on the global radiation budget, *Science, 256,* 1432-1434.

Petitcolin, F., and E. Vermote (2002), Land surface reflectance, emissivity and temperature from MODIS middle and thermal infrared data, *Remote Sens. Environ.*, *83*, 112-134.

Prabhakara, C., G. Dalu, and V. G. Kunde (1974), Estimation of sea surface temperature from remote sensing in the 11-13μm window range, *J. Geophys. Research*, *79*, 5039-5044.

Reid, J. S., T. F. Eck, S. A. Christopher, R. Koppmann, O. Dubovik, D. P. Eleuterio, B. N. Holben, E. A. Reid, and J. Zhang (2005), A review of biomass burning emissions part III: intensive optical properties of biomass burning particles, *Atmospheric Chemistry and Physics*, *5*, 827-849

Remer, L. A., D. Tanre, Y. J. Kaufman, C. Ichoku, S. Mattoo, R. Levy, D. A. Chu, B. Holben, O. Dubovik, A. Smirnov, J. V. Martins, R. R. Li, and Z. Ahmad (2002), Validation of MODIS aerosol retrieval over ocean, *Geophysical Research Letters*, *29*(12),doi:10.1029/2001gl013204.

Roberts, G. J., M. Wooster, G. L. W. Perry, N. Drake, L. M. Rebelo, and F. Dipotso (2005), Retrieval of biomass combustion rates and totals from fire radiative power observations: Application to southern Africa using geostationary SEVIRI imagery, *Journal of Geophysical Research-Atmospheres*,*110*(D21),D21111, doi: 10.1029/2005jd006018.

Roberts, G. J., and M. J. Wooster (2008), Fire detection and fire characterization over Africa using Meteosat SEVIRI, *Ieee Transactions on Geoscience and Remote Sensing*, *46*(4), 1200-1218Doi 10.1109/Tgrs.2008.915751.

Robinson, J. M. (1989), On uncertainty in the computation of global emissions from biomass burning, *Climatic Change*, *14*(3), 243-261

Robinson, J. M. (1991), Fire from space: Global fire evaluation using infrared remote sensing, *International Journal of Remote Sensing*, *12*(1), 3-24.

Roy, D. P., Y. Jin, P. E. Lewis, and C. O. Justice (2005), Prototyping a global algorithm for systematic fire-affected area mapping using MODIS time series data, *Remote Sensing of Environment*, *97*(2), 137-162

Rubio, E., V. Caselles, C. Coll, E. Valour, and F. Sospedra (2003), Thermal-infrared emissivities of natural surfaces: improvements on the experimental set-up and new measurements, *Int. J. Remote. Sens., 20,* 5379-5390.

Running, S. W. (2008), Ecosystem disturbance, carbon, and climate, *Science, 321*, 652-653.

Sato, M., J. Hansen, D. Koch, A. Lacis, R. Ruedy, O. Dubovik, B. Holben, M. Chin, and T. Novakov (2003), Global atmospheric black carbon inferred from AERONET, *Proceed., Nat. Acad. Sci., 100,* 6319-6324, doi:10.1073/pnas.0731897100.

Schroeder, W., J. Morisette, I. Csiszar, L. Giglio, D. Morton, and C. O. Justice (2005), Characterizing vegetation fire dynamics in Brazil through multisatellite data: Common trends and practical issues, *Earth Interactions*, *9(13).*

Schroeder, W., I. Csiszar, and J. Morisette (2008a), Quantifying the impact of cloud obscuration on remote sensing of active fires in the Brazilian Amazon, *Remote Sensing of Environment*, *112*(2), 456-470,doi:10.1016/j.rse.2007.05.004.

Schultz, M. G., A. Heil, J. J. Hoelzemann, A. Spessa, K. Thonicke, J. G. Goldammer, A. C. Held, J. M. C. Pereira, and M. van het Bolscher (2008), Global wildland fire emissions from 1960 to 2000, *Global Biogeochemical Cycles*, *22*(2), Gb2002,doi: 10.1029/2007gb003031.

Seiler, W. and P. J. Crutzen (1980), Estimates of gross and net fluxes of carbon between the biosphere and the atmosphere form biomass burning, *Clim. Change*, 2, 207-247.

Siegert, F., B. Zhukov, D. Oertel, S. Limin, S. E. Page, and J. O. Rieley (2004), Peat fires detected by the bird satellite, *Int. J. Remote Sens., 25(16)*, 3221-3230.

Soja, A. J., W. R. Cofer, H. H. Shugart, A. I. Sukhinin, P. W. Stackhouse, D. J. McRae, and S. G. Conard (2004), Estimating fire emissions and disparities in boreal Siberia (1998-2002), *Journal of Geophysical Research-Atmospheres*, *109*(D14), D14s06, doi: 10.1029/2004jd004570.

Stott, P. (2000), Combustion in tropical biomass fires: a critical review, *Progress in Phys. Geog., 24*, 355-377.

Tonooka, H., F. D. Palluconi, S. J. Hook, and T. Matsunaga (2005), Vicarious Calibration of ASTER Thermal Infrared Bands, *IEEE Trans. Geosci. Remote Sens*., *43*, 2733-2746.

Twomey, S. A., M. Piepgrass, and T. L. Wolfe (1984), An assessment of the impact of pollution on global cloud albedo, *Tellus*, *B36*, 356-366.

van der Werf, G. R., J. T. Randerson. G. J. Collatz. L. Giglio. (2003), Carbon emissions from fires in tropical and subtropical ecosystems, *Global Change Biology*, *9*(4), 547-562.

van der Werf, G. R., J. T. Randerson, L. Giglio, G. J. Collatz, P. S. Kasibhatla, and A. F. Arellano (2006), Interannual variability in global biomass burning emissions from 1997 to 2004, *Atmospheric Chemistry and Physics*, *6*, 3423-3441

Vermote, E., E. Ellicott, O. Dubovik, T. Lapyonok, M. Chin, L. Giglio, and G. J. Roberts (2009), An approach to estimate global biomass burning emissions of organic and black carbon from MODIS fire radiative power, *J. Geophys. Res., 114*, XXX, doi:10.1029/2008JD011188, in press.

Wan, Z., Y. Zhang, Q. Zhang, and Z. Li (2002), Validation of the land-surface temperature products retrieved from Terra Moderate Resolution Imaging Spectrometer data, *Remote Sens. Environ.*, *93*, 163-180.

Whelan, R. J. (1995), The Ecology of Fire, Cambridge Univ. Press, New York.

Wooster, M. J., B. Zhukov, and D. Oertel (2003), Fire radiative energy for quantitative study of biomass burning: Derivation from the BIRD experimental satellite and comparison to MODIS fire products, *Remote Sensing of Environment*, *86*(1), 83-107.

Wooster, M. J., G. Roberts, G. L. W. Perry, and Y. J. Kaufman (2005), Retrieval of biomass combustion rates and totals from fire radiative power observations: FRP derivation and calibration relationships between biomass consumption and fire radiative energy release, *Journal of Geophysical Research-Atmospheres*, *110*(D24), D24311, doi: 10.1029/2005jd006318.

Yokelson, R. J., T. J. Christian, T. G. Karl, and A. Guenther (2008), The tropical forest and fire emissions experiment: laboratory fire measurements and synthesis of campaign data, *Atmospheric Chemistry and Physics*, *8*(13), 3509-3527